UNIVERSITAT POLITÈCNICA
DE CATALUNYA
BARCELONATECH

Single domain spinor Bose-Einstein condensate

by

Silvana Palacios Álvarez

SINGLE DOMAIN SPINOR BOSE-EINSTEIN CONDENSATE

by

SILVANA PALACIOS ÁLVAREZ

Submitted in total fulfilment of the requirements of the degree of Doctor in Philosophy

Supervisor: Prof. Morgan W. Mitchell
ICFO-The Institute of Photonic Sciences
Universitat Politècnica de Catalunya

2017

A mi familia.

ABSTRACT

This work reports on the construction of a new-generation system capable to create single-mode spinor Bose-Einstein condensates of ^{87}Rb, and non-destructively probe them using optical Faraday rotation. This system brings together many of the state-of-the-art technologies in ultra-cold physics in a minimalist design which was possible due to the prolific advances in the field respect to the pioneering experiments (Cornell's, Ketterle's, and Chapman's groups). There is rich phenomena that can be potentially studied in this system from the study of predicted novel quantum phases and topologies to entanglement and spin squeezing which are useful for quantum information and interferometry. The potential of this system make it suitable to answer fundamental questions on the phase transition to a condensed and ferromagnetic state.

In particular, this work describes theoretically and experimentally, the atomic spin coherence, which is relevant for applications like coherent sensing of magnetic fields. In this direction, our findings demonstrate the characteristics of our system make it a sensor with the best predicted energy resolution per unit bandwidth ($\sim 10^{-2}\hbar$) among all the different technologies applied to magnetometry.

The thesis is structured as follows: Part I is dedicated to the mathematical description of the relevant interactions. First, the interaction of optical polarization and atomic spin polarization is reviewed, with special attention to ac-Stark shifts, which are used to generate a conservative trapping potential and Faraday rotation effects that are used for non-destructive spin detection. Second, the interaction of the atoms with a magnetic field is presented. And finally, the mean-filed theory of spinor Bose-Einstein condensation is summarized. The dynamics of a spin-1 system in this picture is described by a three-component Gross-Pitaevskii equation.

Part II contains three chapters describing the implemented technologies and techniques used in the experiment to create and characterize a spinor condensate. The first chapter describes the ultrahigh vacuum, magnetic fields, lasers, spectroscopy and imaging needed to create a magneto optical trap (MOT) and transfer those atoms into an optical dipole trap (ODT). We implemented a non-standard loading technique based on the semi-compensation of the strong differential lightshift induced by the ODT which profits from the effective dark-MOT created at the trap position. In the second chapter we detail, theoretically and experimentally, the all-optical evaporation process employed to achieve condensation in less than five second after the loading. In the final chapter the spin manipulation and read-out techniques are presented. Because there is no observable associated to the spin angle, we exploit the Faraday rotation effect and Stern-Gerlach imaging in order to retrieve information about the spin dynamics.

Finally in Part III, we consider the potential of a spinor BEC as a magnetic sensor. The measurement of fundamental properties defining the sensitivity of the sensor are detailed. Those properties are the volume, the temporal coherence and the read-out noise. We present a model of the magnetic field environment and its repercussion on the noise of the magnetometer. In the last chapter we present our perspectives to the possible applications of our system.

RESUMEN

Este trabajo compila los detalles experimentales de un aparato de "nueva generación" capaz de crear condensados espinoriales de ^{87}Rb en un único dominio magnético, y de obtener información del estado de espín en una forma no destructiva explotando el efecto Faraday. Este aparato conjunta algunas de las tecnologías de punta aplicadas a física de gases ultrafrios en un diseño minimalista. Estas tecnologías se han podido desarrollar debido a los prolíficos avances en el campo, respecto a los experimentos pioneros en los grupos de Cornell, Ketterle y Chapman. Una rica cantidad de fenómenos pueden ser estudiados en este sistema, desde el estudio de novedosas fases y topologías cuánticas hasta la aplicación de entrelazamiento y estados comprimidos relevantes en información cuántica e interferometría. Su potencial lo hace un buen candidato para responder preguntas acerca de la naturaleza de las transiciones ferromagnética y de condensación. En particular, este trabajo describe teorética y experimentalmente la coherencia del estado de espín, el cual, es relevante en aplicaciones como la medición coherente de campos magnéticos. En este sentido, nuestros resultados demuestran que las características de nuestro condensado espinorial lo hacen el sensor con la mejor resolución en energía por unidad de ancho de banda ($\sim 10^{-2}\hbar$), de entre todas las tecnologías aplicadas a magnetometría.

Esta tesis se estructura de la siguiente manera: Part I está dedicada a la descripción matemática de las interacciones relevantes. Primero la interaccioń entre la luz y el espín atómico es revisada, con especial énfasis en el desplazamiento ac-Stark, que es explotado para generar un potencial conservador, así como en las medidas no destructivas del espín via efecto Faraday. En segundo lugar, estudiamos la dinámica de espín bajo la interacción Zeeman entre los átoms y un campo magnético que varía en el tiempo. Finalmente es brevemente tratada la teoría de campo medio (mean-field theory) que describe los condensados espino-

riales en la forma de una ecuación de Gross-Pitaevskii multicomponente.

Part II contiene tres capítulos que detallan la tecnologías y técnicas usadas en el experimento para crear y caracterizar el condensado. El primer capítulo describe el ultra-alto vacío, los campos magnéticos, láseres, espectroscopía e imaging usados para crear una trampa magneto-óptica (MOT), y para transferir esos átomos en una trampa dipolar óptica (ODT). Nosotros implementamos una técnica poco estandard para cargar la ODT, la cual se basa en compensar medianamente el excesivo lightshift diferencial inducido por nuestra ODT. Esta técnica nos ayuda a crear una dark-MOT efectiva con la que podemos conseguir altas densidades de átoms en la ODT. En el segundo capítulo detallamos la evaporación que es "all-optical", con la que podemos conseguir un condensado en menos de 5 s de evaporación. En el capítulo final describimos las técnicas para crear arbitrarios estados de espín y cómo detectarlos. Para esto último explotamos el efecto Faraday y capturamos imágenes Stern-Gerlach.

Finalmente en Part III, estudiamos las propiedades de coherencia, tiempo de vida y extensión espacial del condensado. Detallamos el sistema especialmente en el contexto de sensores magnéticos. Además, presentamos un modelo del campo magnético ambiental y sus repercusiones en el ruido del magnetómetro. En el último capítulo hablamos de algunas de las alternativas aplicaciones de nuestro sistema.

The power of a theory is exactly proportional to the diversity of situations it can explain.

- Elinor Ostrom

¿Que es ello absurdo? decís. ¿Y quién sabe qué es lo absurdo? ¡Y aunque lo fuera! Sólo el que ensaya lo absurdo es capaz de conquistar lo imposible.

- Miguel de Unamuno

ACKNOWLEDGMENTS

Firstly I express my gratitude to Thomas and Natali, for I was very lucky to have you as trainers, you shared all your experience with me with passion and patience. Special acknowledgments I have to Morgan, you have being a great teacher, thanks you for the time, the advice, the respect and for sharing your understanding and knowledge with me any time. Thanks Simon and Pau for building this experiment with me, next time it is going to be even better! thank you very much Martijn and all our summer students, your time in the lab was short but essential.

I thank the members of the IT team and the electronic and mechanical workshops of ICFO, specially to Xavi who was always efficient and happy to collaborate with us proposing alternatives to improve our designs. Thanks to logistics who, ever since the first day we had to paint the walls of the lab, have given me their support and friendship.

All my gratitude to all my friends: you two great women, Paski and Asia, and you great guys Ronney, Fer and James. To all the rest of los puercos: Mike, Juan, Miriam, Lisa, Pau and of course Gio. Thanks for the beautiful days and crazy evenings. I have learned many things about people and life with you all, thanks for making me question my ideas and judgements, there is no better way to become a better person. For the same reasons I thank you Felix, and also for your interest and feedback on this work and for the fervid and motivating discussions on so many other topics.

Finalmente agradezco a mi mayor fuente de felicidad que es y siempre será mi familia. Gracias a todos por el cariño, la motivación y la confianza, por las risas y las lágrimas, por dejar claro que el amor no es mermado por la distancia ni el tiempo.

CONTENTS

ACRONYMS

AM amplitude modulated

AOM acousto optic modulator

BEC Bose-Einstein condensate

CPL coupler

DSHI delayed self-heterodyne interferometer

EDFA Erbium doped fiber amplifier

ECDL Extended cavity diode lasers

FM frequency modulated

FWHM full width at half maximum

FWM four-wave mixing

G_1 coupling factor of the vectorial part of the light-atom interaction Hamiltonian

G_2 coupling factor of the tensorial part of the light-atom interaction Hamiltonian

IR infrared

LO local oscillator

MDDI magnetic dipole-dipole interactions

MTF modulation transfer function

MOT magneto optical trap

MTS modulation transfer spectroscopy

N number of atoms

N_L number of photons

ODT optical dipole trap

PD photo diode

PI proportional-integral

PPLN periodically poled Lithium Niobate

PZT piezo-electric transducer

RAM residual amplitude modulation

spinor BEC spinor Bose-Einstein condensate

T temperature

TIA transimpedance amplifier

VCO voltage controlled oscillator

VGA variable gain amplifier

1 PREFACE

Over the last twenty-two years, from the first creation of a dilute gas Bose-Einstein condensate (BEC) [Anderson et al., 1995], many fruitful studies have contributed to the field. These studies have greatly extended the knowledge of fundamental phenomena. They have also contributed to developing tools to bring about the next generation of technologies that will exploit quantum physics. The complex setups of the pioneering works have been miniaturized to a single chip [Wildermuth et al., 2006; Hansel W. et al., 2001; Wang et al., 2005] and the production rates have been lowered to a few seconds [Barrett et al., 2001; Clément et al., 2009; Olson et al., 2013].

Although a different condensed system, liquid He, was created and extensively studied before the dilute condensates, much physics such as the understanding of weakly interacting systems and interferometry with atomic waves, eluded observation until dilute condensates appeared. The excitement for studying the new open physics brought many people to the field. After a few years many of the original used techniques had been greatly improved. One example is the realization of optical dipole traps that enabled the possibility to confine arbitrary spin states [Stamper-Kurn et al., 1998; Barrett et al., 2001]. This opened a new subfield for the study of a system with additional degrees of freedom in the spin space, which is today known as a spinor Bose-Einstein condensate (spinor BEC).

Spinor BECs are interesting and useful for several fundamental and practical reasons. Theoretical studies have predicted rich phenomena in multicomponent BEC such as entanglement, spin squeezing, spin-wave formation and suppression of quantum phase diffusion [Duan et al., 2002; Müstecaplıoğlu et al., 2002; Gu et al., 2004; Law et al., 1998]. These results are useful for quantum information and interferometry. In a spinor condensate, interactions between atoms allow the observation of macro-

scopic phenomena such as Schrödinger cat states [Cirac et al., 1998; Pietilä and Möttönen, 2009] and Dirac monopoles [Ray M. W. et al., 2014; Savage and Ruostekoski, 2003]. There are regimes of ultralow magnetic field predicted to lead to a spontaneous superfluid flow of atoms or to strong spin oscillations, particularly interesting in the field of magnetometry.

In the field of quantum metrology applied to atomic sensors, the standard theory [Budker and Romalis, 2007] situates a spinor BEC system in the most promising regime to detect magnetic fields with high spatial and temporal resolution: due to its symmetries and internal interactions, inhomogeneous response of the atoms is forbidden. Some groups have exploited the spatial advantages of spinor condensates as a 2D spatially resolved magnetometer [Higbie, 2005]. In addition, BEC systems have proven very efficient at generating metrologically-useful entanglement, which allows a spinor sensor to surpass the standard quantum limit of sensitivity [Muessel et al., 2014; Brask et al., 2015].

These possibilities motivated the construction of a ferromagnetic spinor condensate. In the long term, we would take advantage of the experience of our group demonstrating squeezing of cold atoms and light states [Wolfgramm et al., 2010; Sewell et al., 2012; Wolfgramm et al., 2013; Colangelo et al., 2017] to apply these techniques on our own system and try to combine them. We gained particular motivation to study the ferromagnetic phase transition and its relation to condensation, a question that has being studied in many theoretical works [Yamada, 1982; Gu and Klemm, 2003; Poluektov and Savchenko, 2015] with no clear experimental answer.

Part I

MATHEMATICAL DESCRIPTION OF FARADAY MEASUREMENTS OF SPIN-1 CONDENSATES

2

LIGHT-ATOM INTERACTION: FARADAY ROTATION

2.1 STOKES OPERATORS

The state of polarization of a plane wave is described classically in terms of the Stokes parameters and quantum mechanically by its analogous operators:

$$\hat{S}_0 = \frac{1}{2}\left(\hat{a}_+^\dagger \hat{a}_+ + \hat{a}_-^\dagger \hat{a}_-\right) \qquad \hat{S}_x = \frac{1}{2}\left(\hat{a}_+^\dagger \hat{a}_- + \hat{a}_-^\dagger \hat{a}_+\right) \tag{1}$$
$$\hat{S}_y = \frac{i}{2}\left(\hat{a}_-^\dagger \hat{a}_+ - \hat{a}_+^\dagger \hat{a}_-\right) \qquad \hat{S}_z = \frac{1}{2}\left(\hat{a}_+^\dagger \hat{a}_+ - \hat{a}_-^\dagger \hat{a}_-\right)$$

expressed in terms of the Schwinger boson operators ($\hat{a}_\pm^\dagger$ and $\hat{a}_\pm$) representing the creation and annihilation of a photon with $\pm$ polarization [Geremia et al., 2006]. Another useful form to represent these operators is in terms of the two component operator $(\hat{a}_+\ \hat{a}_-)^T$ and the Pauli matrices σ_μ (for $\mu = x, y, z$) plus the identity (for $\mu = 0$) [Jauch and Rohrlich, 1976]:

$$\hat{S}_\mu = \frac{1}{2}(\hat{a}_+^*\ \hat{a}_-^*)\sigma_\mu(\hat{a}_+\ \hat{a}_-)^T. \tag{2}$$

With the last expression it is easy to demonstrate the commutation relation $[\hat{S}_x, \hat{S}_y] = i\hat{S}_z$ and cyclic permutations and $[\hat{S}_\mu, \hat{S}_0] = 0$. We can interpret the expected value of those operators as half the difference in the number of photons in the different bases: $\langle \hat{S}_x \rangle$ represent those in the H-V linear basis, $\langle \hat{S}_y \rangle$ in the $\pm 45°$ basis, and $\langle \hat{S}_y \rangle$ in the circular basis. $\langle \hat{S}_0 \rangle$ accounts for the total number of photons.

2.2 SPIN OPERATORS

A spin-1 system is in the most general way described by a density matrix with eight degrees of freedom, we can therefore represent it in terms of eight linearly independent generators. Such a representation can be made in terms of the 3x3 Gell-Mann matrices which are a generalization of the Pauli matrices for a spin-1/2 system. Equivalently, a spin-1 system can be represented in therms of the spin operators: [Colangelo et al., 2013] $\{\hat{\lambda}\} = \{\hat{f}_x, \hat{f}_y, \hat{f}_z, \hat{j}_x, \hat{j}_y, \hat{j}_k, \hat{j}_l, \hat{j}_m\}$. The single atoms orientation operators $\hat{f}_x, \hat{f}_y, \hat{f}_z$ are defined as:

$$\hat{f}_x = \frac{1}{\sqrt{2}}\begin{pmatrix} 0 & 1 & 0 \\ 1 & 0 & 1 \\ 0 & 1 & 0 \end{pmatrix}, \hat{f}_y = \frac{i}{\sqrt{2}}\begin{pmatrix} 0 & -1 & 0 \\ 1 & 0 & -1 \\ 0 & 1 & 0 \end{pmatrix}, \hat{f}_z = \begin{pmatrix} 1 & 0 & 0 \\ 0 & 0 & 0 \\ 0 & 0 & -1 \end{pmatrix} \quad (3)$$

which follow the commutation relation $[\hat{f}_i, \hat{f}_j] = i\epsilon_{ijk}\hat{f}_k$. Whereas the alignment variables take the form:

$$\begin{aligned} \hat{j}_x &= \hat{f}_x^2 - \hat{f}_y^2 & \hat{j}_y &= \hat{f}_x\hat{f}_y + \hat{f}_y\hat{f}_x \\ \hat{j}_k &= \hat{f}_x\hat{f}_z + \hat{f}_z\hat{f}_x & \hat{j}_l &= \hat{f}_y\hat{f}_z + \hat{f}_z\hat{f}_y \\ \hat{j}_m &= \frac{1}{\sqrt{3}}(2\hat{f}_z^2 - \hat{f}_x^2 - \hat{f}_y^2) \end{aligned} \quad (4)$$

These matrices obey the ortho-normalization condition $\mathrm{Tr}[\hat{\lambda}_i\hat{\lambda}_j] = 2\delta_{ij}$.

In terms of the $\{\hat{\lambda}\}$ basis we can expand the spin-1 density matrix as:

$$\begin{aligned} \hat{\rho} =& \frac{1}{3}\mathbb{1} + \frac{1}{2}\sum_{i=1}^{8}\langle\hat{\lambda}_i\rangle\hat{\lambda}_i \\ =& \frac{1}{3}\mathbb{1} + \frac{1}{2}\sum_{i=1}^{3}\langle\hat{f}_i\rangle\hat{f}_i + \frac{1}{2}\sum_{i=1}^{5}\langle\hat{j}_i\rangle\hat{j}_i \end{aligned} \quad (5)$$

where the expected values are given by $\langle\hat{\lambda}_i\rangle = \mathrm{Tr}[\hat{\rho}\hat{\lambda}_i]$. This means that the density matrix of a spin-1 system can always be

represented by the expectation values of eight observables, three of which are vector quantities and five of which are second-order tensor quantities [Hofmann and Takeuchi, 2004].

For a many body system we define the collective spin operators:

$$\hat{F}_i = \sum^{N} \hat{f}_i \qquad \text{and} \qquad \hat{J}i = \sum^{N} \hat{j}_i \tag{6}$$

for the number of atoms (N). For convenience we also define $\hat{F}_\pm = \hat{F}_x \pm i\hat{F}_y$, as well as the commutation relations $[\hat{F}_z, \hat{F}_\pm] = \pm\hat{F}_\pm$.

2.3 LIGHT-ATOM INTERACTION: IRREDUCIBLE HAMILTONIAN

The interaction Hamiltonian describing off resonant light interacting with an atom in the ground state with angular momentum f has been studied under the rotating wave approximation, by [Le Kien et al., 2013; Geremia et al., 2006]. They show that such a Hamiltonian can be effectively expanded as a sum of terms containing the different irreducible spherical tensor components of the polarizability tensor $\overleftrightarrow{\alpha}(f, f') = \alpha^{(0)}_{f,f'} + \alpha^{(1)}_{f,f'} + \alpha^{(2)}_{f,f'}$ as:

$$\hat{\mathcal{H}}^{(0)} = \alpha^{(0)} \frac{2}{3} \hat{S}_0 \mathbb{1}, \tag{7}$$

$$\hat{\mathcal{H}}^{(1)} = \alpha^{(1)} \hat{S}_z \hat{f}_z, \tag{8}$$

$$\hat{\mathcal{H}}^{(2)} = \alpha^{(2)} \left\{ \hat{S}_x \hat{j}_x + \hat{S}_y \hat{j}_y + \hat{S}_0 \left[3\hat{f}_z^2 - f(f+1)\mathbb{1} \right] /3 \right\} \tag{9}$$

where $\alpha^{(i)} = G \sum_{f'} \alpha^{(i)}_{f,f'} / \Delta_{f,f'}$, $\Delta_{f,f'} \equiv \omega - \omega_{f,f'}$ being the detuning of the probe frequency ω with respect to the atomic resonance frequency $\omega_{f,f'}$ of the transition $|f\rangle \to |f'\rangle$, $G = \omega/(2\epsilon_0 V)$ the form factor for the volume of the cloud V, and [Geremia et al., 2006; Stockton, 2007]:

$$\begin{aligned}
\alpha^{(0)}_{f,f'} =& \alpha^{f'}_{f}\left[(2f-1)\delta^{f'}_{f-1} + (2f+1)\delta^{f'}_{f} + (2f+3)\delta^{f'}_{f+1}\right], \\
\alpha^{(1)}_{f,f'} =& \alpha^{f'}_{f}\left[-\frac{2f-1}{f}\delta^{f'}_{f-1} - \frac{2f+1}{f(f+1)}\delta^{f'}_{f} + \frac{2f+3}{f+1}\delta^{f'}_{f+1}\right], \\
\alpha^{(2)}_{f,f'} =& \alpha^{f'}_{f}\left[\frac{1}{f}\delta^{f'}_{f-1} - \frac{2f+1}{f(f+1)}\delta^{f'}_{f} + \frac{1}{f+1}\delta^{f'}_{f+1}\right],
\end{aligned} \tag{10}$$

$$\alpha^{f'}_{f} = \alpha_0(2j'+1)\left|\begin{Bmatrix} 1 & j & j' \\ i & f' & f \end{Bmatrix}\right|^2, \tag{11}$$

$$\alpha_0 = \frac{3\epsilon_0\hbar\Gamma\lambda^3}{8\pi^2} \tag{12}$$

where $\delta^{f'}_{f}$ is the Kronecker delta, Γ the spontaneous emission rate and λ the transition wavelength. i is the nuclear spin quantum number, $j(j')$ the total electron angular momentum quantum number of the ground (excited) state, and $f(f')$ the total angular momentum quantum number for the ground (excited) state.

2.3.1 *Scalar term*

Equation 7 is the scalar term of the Hamiltonian and refers to the light polarization and spin state-independent light shift. Together with $\hat{S}_0$-containing terms in $\hat{\mathcal{H}}^{(2)}$, it represents the AC stark shift exploited in the creation of a spatial dependent potential which is the dipole trap. The dipole potential will be approximated by neglecting the tensorial terms as they represent spin-dependent corrections around 1% of the scalar light shift. See Section 5.3.3.

2.3.2 *Faraday Interaction*

The rank-1 Hamiltonian $\hat{\mathcal{H}}^{(1)}$ contains the vectorial part of the polarizability and describes how a spin component along $\mathbf{z}$ of the angular momentum of the atoms induces a differential phase shift between the circular polarization components of the probe

light. This is an induced birefringence like the familiar Faraday effect.

We write the interaction Hamiltonian between the light an a collection of atoms as the sum of the interaction Hamiltonians describing the interaction of the field with with each atom: $\hat{H}_F = \sum^N \hat{\mathcal{H}}^{(1)}$. The linearity of Equation 6 allows us to express this interaction Hamiltonian in terms of the collective spin operator:

$$\hat{H}_F = \frac{\hbar G_1}{\tau_p} \hat{S}_z \hat{F}_z. \tag{13}$$

In this expression τ_p represents the total interaction time and the dimensionless parameter coupling factor of the vectorial part of the light-atom interaction Hamiltonian (G_1) accounts for both the polarizability and the geometrical factors that modify the effective interaction strength. Note, that this Hamiltonian couples directly to the magnetic quantum number m_F through $\hat{F}_z$, and looks like the usual linear Zeeman effect Hamiltonian $\hat{H}_{Z1} \propto B_z \hat{F}_z$. Therefore the vector component Hamiltonian acts like an effective magnetic field for the atoms with the addition that spatial variations on the polarization state could result in an effective magnetic field gradient across the atoms. [Jasperse, 2015]

2.3.3 *Tensorial lightshift*

The final expression for the Hamiltonian, the tensorial $\hat{\mathcal{H}}^{(2)}$, induces ellipticity on a linearly polarized input beam. When the system is a pseudospin 1/2 this term vanishes as shown by [Kubasik et al., 2009; de Echaniz et al., 2008]. The tensor lightshift drops faster with detuning than do the vectorial shifts, for which it has been predicted that the case of a very far detuned probe beam where the detuning is larger than the hyperfine splitting of the excited state (and therefore negligible), a ^{87}Rb atom in $|F = 1\rangle$ effectively behaves as a pseudospin 1/2 system. Some works, nevertheless, have demonstrated signatures where the system behaves not like a psin 1/2 system no matters how large the detuning is [Koschorreck et al., 2010a; Stockton, 2007].

The terms proportional to the alignment operators, and therefore quadratically dependent on the orientation operators, together with the Zeeman interaction Equation 20, may induce collapses and revivals on the Faraday interaction, depending on the polarization orientation of the probe beam [Smith et al., 2004]. It is possible to find a polarization angle for which the tensorial contribution can be neglected, the so called magic angle $\phi_{magic} = 54.7°$ relative to the bias field orientation.

2.4 DYNAMICS

We can write the evolution operator neglecting the terms with $\hat{S}_0$ which commutes with all the Stokes parameters:

$$\mathcal{U}(t) = e^{-\frac{i}{\tau_p}[G_1 \hat{S}_z \hat{F}_z + G_2(\hat{S}_x \hat{J}_x + \hat{S}_y \hat{J}_y)]t} \tag{14}$$

for the collective spin operators and the effective coupling factor of the tensorial part of the light-atom interaction Hamiltonian (G_2). This coupling constant is typically orders of magnitude lower than G_1 and therefore we will focus on the G_1 term. This evolution operator acts on the Stokes operators as:

$$\begin{aligned}
\hat{S}_y(t) =& \mathcal{U}^\dagger \hat{S}_y \mathcal{U} \\
=& e^{\frac{i}{\tau_p} G_1 \hat{S}_z \hat{F}_z \tau_p} \hat{S}_y(0) e^{-\frac{i}{\tau_p} G_1 \hat{S}_z \hat{F}_z \tau_p} \\
=& \hat{S}_y(0) \cos G_1 \hat{F}_z + \hat{S}_x(0) \sin G_1 \hat{F}_z && (15) \\
=& \hat{S}_y(0) \cos\theta + \hat{S}_x(0) \sin\theta && (16)
\end{aligned}$$

and analogously:

$$\begin{aligned}
\hat{S}_x(t) =& \hat{S}_x(0) \cos\theta - \hat{S}_y(0) \sin\theta && (17) \\
\hat{S}_z(t) =& \hat{S}_z(0) && (18)
\end{aligned}$$

where we identify $\theta = G_1 \hat{F}_z$ as the Faraday rotation angle.

If the probing light is linearly polarized such that: $\langle \hat{S}_y(0) \rangle = \langle \hat{S}_z(0) \rangle = 0, \langle \hat{S}_x(0) \rangle = N_L/2$ for the number of photons (N_L), the expected values are simply:

$$\begin{aligned} \langle \hat{S}_x(t) \rangle &= \frac{N_L}{2} \cos\theta \\ \langle \hat{S}_y(t) \rangle &= \frac{N_L}{2} \sin\theta \\ \langle \hat{S}_z(t) \rangle &= 0 \end{aligned} \tag{19}$$

3

ZEEMAN INTERACTION

Let's consider the case of a spin ensemble in the presence of a constant magnetic field $B_z\mathbf{z}$. The Breit-Rabi expression for the energy shifts of a ^{87}Rb atom in the ground state ($S = 1/2$, $L = 0$, $J = 1/2$, $I = 3/2$) in the presence of a magnetic field reads: $E_Z = -\Delta E_{hf}/8 \pm \Delta E_{hf}/2(1 + 4m_F x/(2I+1) + x^2)^{1/2} + g_I \mu_B m_F B$ where $x = (g_J - g_I)\mu_B B_z/\Delta E_{hf}$ for ΔE_{hf} being the energy splitting between hyperfine states, g is the Landé $g-$factor for the electronic configuration ($g_I \simeq 1 \times 10^{-3}$, $g_J \simeq 2$) [Breit and Rabi, 1931; Steck, 2001]. It is useful to expand E_Z in its Taylor series and approximate it to second order in magnetic field, which leads to the following Hamiltonian [Kawaguchi and Ueda, 2012]:

In this thesis $\mathbf{x}$, $\mathbf{y}$ *and* $\mathbf{z}$ *represent the unit vectors along the given direction.*

$$\begin{aligned}\hat{H}_Z =& \hat{H}_{Zl} + \hat{H}_{Zq},\\ \simeq& \frac{g_J}{4}\mu_B B_z \hat{F}_z + \frac{(g_J \mu_B)^2}{16\Delta E_{hf}} B_z^2 \hat{F}_z^2,\\ \simeq& g_F \mu_B B_z \hat{F}_z + \frac{(g_F \mu_B B_z)^2}{\Delta E_{hf}} \hat{F}_z^2,\end{aligned} \tag{20}$$

where μ_B is the Bohr magneton. The first term is referred to as the linear Zeeman shift and the second term as the quadratic Zeeman shift. In the hyperfine ground state of ^{87}Rb , $|F = 1(2)\rangle$, $g_F = -(+)1/2$ and $\Delta E_{hf} = +(-)6.8\,\text{GHz}$.

The evolution of the spin operators under the linear part of the Hamiltonian is given by the operator:

$$\mathcal{U} = e^{-iH_{Zl}t/\hbar} = e^{-i\omega_L t \hat{F}_z}, \tag{21}$$

where we have defined the Larmor frequency $\omega_L = g_F \mu_B B_z/\hbar$. Expanding $\mathcal{U}$ into its Taylor series we find the useful expression:

$$\mathcal{U} = e^{-i\omega_L t \hat{F}_z} = \mathbb{1} - i\sin(\omega_L t)\hat{F}_z + [\cos(\omega_L t) - 1]\hat{F}_z^2, \tag{22}$$

where we have used the fact that for $F = 1$ and integer k, $\hat{F}_z^{2k} = \hat{F}_z^2$ and $\hat{F}_z^{2k+1} = \hat{F}_z$. The spin operators evolve as follows:

$$\begin{aligned}\hat{F}_z(t) &= \hat{F}_z(0), \\ \hat{F}_y(t) &= \cos(\omega_L t)\hat{F}_y(0) - \sin(\omega_L t)\hat{F}_x(0), \\ \hat{F}_x(t) &= \cos(\omega_L t)\hat{F}_x(0) + \sin(\omega_L t)\hat{F}_y(0).\end{aligned} \tag{23}$$

From Equation 23 it is straight forward to see, that the atoms undergo Larmor precession at a frequency ω_L on the plane xy.

Before studying the evolution due to the quadratic Zeeman part of the Hamiltonian let's consider the more general case when the magnetic field is a function of time.

Time dependent magnetic field

In this section we will detail the dynamics due to the linear and quadratic contributions in the general case when the magnetic field exhibits time dependent noise on top of its main value causing Larmor precession.

Completely analogous to Equation 20, we can describe the interaction between the atoms and a time dependent magnetic field $\mathbf{B}(t) = B_z(t)\mathbf{z}$ with the Hamiltonian:

$$\hat{H}_Z = g_F \mu_B B_z(t)\hat{F}_z + \frac{[g_F \mu_B B_z(t)]^2}{\Delta E_{hf}}\hat{F}_z^2. \tag{24}$$

the evolution operator is then given by:

$$\begin{aligned}\mathcal{U} &= \exp\left\{-\frac{i}{\hbar}\int \hat{H}(t')dt'\right\} \\ &= \exp\left\{-\frac{i g_F \mu_B}{\hbar}\hat{F}_z \int B_z(t')dt' - \frac{i(g_F\mu_B)^2}{\hbar \Delta E_{hf}}\hat{F}_z^2 \int B_z^2(t')dt'\right\} \\ &\equiv \exp\left\{-i\Theta_L(t)\hat{F}_z - i\Theta_Q(t)\hat{F}_z^2\right\}\end{aligned} \tag{25}$$

where we have defined:

$$\Theta_L(t) = \frac{g_F \mu_B}{\hbar} \int_0^t B_z(t')dt' \tag{26}$$

$$\Theta_Q(t) = \frac{(g_F \mu_B)^2}{\hbar \Delta E_{hf}} \int_0^t B_z^2(t')dt' \tag{27}$$

We have seen before that the linear part of the Hamiltonian acts on the spin operators such that:

$$\begin{aligned} \hat{F}_z(t) &= \hat{F}_z(0), \\ \hat{F}_x(t) &= \cos(\Theta_L(t))\hat{F}_x(0) + \sin(\Theta_L(t))\hat{F}_y(0), \\ \hat{F}_y(t) &= \cos(\Theta_L(t))\hat{F}_y(0) - \sin(\Theta_L(t))\hat{F}_x(0). \end{aligned} \tag{28}$$

The evolution operator for the quadratic part of the Hamiltonian $\mathcal{U}_Q$, on the other hand, can be written in matrix form:

$$\mathcal{U}_Q = \exp\{-i\Theta_Q(t)\hat{F}_z^2\}, \tag{29}$$

$$= \begin{pmatrix} e^{-i\Theta_Q} & 0 & 0 \\ 0 & 1 & 0 \\ 0 & 0 & e^{-i\Theta_Q} \end{pmatrix}, \tag{30}$$

using the expression $e^{i\omega t \hat{F}_z^2} = \mathbb{1} + \hat{F}_z^2 \left(e^{i\omega t} - 1\right)$. This relation is true since $\hat{F}_z^{2n} = \hat{F}_z^2$ for $F = 1$. The evolution of the spin operators under $\mathcal{U}_Q$ is then given by:

$$\begin{aligned} \hat{F}_z(t) &= \hat{F}_z(0), \\ \hat{F}_x(t) &= \cos(\Theta_Q(t))\hat{F}_x(0) - \sin(\Theta_Q(t))\hat{J}_l(0), \\ \hat{F}_y(t) &= \cos(\Theta_Q(t))\hat{F}_y(0) + \sin(\Theta_Q(t))\hat{J}_k(0). \end{aligned} \tag{31}$$

Notice that spin alignment now enters caused by the quadratic Zeeman interaction (see Equation 4 and Equation 6).

The evolution under the complete Hamiltonian $\hat{H}_Z$, $\mathcal{U} = \mathcal{U}_\mathcal{L}\mathcal{U}_Q$ can then be expressed as: $(\mathcal{U}_\mathcal{L}\mathcal{U}_Q)^\dagger \hat{O}\mathcal{U}_\mathcal{L}\mathcal{U}_Q = \mathcal{U}_\mathcal{L}{}^\dagger \mathcal{U}_Q{}^\dagger \hat{O}\mathcal{U}_Q\mathcal{U}_\mathcal{L}$ because the operators $\hat{F}_z, \hat{F}_z^2$ commute. Applying the transformations we get:

$$
\begin{aligned}
\mathcal{U}^\dagger \hat{F}_x \mathcal{U} =& \mathcal{U}_\mathcal{L}{}^\dagger \mathcal{U}_Q{}^\dagger \hat{F}_x \mathcal{U}_Q \mathcal{U}_\mathcal{L} \\
=& \mathcal{U}_\mathcal{L}{}^\dagger \left[\cos(\Theta_Q)\hat{F}_x(0) - \sin(\Theta_Q)\hat{J}_l(0)\right] \mathcal{U}_\mathcal{L}, \\
=& \cos(\Theta_Q)\left[\cos(\Theta_L)\hat{F}_x(0) + \sin(\Theta_L)\hat{F}_y(0)\right] \\
& - \sin(\Theta_Q)\left[\cos(\Theta_L)\hat{J}_l(0) + \sin(\Theta_L)\hat{J}_k(0)\right] \\
=& \cos(\Theta_Q)\cos(\Theta_L)\hat{F}_x(0) + \cos(\Theta_Q)\sin(\Theta_L)\hat{F}_y(0) \\
& - \sin(\Theta_Q)\cos(\Theta_L)\hat{J}_l(0) - \sin(\Theta_Q)\sin(\Theta_L)\hat{J}_k(0)
\end{aligned}
\tag{32}
$$

and analogously:

$$
\begin{aligned}
\mathcal{U}^\dagger \hat{F}_y \mathcal{U} =& \cos(\Theta_Q)\cos(\Theta_L)\hat{F}_y(0) - \cos(\Theta_Q)\sin(\Theta_L)\hat{F}_x(0) \\
& + \sin(\Theta_Q)\cos(\Theta_L)\hat{J}_k(0) - \sin(\Theta_Q)\sin(\Theta_L)\hat{J}_l(0)
\end{aligned}
\tag{33}
$$

$$
\mathcal{U}^\dagger \hat{F}_z \mathcal{U} = \hat{F}_z \tag{34}
$$

where we have omitted the time dependence of the angles. From these results we can see that not only a coherent rotation of the orientation is expected, but also alignment-to-orientation conversion. Most important is to notice the time dependence of Θ_Q which is the integral in time of the magnetic field squared. This causes a drift to Θ_Q due to the variance of the magnetic field noise, an effect that accumulates in time even when the noise is symmetric about zero.

To illustrate the main dynamics of the spin operator we consider the simplest case, when the magnetic field is constant. Assuming the initial conditions: $\langle \hat{F}_x(0) \rangle = F_x$ and $\langle \hat{F}_{z,y}(0) \rangle = 0$, the evolution of the spin operator $\hat{F}_x$ is simply given by an amplitude modulated signal: $\cos(\omega_L t)\cos(\omega_Q t)F_x$, with oscillating frequency $\omega_L = g_F \mu_B B_z/\hbar$ modulated at $2\omega_Q$, with $\omega_Q = (g_F \mu_B B_z)^2/(\hbar \Delta E_{hf})$. This describes a coherent dynamics during the full evolution time, as shown in Figure 1.

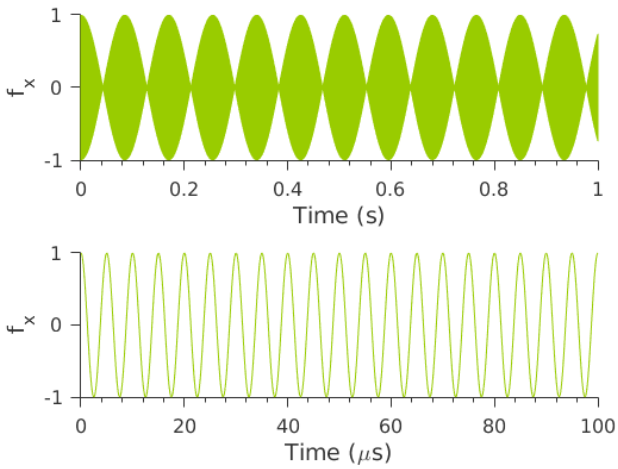

Figure 1: Spin projection on the axis **x** over long (upper graph) and short (lower graph) time scales under a constant Bz = 28.6 µT. At this field the amplitude modulation caused by the quadratic Zeeman shift occurs on ~ 100 ms time-scales.

4

BASIC CONCEPTS OF MEAN-FIELD THEORY OF SPINOR CONDENSATES

4.1 INTRODUCTION

Describing a system of bosons is a many-body problem in which individual particles affect each other. In the simplest case, when the different particles don't interact one can simply write the field operator describing the system as the product of single-particle field operators, if the particles are bosons and all occupy the single-particle ground state $\hat{\phi}_0(\mathbf{r})$, the N-particle field operator is of the form:

$$\hat{\psi}(\mathbf{r}) \equiv \hat{\psi}(\mathbf{r}_1, ..., \mathbf{r}_N) = \prod_1^N \hat{\phi}_0(\mathbf{r}_i), \tag{35}$$

which is the Hartree approximation [Pethick and Smith, 2002] . The problem then reduces to solving the one particle Schrödinger equation, where the total energy of the N-particle system is simply the energy of one particle times N. This approach gives a good intuition about the kinetic properties of a condensate of ultracold atoms, which are very dilute and very weakly interacting systems. Nevertheless, other interesting properties arise from the interaction between bosons and therefore a more sophisticated treatment is needed.

If one is to include interactions between bosons a many-body Schrödinger equation has to be solved. Numerically solving this problem has a very high computational cost when the number of particles is of the order of 10^5 as in typical experiments. In dilute gases this many-body problem can be simplified by considering the effect of individual particles as an average or mean action of the fluid, ignoring in this way quantum fluctuations and correlations between particles. The description in terms of a field

operator $\hat{\psi}^\dagger$, which creates one boson in a given spatial mode, is replaced by a classical field which is its mean value or expectation value on the vacuum: $\psi(\mathbf{r}) \equiv \langle vac|\hat{\psi}(\mathbf{r})|vac\rangle = \sqrt{N}\phi_0(\mathbf{r})$, which is known as the condensate wavefunction. Equation 35 means that all the atoms are in the one particle ground state, with no possibility to excite to other spatial modes. We note that $\int d\mathbf{r}|\psi(\mathbf{r})|^2 = N\int d\mathbf{r}|\phi(\mathbf{r})|^2 = N$, where the second equality follows from the normalization condition on ϕ. This motivates the identification of $|\psi(\mathbf{r})|^2$ as the local density $n(\mathbf{r})$. Within this mean-field picture, particle interactions are described via a pseudopotential in the Hamiltonian that governs the evolution of the condensate wavefunction. It is assumed only binary low energy collisions take place, as will be justified in Section 4.3. When such a pseudopotential is included in the Hamiltonian, the problem is described by a nonlinear Schrödinger equation known as Gross-Pitaevskii equation (see Section 4.4).

While mean field theory can describe many important phenomena like vortices and spin waves, it has no way to describe microscopic correlations. Effects like the creation of Efimov states can not be properly described in this picture. Theoretical methods to handle such scenarios such as perturbation theory on the mean field have been made [Bogolyubov, 1947; Mazzanti et al., 2003].

In this mean-field construction of the condensate wavefunction we have define it to as a complex number which has a well-defined phase in contrast to the operator $\hat{\psi}(\mathbf{r})$. This means that in this picture condensation breaks the gauge symmetry of the many-body system.

Additional internal degrees of freedom can be added to this problem, such as the internal spin state of the atoms. This represent extra dimensions in the Hilbert space as atoms in the spatial ground state can change spin state. A condensate of spin-F particles, known as spinor Bose-Einstein condensate, can then be represented as a vectorial wavefunction with $2F+1$ components, and therefore a much richer dynamics where the spatial and internal degrees of freedom interplay is expected.

In the following sections we write the equations that describe spinor Bose-Einstein condensates in the mean field approxima-

tion. Although this theory seems to be a very restrictive one, it has been very successful explaining current experiments with spinor condensates [Chang et al., 2004, 2005; Jacob et al., 2012]

4.2 MATHEMATICAL REPRESENTATION OF SPINOR CONDENSATES

The system described above considers that only one single particle quantum state is macroscopically occupied. A spinor condensate nevertheless is a system where the atoms, although in the motional ground state, have the possibility to occupy different internal states and go from one sate to another; in contrast to mixtures of several species where the populations in each component are strictly conserved. This implies that a spinor condensate cannot be described by the product of single components defining a scalar field operator $\hat{\psi}(\mathbf{r})$.

A spin-F condensate is rather described by a vectorial field operator which has 2F components: $\hat{\Psi}(\mathbf{r}) = \left(\hat{\psi}_{-m}(\mathbf{r}), ..., \hat{\psi}_0(\mathbf{r}), ..., \hat{\psi}_m(\mathbf{r})\right)^T$, one per each internal state. In the case of ^{87}Rb in the $F = 1$ hyperfine ground state, the order parameter has three components, one for each magnetic sublevel $m = -1, 0, 1$:

$$\hat{\Psi}(\mathbf{r}) = \left(\hat{\psi}_{-1}(\mathbf{r}), \hat{\psi}_0(\mathbf{r}), \hat{\psi}_1(\mathbf{r})\right)^T \tag{36}$$

In the Hartree approximation we can assume all the atoms occupy a single particle state which is a linear superposition of spin states, and therefore the many-body wave function can be written as the product of single particle vectorial wavefunctions.

In the mean field approximation we write the order parameter as:

$$\Psi(\mathbf{r}) = \langle\hat{\Psi}(\mathbf{r})\rangle = (\psi_{-1}(\mathbf{r}), \psi_0(\mathbf{r}), \psi_1(\mathbf{r}))^T \tag{37}$$

where each ψ_m contains the motional ground state wavefunction ϕ_0 and a spinor component:

$$\psi_m(\mathbf{r}) = \langle\hat{\psi}_m(\mathbf{r})\rangle = \sqrt{n(\mathbf{r})}\zeta_m(\mathbf{r})\phi_0. \tag{38}$$

$\zeta = (\zeta_{-1}, \zeta_0, \zeta_1)$ is a three component spinor with the normalization condition $|\zeta| = 1$, such that:

$$n(r) = \sum_{m=-1}^{1} |\psi_m(\mathbf{r})|^2 \tag{39}$$

The representation basis for the spin state is generally chosen for the quantization to be along $\mathbf{z}$, and therefore $\{|-1\rangle, |0\rangle, |1\rangle\}$ are the eigenstates of the spin operator $\hat{f}_z$.

The spin state is characterized by the spinor with components $\zeta_m = \sqrt{\rho_m} \exp\{i\phi_m\}$. Where ρ_m is the population in the m state. The difference $\rho_1 - \rho_{-1}$ indicates a net longitudinal magnetization along the quantization axis. The coherences, on the other hand, indicate transverse magnetization.

4.3 COLLISIONS

Alkali atoms are in their electronic ground state where only hyperfine levels define different collisional channels. The interactions between pair of atoms in modeled by a simple repulsion of hard spheres,covalent bonding and a long range Van der Waals interaction caused by the electric dipole-dipole interaction between atoms and scales like $-\alpha/r^6$(includes electrostatic, induction, dispersion, etc.). Covalent bonding make the distinction when the electrons of the two colliding atoms are in a singlet state or in a triplet state: there is an strong interaction between two electrons with opposite spin as they will try to occupy the same orbital.

In scattering theory one would write the wavefunction of the relative motion of the atoms as the sum of an incoming plane wave and a scattered one. The wave function for the center of mass motion is a plane wave whereas the wavefunction for the relative motion satisfies Schrodinger equation with the mass equal to the reduced mass $m_r = m_1 m_2/(m_1 + m_2)$. For the low energy scales of the collision we write the scattered wave as only a spherical wave$\psi = e^{ikz} + f(\theta)e^{ikr}/r$. We can then find an associated scattering length a for $\psi = 1 - a/r$ which gives the intercept

of the asymptotic wavefunction. The cross section is the defined as the connection between the scattering length and the phase shifts: $\sigma = \int |f(\theta)|^2 = 4\pi a^2$ but when considering identic particles one have to integrate in half the range to avoid double counting indistinguishable states and therefore $\sigma = 8\pi a^2$

The first assumption we make before writing a explicit form of the interaction between particles are:

1. the system is so dilute that only collisions between two particles need to be considered
2. the incident energy is so low that only the lowest order partial wave ($L_{pair}^{initial} = 0$) contributes
3. the short-range potential is rotationally invariant and therefore the total angular momentum is conserved
4. weak-dipolar approximation, whereby one neglects the spin-orbit coupling through the short-range molecular potential. Now the orbital and internal angular momenta are separately conserved
5. s-wave collisions do not mix hyperfine states

From the symmetry point of view we are constructing an interaction that preserves the full rotational symmetry of the state due to conservation of orbital angular momentum, this means the energy has to be invariant under SO(3) rotations in spin space.

Basic description of scattering of a pair of particles is usually understood as having a wavefunction of the relative motion between atoms being the sum of an incoming plane wave and a scattered wave [Pethick and Smith, 2002], which in the spherical basis can be expanded in terms of spherical harmonics as they are solution to Schrödinger equation and basis of the SO(3) group. An integer-spin state can be described in terms of the spherical harmonics [Kawaguchi and Ueda, 2012]. In this case a combination of spherical harmonics represent the many-body wavefunction being the eigenfunctions of the total spin angular momentum of the pair of atoms F_{pair} (remember $L_{pair} = 0$), and we denoted as $Y_{F_{pair}}^{m_{pair}}$. Because the wavefunction is expressed

in terms of relative coordinates, an interparticle change is an effective change of sign of the relative coordinate: $(r, \theta, \phi) \mapsto (r, -\theta, -\phi)$ which is the parity transformation in spherical coordinates. By the properties of these functions we know the parity transformation acts on the spherical harmonics as change in sign given by $(-1)^{-F_{pair}+2m_{pair}} \equiv (-1)^{-F_{pair}}$, which enforces the interaction to be such that F_{pair} is always even to keep the symmetry of the bosonic wavefunction.

Under all these assumptions we can write then the effective interaction as being composed by the sum of the terms for the two channels $F_{pair} = 0, 2$ as $U_0 = 4\pi\hbar^2 a_0/m$ and $U_2 = 4\pi\hbar^2 a_2/m$ being a the scattering lengths with values for ^{87}Rb :

hyperfine level	a_0/a_B	a_2/a_B
$F = 1$	101.8 ± 0.2	100.4 ± 0.1
$F = 2$	87.4 ± 1.0	92.4 ± 1.0

Table 1: Values of the relevant scattering lengths of ^{87}Rb atoms [Stamper-Kurn and Ueda, 2013]. a_B is the Bohr radius.

Those channels define the interaction energy given by:

$$E_{int}[\psi] = \int d\mathbf{r} \frac{n^2}{2}(c_0 + c_2|\mathbf{F}|^2) \tag{40}$$

for $c_0 = 4\pi\hbar^2(a_0 + 2a_2)/3m$, $c_2 = 4\pi\hbar^2(a_2 - a_0)/3m$, where repeated indexes indicate the sum over all magnetic states. Here $\mathbf{F} = (F_x, F_y, F_z)^T$ is the spin density vector where the components are the expected values of the orientation operators $\hat{F}_x, \hat{F}_y, \hat{F}_z$ defined in Equation 3. Explicitly:

$$F_x = \Psi^\dagger \hat{F}_x \Psi = \frac{2}{\sqrt{2}} \mathrm{Re}\{(\psi_1^* + \psi_{-1}^*)\psi_0\} \tag{41}$$

$$F_y = \Psi^\dagger \hat{F}_y \Psi = \frac{2}{\sqrt{2}} \mathrm{Im}\{(\psi_1^* - \psi_{-1}^*)\psi_0\} \tag{42}$$

$$F_z = \Psi^\dagger \hat{F}_z \Psi = |\psi_1|^2 - |\psi_{-1}|^2 \tag{43}$$

In a real system correlations between particles could lead to an occupation of exited spatial modes or depletion of the condensate. But it has been estimated to scale as $\sqrt{na_0^3}$ [Pethick and Smith, 2002] for the density n. In our experimental conditions the depletion is of the order of 0.1% and therefore the mean-field approximation should be a good description of our system.

In this section we mainly follow [Kawaguchi and Ueda, 2012]

In the mean field approximation we write the energy functional, which is the expected value of the Hamiltonian as:

$$E[\psi] = \int d\mathbf{r} \left\{ \sum_{m=-1}^{1} \psi_m^* \left[-\frac{\hbar^2}{2M}\nabla^2 + U(\mathbf{r}) \right] \psi_m + \frac{c_0}{2} n^2 + \frac{c_2}{2} |\mathbf{F}|^2 \right\} \tag{44}$$

where M is the mass of the atoms $M(^{87}\mathrm{Rb}) = 1.44316060(11) \times 10^{-25}$ kg [Steck, 2001]. $U(\mathbf{r})$ is the confining potential, normally well approximated by a harmonic oscillator. In Equation 44 we have included the interaction energy given in Equation 40.

The case of $^{87}\mathrm{Rb}$ in $F = 1$ is such that $c_2 < 0$, from the last equation we can observe the energy of the many body system is minimum when all atoms choose the same, although arbitrary oriented, pointing direction. This is, $^{87}\mathrm{Rb}$ in $F = 1$ is ferromagnetic.

In any normal experimental condition there are magnetic fields present. Usually strong static magnetic fields like earth's are compensated with induced fields, but many other sources around can make difficult to lower the noise to a level of negligible Zeeman energy. In the presence of a magnetic field $\mathbf{B} = B\mathbf{z}$, the Zeeman interaction makes a contribution to the energy given by:

$$E_Z[\psi] = \int d\mathbf{r} \sum_{m=-1}^{1} \psi_m^* \left(pm + qm^2 \right) \psi_m \tag{45}$$

where $p = g_F \mu_B B$ and $q = (g_F \mu_B B)^2 / \Delta E_{hf}$ (see Equation 20).

4.4 GROSS-PITAEVSKII EQUATION

Using the above expressions we can write the total energy functional as:

$$E[\psi] = \int d\mathbf{r} \left\{ \sum_{m=-1}^{1} \psi_m^* \left[-\frac{\hbar^2}{2M}\nabla^2 + U(\mathbf{r}) + pm + qm^2 \right] \psi_m + \frac{c_0}{2}n^2 + \frac{c_2}{2}|\mathbf{F}|^2 \right\} \tag{46}$$

from its time evolution, we can write the equations describing the mean-field dynamics of the spinor components, which are a set of three Gross-Pitaevskii equations for $m = 1, 0, -1$:

$$i\hbar\frac{\partial\psi_m}{\partial t} = \left[-\frac{\hbar^2}{2M}\nabla^2 + U(\mathbf{r}) + pm + qm^2 + c_0 n \right] \psi_m + c_2 \sum_{m'=-1}^{1} \mathbf{F}\cdot\mathbf{f}_{(m,m')}\psi_{m'}. \tag{47}$$

By comparing the kinetic energy with the interaction energy, we can determine two useful characteristic lengths: the healing length $\xi_n = \hbar/\sqrt{2Mc_0n_0}$, providing information about the density spatial variations, and the spin healing length $\xi_s = \hbar/\sqrt{2Mc_2n_0}$ which describes the length scale of spatial variations in the condensate profile induced by the spin-dependent interactions. These length scales give insights about the effective dimensionality of the problem. A spin healing length longer that the spatial dimension of the atom distribution make too energetically costly the existence of spatially varying spin distributions. In this scenario the system can be considered as spin invariant along the given direction.

In ^{87}Rb $c_0 \simeq 216c_2$ and therefore $\xi_s \simeq 15\xi_n$. This lengths together with the size of the condensate, normally interpreted as the Thomas-Fermi radius, determine the spin and atom distribution of the particular configuration.

Notice that this description is made considering a uniform system in space, however in typical experiments the spatial distribution is determined by the confining potential. A way to proceed

is to employ the single mode approximation which considers all the spin states to be in the same spatial mode. This is an accurate description when the spin-dependent interaction energy is much smaller than the spin-independent energy and the kinetic energy.

Part II

APPARATUS

5

IMPLEMENTED TECHNOLOGIES AND TECHNIQUES TO TRAP AND COOL THERMAL ATOMS

Standard techniques to cool and trap neutral atoms rely on three main forces: the scattering force, the magnetic force and the dipole force. With the passing of time, the use of a MOT became the standard technique to cool and trap neutral atoms from room temperature to a few hundreds of μK. It was first demonstrated in 1987 for sodium atoms by E. L. Raab [Raab et al., 1987] and eventually extended to all alkali atoms. A magneto optical trap (MOT) exploits the radiation-pressure force from multi scattered photons to slow down room-temperature atoms with average velocity of 300 m/s to a velocity of 150 mm/s corresponding to a few hundreds of μK. The typical acceleration the atoms experience during the cooling process is around 1×10^4 g. The cooling process exploits the Doppler effect to make the scattering rate velocity dependent (optical molasses) whereas the confining is given by spatially dependent magnetic force. For a nice description of this technique one may consult the Nobel lectures by Chu, Cohen-Tannoudji and Phillips [Chu, 1998; Cohen-Tannoudji, 1998; Phillips, 1998].

Magnetic trapping techniques do not make possible studies of spinor physics since not all spin components can be magnetically trapped. For this reason we implemented optical trapping techniques that are state-independent. Those exploit the AC stark shift effect described in Chapter 2.

In the following sections we describe the implemented technologies and techniques from ultrahigh vacuum to optical trapping. Next chapter will be fully dedicated to describe the evaporation process that leads to condensation.

5.1 VACUUM SYSTEM

The vacuum system as sketched in Figure 2 is formed by a glass cell attached to a six-way cross (CX6-40, MDC) sealed with CF40 flanges and copper gaskets (GK-150, MDC). The chamber is pumped with an ion pump that can reach an ultimate pressure of 10^{-11} T. We installed an all metal valve (MAV-150-V, MDC) to isolate the primary pump from the ion pump.

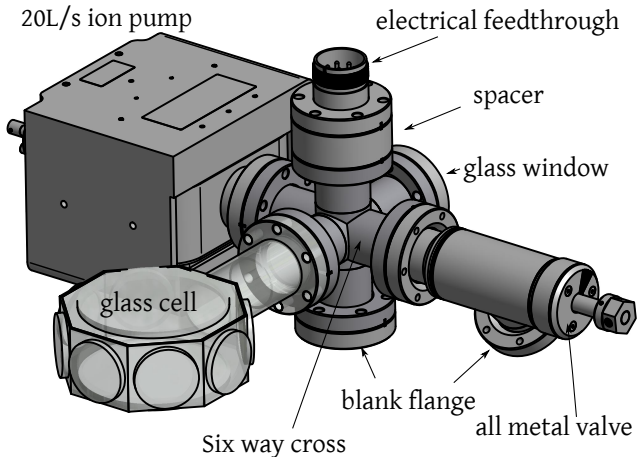

Figure 2: Vacuum system.

Glass cell

The glass cell is an Octagonal BEC Cell 4 (precision Glassblowing), which is double sided AR coated to reduce reflections on the surfaces at both 780 nm and 1560 nm wavelengths. The measured transmission is 97% in the case of 780 nm light and 99% for 1560 nm light (for the whole spectrum see Appendix C). The transmission is limited by the fact that affixing the coated windows to the cell frame requires baking to very high temperatures, which shifts the performance of the coatings in a way that cannot be accurately predicted. Before the bake-out the cell was coated to achieve more than 99% transmission at 925 nm and 1690 nm. The physical dimensions of the glass cell are shown in Appendix C.

Ion pump

The diode configuration refers to the configuration where both cathode plates are made of titanium and the anode is operated at positive high voltage.

Our ion pump (TiTan 25SVW, Gamma Vacuum) has conventional diode elements (100% Ti) that provides high pumping speeds of air and reactive gases but lower pumping speeds of noble gases. This pumping technology uses strong voltages (7 kV) and strong magnetic fields (1200 G) to accelerate free electrons in magnetron motion. Those electrons collide with the molecules inside the chamber and ionize them, so that the ionized particles are accelerated towards the Ti cathode. The impact chemically binds the ionized molecules with Ti forming Ti compounds which are attracted and collected in the anode plates. Such an impact also sputters Ti onto the anode. Over time the pumping speed degrades because the anode gets covered by Ti and Ti compounds (TiO, TiO2, TiN, TiN2...) and the cathode's surface gradually breaks due to ion impacts.

In addition to the gases contained in the volume of the system ($\sim$ 1.6 m^3), the main gas load at the lower pressures is represented by the water vapor that is adsorbed on all the surfaces of the system. [Rutherford, 1997].

In time, Rb accumulation build up and a leakage current between electrodes appear. Such a current affects the current readout of the pump and the pressure appears higher than the actual pressure inside the chamber. We have observed this phenomenon comparing the readout of the pressure before and after a baking up procedure to remove the accumulated Rb. The procedure lasted 120 hours, over which the temperature of the ion pump was increased to a maximum value of 150° C and decrease it back to room temperature as advised by [GammaVacuum, 2006]. Because Rb deposition grows very fast we decided to monitor the pressure by monitoring the loading time of the MOT (see Section 5.5.1).

In order to create the pump's strong magnetic field the ion pump requires, two strong ferrite magnets are placed outside the vacuum part of the pump (see Figure 3). These magnets are enclosed in magnetic steel to concentrate the field inside where it reaches values of 1200 G. Outside the steel container the magnetic field is still very strong, $\sim$ 33 G measured with a Hall probe

(TE2010.405), which means the magnetic steel enclosure already attenuates the flux field by a factor of 36 (an approximate magnetic plot is shown in Appendix C). Apart from our specific magnetic requirements the strong field created by the ion pump magnets tend to limit the minimum temperature molasses can achieve and therefore a better magnetic isolation is desired. We designed a mu-metal shielding for the ion pump in order to reduce the such remaining field (see Figure 3).

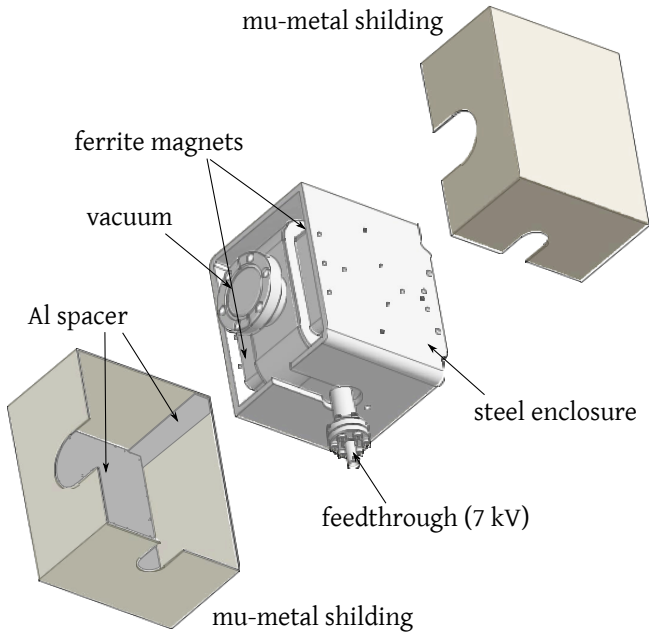

Figure 3: Mu-metal shielding for ion pump.

The attenuation factor of a magnetic shielding is defined as the ratio between the field strength inside B_{in} and the field strength outside B_{out}. This ratio depends on the magnetic and geometrical properties of the enclosure. For a cubic magnetic enclosure the attenuation factor is approximately:

$$A \equiv \frac{B_{in}}{B_{out}} = \frac{4}{5}\mu_r \frac{t}{l} \tag{48}$$

where μ_r is the relative permeability of the mu-metal, t the material thickness and l the side length of the box. Our shielding (The mushield company) is a two part box made of mu-metal high permeability comp-1 of 1.5 mm thickness. Its geometrical dimension are approximately $181 \times 144 \times 132$ mm (see Figure 3). According to the company high permeability comp-1 has a minimum relative permeability of 8×10^4 at 40 G with saturation point of 7500 G. The magnetic properties of the heat-treated mu-metal are very fragile under mechanical manipulation.

High permeability shieldings strictly require non-magnetic spacers to avoid direct contact with any strong magnetic source, this avoids saturation of the permeable material. We placed Al spacers between the shielding and the ion pump as shown in Figure 3.

For the sake of comparison we put the ferrite magnets inside the mu-metal shielding. The field strength outside the shielding was less than 3 G and therefore the attenuation factor is about 400, which is one order of magnitude better than the steel enclosure but lower than the estimated value of 530 according to Equation 48. This can be explained by the reduction of μ_r under strong magnetic fields, the value $\mu_r = 8000$ is considered for $B = 40$ G.

After placing the mu-metal shielding around the ion pump we measured the remaining magnetic field strength to be about maximum 4 G next to the ion pump and between 0.41 G and 0.56 G around the glass cell, which is close to the earth magnetic field 0.454 G given by the National Oceanic and Atmospheric Administration calculator .

https://www.ngdc.noaa.gov/geomag/magfield.shtml

Atom source

Rubidium is introduced into the vacuum chamber by sublimating solid rubidium from a dispenser. Two Rb dispensers were mounted on the electrical feedthrough (IFC8-C40, MDC) of the chamber, one with the natural abundance of ^{85}Rb and ^{87}Rb (Alvasource-3-Rb-C, Alvatec) and another one with purely ^{87}Rb (99.2%, Alvasource-3-Rb87-C, Alvatec) as shown in Figure 4. This technology has the solid alkali sealed in an Ar atmosphere pro-

tected by an In seal, and therefore the activation process comprises two steps, one to melt the In and release the Ar, and another one to actually release the alkali metal. This procedure is accomplished by passing a current through the dispensers to heat them for typically three minutes. The exact necessary current of about 3 A depends on the particular dispenser.

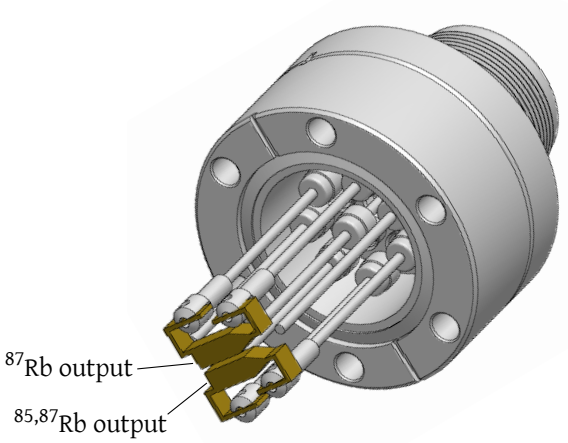

Figure 4: Dispensers mounted on a feedthrough serving as Rubidium source.

5.1.1 *Achieving ultra-high vacuum*

A primary pump connected behind the valve was used to lower the pressure from atmospheric to below 10^{-3} Torr, this pump is a turbo pump (Hicube Eco 80, TECNOVAC): pumping speed for N_2 35 L/s, which can reach an ultimate pressure of 10^{-7} Torr. When the pressure reached $\sim 10^{-6}$ Torr the ion pump was activated and the valve closed.

Water vapor in the surfaces of the chamber represents the majority of the gas load during pumpdown [Rutherford, 1997] and therefore heating up the system while pumping (baking) is rec-

ommended to accelerate the desorption of the water and reduce the pumpdown time.

A precleaning phase was carried out by baking the metallic parts of the chamber to 250 °C for twelve days. After reaching an ultimate pressure of $\sim 10^{-11}$ Torr, we opened the vacuum using nitrogen to fill the chamber and installed the glass cell and the window. A full cleaning was then carried out baking at a maximum temperature of 150 °C until reaching again the same ultimate pressure.

5.2 MAGNETIC FIELDS

Spatial confinement in MOTs requires relatively strong magnetic gradients, typically in the order of 10 G/cm. In order to create such gradients we use a pair of coils in anti-Helmholtz configuration, each one formed by 41 turns of 1.6 mm thick copper wire. Each coil has a resistance of about 0.16Ω. As shown in Figure 5 the MOT coils are mounted in plastic supports with the same dimensions of the glass cell. The radius of each coil is 55 mm and are separated by 75 mm. In this configuration we can create at the center of the chambers a gradient of 11.2 G/cm with 8.5 A.

the continuous use of higher currents is not recommended since the coils warm up and both the isolating layer and the epoxy glue that keeps fixed each layer of wires can melt deforming the coils and depositing residue on the chamber.

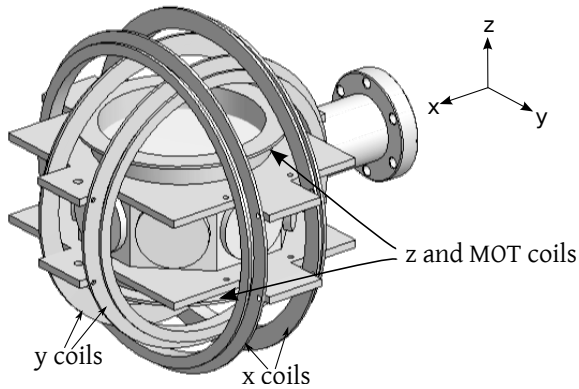

Figure 5: Coil support mounted around the glass cell. Z compensation coils are mounted on top of the MOT coils. X and Y coils are attached to the same mount (also see Appendix C).

In order to compensate high magnetic bias fields such as the earth's magnetic field we use three orthogonal pairs of coils in nearly Helmholtz configuration. Their dimensions are shown in Table 2.

coils	radius (mm)	coil separation (mm)	turns each
MOT	55	75	41
X	100	50	9
Y	85	50	9
Z	60	75	7

Table 2: Geometrical properties of compensating and MOT coils. See also the CAD drawings in Appendix C (courtesy of T. Vanderbruggen).

5.3 LASERS

We built up the experiment around a single master laser: a low noise, narrow linewidth laser that serves as a frequency reference for offset locking of the other lasers. One advantage is the compactness of the optical setup, since the master is the only laser being frequency stabilized by means of spectroscopic techniques. Another advantage is the possibility of reducing the frequency noise of the lasers when locked to the more stable master source.

Very narrow linewidths are difficult to measure, interferometric techniques require time delays equivalent to a laser being transmitted through hundreds of km of fiber, a distance comparable to the coherence length of the laser. This is not possible to implement directly at the resonance frequency of ^{87}Rb , 780 nm, due to the high losses of optical fibers at this wavelength. infrared (IR) frequencies, on the other hand, can be transmitted through optical fibers with hardly any losses which allows the possibility to build a self-heterodyne setup with hundreds of km of fiber delays for 1560 nm. Knowing the properties of this seed, one can use its second harmonic 780 nm, as the master laser of a ^{87}Rb experiment.

The developed IR fiber laser technology in telecommunications was an attractive solution for the desired reference laser. Fiber lasers are intrinsically single-longitudinal-mode with linewidths below 1 kHz, such lasers are long-term stable and frequency tuning is possible by applying tensile strain to the fiber. In particular Erbium doped fiber lasers operate in the 1530 nm to 1585 nm wavelength range.

5.3.1 *Master Laser*

5.3.1.1 *Frequency doubling*

Our master laser is the second harmonic of a 1560 nm Erbium doped fiber amplifier (EDFA) (*Koheras Adjustik and Boostik, NKT Photonics*) with maximum power of 3 W. We generate its second harmonic in a periodically poled Lithium Niobate (PPLN) nonlinear crystal (PPLN, *HCP Photonics*) of length $\ell = 50\,\text{mm}$ and grating period $\Lambda = 19.48\,\mu\text{m}$ for type-I phase matching. (See Figure 6). Aiming for optimal efficiency, we shaped our beam following the Boyd-Kleinman focusing condition for Gaussian pump beams. It states that the spot size that maximizes the conversion efficiency is such that the ratio of the crystal length to the confocal parameter is 2.84 [Boyd and Kleinman, 1968]. The confocal parameter is twice the Rayleigh range (z_R) of the focused Gaussian beam. The final configuration is a collimated Gaussian beam of 2.1 mm diameter focused with a 60 mm lens. We obtained a conversion efficiency of 1.9 %/W, generating a maximum power at 780 nm of 170 mW when pumping with the maximum power given by the EDFA.

5.3.1.2 *Linewidth measurement*

In order to estimate and monitor the frequency width of the EDFA we built a delayed self-heterodyne interferometer (DSHI) for IR (see Figure 7). The interferometer is formed by one first path which is a delay line of $\tau_d = 0.5\,\text{ms}$ in 100 km of single-mode fiber (Corning SMF-28). The second path is a path frequency shifted by 40 MHz in an acousto optic modulator (AOM)

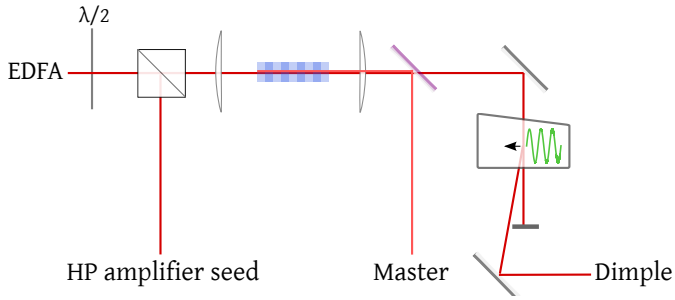

Figure 6: Doubling bench. EDFA 3 W at 1560 nm, 2.1 mm beam diameter pumping PPLN 50 mm long with 60 mm focal length lenses.

(Gooch & Housego, I-FS040-2S2J-3-GH53). Such an AOM is driven by the amplified signal of a clock generator with relative frequency stability of 10^{-12} (or equivalently, has a linewidth below 1 Hz). In free space both paths are combined and detected with an InGaAs photo diode (PD) with a transimpedance amplifier (TIA) (Thorlabs PDA10CF). The attenuation at 1550 nm in the fiber is 0.22 dB/km and therefore 100 mW of 1560 nm entering the delay line is enough to have a good signal on the PD.

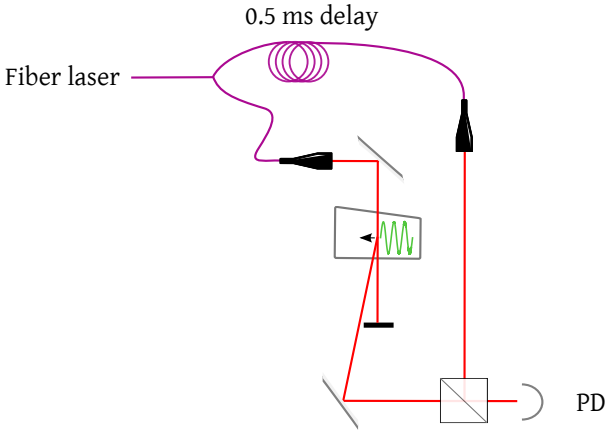

Figure 7: IR Self-Heterodyne interferometer bench for narrow linewidth measurements.

It has been found by a number of works that fiber lasers exhibit not only white frequency noise which is is due to quantum phase fluctuations and gives the characteristic Lorentzian lineshape to the laser spectrum, it also exhibits low-frequency noise substantially due to temperature fluctuations that induce noise in the seed beam. Those low-frequency fluctuations have been approximated by a low frequency cut-off [Horak and Loh, 2006] or $1/f-$noise [Mercer, 1991]. We will follow the analysis on the latest in this full section unless otherwise stated.

The authors have demonstrated that the total spectrum of a fiber laser is well approximated by the convolution of a Lorenzian function of width γ and a Gaussian function with standard deviation σ. Matematically, such a convolution is the so called Voigt function which can be written in terms of the real part of the Faddeeva function as:

$$V(z) = \frac{1}{\sqrt{2\pi}\sigma}\Re\{\exp\left(-z^2\right)\operatorname{erfc}(-iz)\}, \tag{49}$$

for the complex number $z = [\nu + i\gamma]/\sqrt{2}\sigma$. The full width at half maximum (FWHM) of this distribution can be related to γ and σ through:

$$\Delta V^{FWHM} \simeq 1.0692\gamma + \sqrt{0,8664\gamma^2 + 5.54\sigma^2} \tag{50}$$

The DSHI signal is acquired with a spectrum analyzer with resolution bandwidth of 30 Hz. Figure 8 shows the data and Voigt fit obtained with a nonlinear least squares procedure and using the code by [Abrarov and Quine, 2014] to estimate the Faddeeva function. The results of the fit are: $\Delta V^{FWHM} = 3.12 \pm 0.10$ kHz, and corresponding $\gamma_F = 453 \pm 20$ Hz, $\sigma_F = 1.10 \pm 0.03$ kHz. The inset in Figure 8 shows a Gaussian fit to the data with $\sigma = 1.03$ kHz which only fits well the top part as expected. The Voigt fitting is limited by the distinctiveness between a Gaussian and the $1/f$ contribution to the self-heterodyne lineshape.

With the obtained fit parameters to the DHSI signal we estimate the laser to have corresponding widths: $\gamma_{1560} = \gamma_F/2 =$

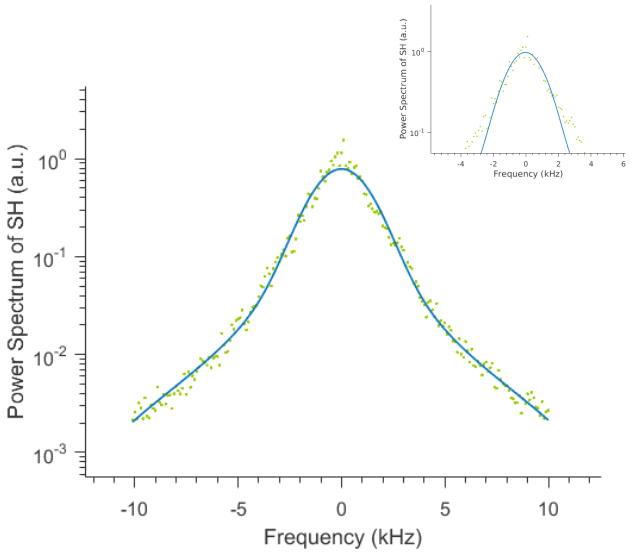

Figure 8: DSHI signal frequency shifted to center at 0 Hz (green dots) and Voigt profile fit (blue line) showing the linewidth measurement of the master laser at 1560 nm. Inset shows a Gaussian fit that accurately describes only the center part of the lineshape.

226 ± 10 Hz and $\sigma_{1560} = \sigma_F\sqrt{2}/2 = 784 \pm 20$ Hz, and FWHM of the Voigt profile: $\Delta V_{1560}^{FWHM} = 2.10 \pm 0.05$ kHz at $\tau_d = 0.5$ ms.

When a DHSI is used to measure the linewidth of a laser with only white noise, the resolution of the interferometer can be simply interpreted as $1/\tau_d$, which implies the delay line has to be much longer than the expected Lorentzian width. When low frequency noise is present the delay itself plays a role on the estimation of the $1/f$—noise width since long delays cause broadening of the signal. In this setup, $1/\tau_d = 2$ kHz, comparable to the measured full width of the laser, which might cause a slightly underestimation of the laser linewidth. Longer delays require recirculating delay lines like that demonstrated in [Dawson et al., 1992].

The linewidth of the second harmonic at 780 nm

The theory used in the previous analysis assumes the jitter (noise in time domain) is stationary such that $\langle \exp\{i\Delta\phi(t,\tau)\}\rangle = \exp\{-\langle\Delta\phi^2(\tau)\rangle/2\}$, and the mean square phase fluctuation can be written as:

$$\langle\Delta\phi^2(t)\rangle = \langle[\phi(t+\tau)-\phi(t)]^2\rangle \tag{51}$$

$$\simeq \frac{2}{\pi}\int \sin^2(\omega\tau/2)\left[S_0 + \frac{k}{|\omega|}\right]\frac{d\omega}{\omega^2} \tag{52}$$

where $S_0 = 2\gamma$ and $k \simeq 4\sigma^2$. In the second harmonic process the generated field is proportional to the square of the fundamental field, this means the phase of the second harmonic is $\phi_{SH}(t) = 2\phi(t)$ and therefore: $\langle\Delta\phi^2_{SH}(t)\rangle = 4\langle\Delta\phi^2(t)\rangle$. This factor can be understood as an increase in the width of the noise as: $S_{0,SH} = 4S_0$ and $k_{SH} = 4k$. This implies the Lorentzian width of the noise of the second harmonic is a factor of 4 the noise in the fundamental mode whereas the Gaussian is a factor of two larger:

$$\begin{aligned} \gamma_{780} &= 0.90 \pm 0.04\,\text{kHz} \\ \sigma_{780} &= 1.570 \pm 0.040\,\text{kHz} \\ \Delta V_{780}^{FWHM} &= 4.75 \pm 0.06\,\text{kHz}. \end{aligned} \tag{53}$$

5.3.1.3 *Modulation Transfer Spectroscopy for frequency stabilization*

We frequency lock our master laser with a closed-loop feedback based on modulation transfer spectroscopy (MTS). MTS relies on a four-wave mixing (FWM) process where a frequency modulated pump beam and an unmodulated probe interact via the nonlinear medium (vapor cell) to create new sidebands of the probe [Camy et al., 1982; Ducloy and Bloch, 1981, 1982]. Phase matching conditions require this new field to propagate in the same direction as the probe beam. When the probe and its sidebands are detected and properly demodulated, a dispersive signal suitable for frequency locking is obtained. This nonlinear pro-

cess is more efficient in closed transitions where there is no relaxation to non resonant states. We use it to stabilize the master laser to the closed transition $|5S_{1/2}, F = 2\rangle \rightarrow |5P_{3/2}, F' = 3\rangle$ (see Appendix A).

MTS has several advantages over typical saturated absorption spectroscopy. The major one is the lack of background offsets due to linear absorption. In addition, this technique is very robust under power and magnetic field fluctuations: less than 50 kHz of deviation from the absolute frequency are expected for power fluctuations of 50% or magnetic fields of up to 60 µT, as we demonstrated in [de Escobar et al., 2015]. It is important to mention that only frequency modulated (FM) signals provide dispersive-like shapes, a purely amplitude modulated (AM) saturating beam would have only in-phase sidebands losing the odd symmetry characterizing a dispersion-like signal. Special care has to be taken to reduce any residual amplitude modulation (RAM) coming from envelope responses of VCOs or AOMs and beam misalignments, as it induces zero crossing offsets on the lineshape and therefore frequency shifts.

The MTS setup is shown in Figure 9. Part of the master laser is split into two beams: a weak probe (0.46 mW) and a strong pump (1.5 mW). The pump is additionally modulated and frequency shifted by an AOM in cat-eye configuration driven by an FM signal. The beams are expanded to have waists of 4.5 mm, larger waist reduce misalignment induce RAM. Both beams counterpropagate in a Rb glass cell at room temperature having orthogonal linear polarizations. The probe is detected with a photodiode with a transimpedence amplifier after it traverses the cell.

The FM signal is generated by a VCO (Minicircuits ROS-80-7119) driven by a local oscillator (LO) DC offset, it oscillates at $f_c = 83.6\,\text{MHz}$ with sidebands at $f_m = 3.413\,\text{MHz}$ (see upper part of Figure 10). The pump beam passes the AOM twice before it enters the cell, at that point its frequency is $f_{pump} = f_p - 2f_c + nf_m$, where n indexes the corresponding sideband.

During the FWM process two components of the pump, $f_p - 2f_c + n_1 f_m$ and $f_p - 2f_c + n_2 f_m$, combine with the probe to generate new fields oscillating at $f_p \pm (n_1 - n_2)f_m$. These new fields, interfering with the probe are detected as amplitude modulation

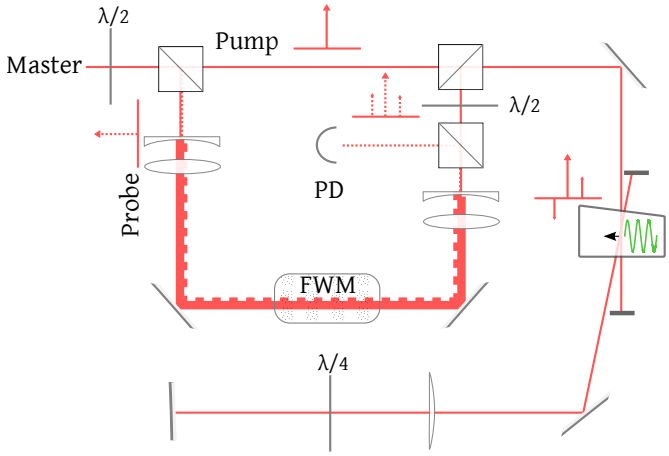

Figure 9: Optical setup for MTS. Dotted line and continuous line represent probe and pump beams respectively

at frequency $(n_1 - n_2)f_m$. This beat note is split into DC and RF components. The former is used to monitor light absorption while the second is demodulated by mixing it with an extra output of the LO. The demodulation phase can be chosen to observe the lineshape in absorption or dispersion. The dispersive signal is low-pass filtered at 100 kHz and fed as the error signal into a proportional-integral (PI) controller. The output signal is fed back on the piezo-electric transducer (PZT) tensing the fiber of the laser (see Figure 10).

A typical obtained MTS error signal is shown in Figure 11 with an absorption profile showing the transitions $|5S_{1/2}, F = 2\rangle \rightarrow |5P_{3/2}, F' = 1, 2, 3\rangle$ in ^{87}Rb and $|5S_{1/2}, F = 3\rangle \rightarrow |5P_{3/2}, F' = 2, 3, 4\rangle$ in ^{85}Rb. Notice that the signal is much stronger for the two closed transitions.

Considering the resonance condition of the two photons being absorbed:

$$\begin{aligned} f_0 &= f_p - 2f_c - f_0 v/c, \\ f_0 &= f_p + f_0 v/c, \end{aligned} \tag{54}$$

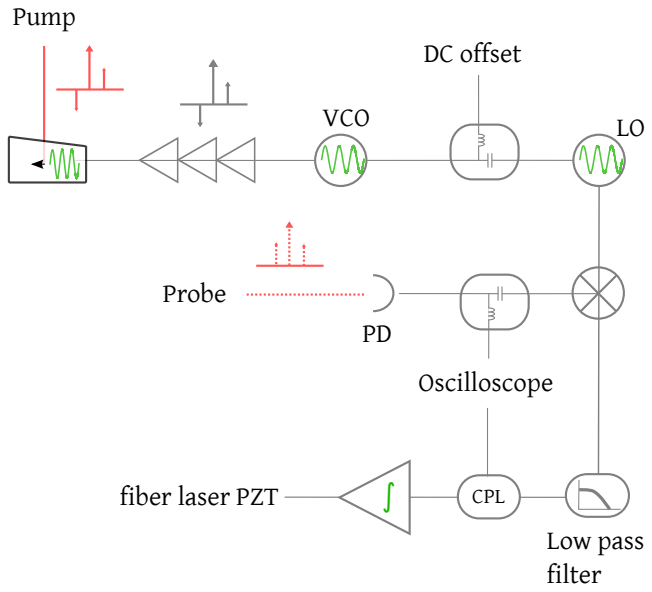

Figure 10: Closed-loop feedback for MTS. We use auxiliary CPLs to monitor our signals.

where v is the addressed atom velocity class, k the wave number of the fields and f_0 the absolute frequency of the transition, we find the resonance frequency : $f_p = f_0 + f_c$. For this reason we frequency lock the master laser 83.6 MHz above the $|5S_{1/2}, F = 2\rangle \rightarrow |5P_{3/2}, F' = 3\rangle$ transition.

5.3.2 *Cooler and repumper*

Extended cavity diode lasers (ECDL) have been the ubiquitous laser technology in atomic physics. This lasers have narrow linewidth, are widely tunable, and easy to frequency stabilize. These lasers are diode lasers with an additional frequency-selective element. In our case that role is played by a grating in front of the diode laser mounted in Littrow configuration. We have two ECDLs, one resonant with the cooling transition $|5S_{1/2}, F = 2\rangle \rightarrow |5P_{3/2}, F' = 3\rangle$ (TApro, Toptica) and another to repump atoms back into the cycling transition which is resonant with $|5S_{1/2}, F = 1\rangle \rightarrow |5P_{3/2}, F' = 2\rangle$ (DL pro design, Toptica). Both lasers have linewidths below

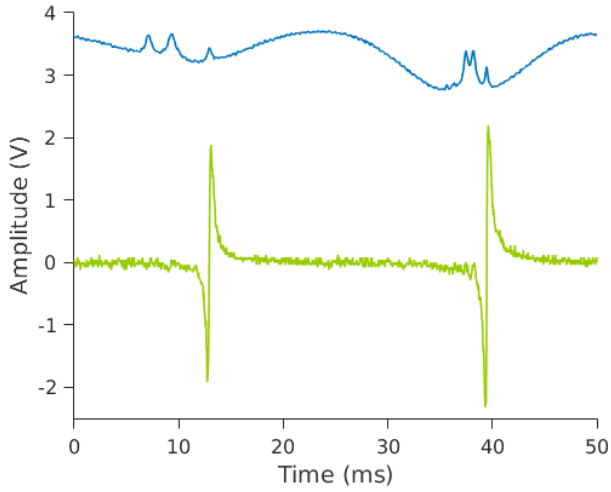

Figure 11: Blue line: saturated absorption profile for ^{87}Rb and ^{85}Rb D2 lines. Green line: error signal obtained from MTS.

500 kHz and maximum powers of 0.9 W and 70 mW in a clean Gaussian mode, respectively.

The bench for the MOT lasers is sketched in Figure 12. All inputs and outputs are fiber coupled. Both cooler and repumper are combined in a 30/70 beam splitter after passing an AOM to control their power. We use small mechanical shutters to block laser light (SHT934, Sunex) with open and close times of 8/6 ms driven with 200 mA. We were not able to use them at the nominal times of 2.8/1.8 ms since the stronger driving current needed to reach those times lead to their destruction.

After the cooling and repumping beams are combined the light is fiber coupled and sent to an optical assembly of power-splitting modules (fiber optical beamport cluster 1→6, Schäfter & Kirchhoff) where by adjusting five half-wave plates one can equalize the output power of its six fiber outputs. The first optical element in the cluster is a PBS, therefore we can adjust the ratio of cooler to repumper powers traversing the cluster by adjusting the last half-wave plate in the MOT bench. Before the five splitting modules a 99/1 BS and a PD are used to monitor the total input power in the cluster.

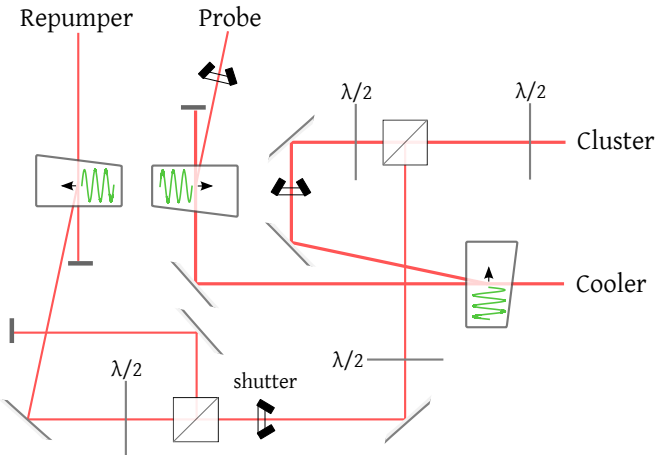

Figure 12: MOT light bench. Both cooler and repumper are combined after passing an AOM to control their power. By adjusting the half-wave plate at the output cluster we set the ratio of cooler power to repumper power since the input of cluster has a PBS. All inputs and outputs are fiber coupled.

The six outputs of the cluster are sent to six fiber collimators with a quarter waveplate integrated (60FC-Q780-4-M60-10, Schäfter+Kirchhoff), these six beams with circular polarization counterpropagate by pairs in three orthogonal spatial directions. The output diameter of these beams is about 1 cm. In two of these orthogonal directions we add secondary beam expanders to increase the diameter by a factor of two .

the original design contemplated 1 cm *beams for the MOT, a later requirement of higher number of atoms resulted in the expansion of such beams*

5.3.2.1 *Phase-locked loop for frequency stabilization.*

We stabilize our ECDL using an optical phase-locked loop. This locking technique keeps constant the rate at which the relative phase between two lasers, a master laser and a slave laser, changes. Such a rate is the beat frequency f_{beat} of the heterodyne signal from a fast photodiode where both beams combine. The first step in this loop is to compare f_{beat} with an external frequency reference f_{ref} and generate a current proportional to the difference between them. This signal is to be minimized at each loop by giving proper feedback to the slave laser. This technique is very robust in frequency and mainly limited by the photodiode's speed.

It can be used to lock lasers with frequency offsets of up to tens of GHz [Appel et al., 2009]. Another powerful capability of this technique is the possibility of transferring the frequency stability of a stable master laser to a less stable slave laser [Santarelli et al., 1994]. For those reasons we lock the MOT lasers to our more stable master laser.

this light is taken from the extra output the cooler laser has. It comes from the ECDL seeding the TA

The setup to frequency lock the cooler laser is shown in Figure 13. From *master* output in the doubling bench (Figure 6) we take 1 mW of master laser light to fiber combine it with 5 mW of cooling light and detect in a PIN receiver (PT10GC, Bookham) 10 Gb/s speed. The beatnote (179.8 MHz) is split with a bias tee, the DC component is sent to an oscilloscope to monitor the amplitude of the signal and the RF component to a coupler taking a small fraction of light to monitor with the spectrum analyzer, the rest feeds a digital phase-frequency-discriminator chip (ADF4110, Analog Devices). In the original design, an external voltage controlled oscillator (VCO) performed the external frequency reference, today an atom clock does. By interfacing the chip with a micro-controller board (SDP, Analog Devices) we can program different counters to divide f_{ref} and f_{beat} before they enter the phase frequency detector, this gives us the possibility to use frequency references below the microwave range even for locking lasers several GHz apart in frequency. A charge pump converts the frequency difference into a proportional current, which is sent to an external loop filter and to the PI. In the PI the signal is amplified and integrated twice. The output of the first integrator actuates on the laser current (FET, 20 MHz bandwidth) and the one of the second on the PZT (kHz bandwidth), this last part dominates at DC.

To frequency shift the laser we reprogram the PLL. To reach faster the requested frequency we add a feed forward voltage directly acting on the PZT. This is particularly important for phases of the experiment requiring large shifts in short times like during molasses and dipole trap loading (see Section 5.5.2).

Using this locking technique has several advantages: there is no need to have more than one spectroscopy setup per wavelength in the laboratory, it is robust against amplitude fluctuations of the beat signal, exhibits high stability and its versatil-

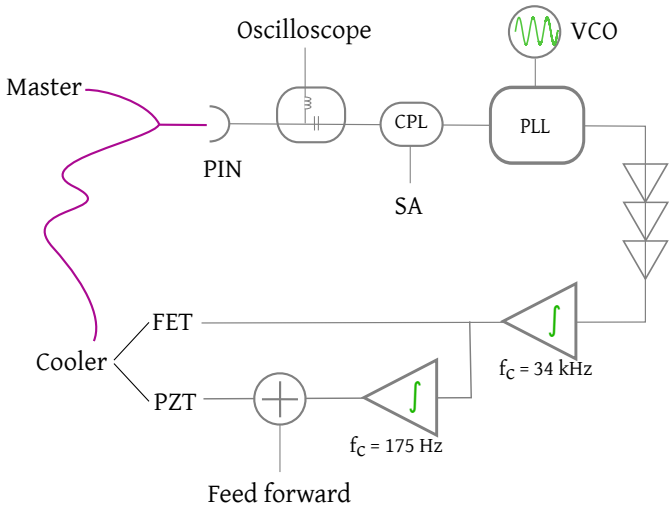

Figure 13: Heterodyne optical looking of cooler laser. Purple lines represent optical signals in fibers and gray lines electronic signals. The PLL is formed by a phase frequency detector, a charge pump, two programmable reference dividers and a external loop filter and frequency reference.

ity allows us to transfer the master's laser frequency stability to other lasers, even those offset by GHz. We use a completely analogous design for locking the repump laser, with the difference that the digital phase-frequency-discriminator chip is faster (ADF4102, Analog Devices) since the beat note between the master and the repumper oscillates at 6.564 GHz.

5.3.3 *Dipole laser*

The spatially dependent AC Stark shift is exploited to create a conservative potential capable of trapping sub-mK atoms (see also Chapter 2). In the electric dipole approximation we can describe such a potential as $U_{dipolar}(\mathbf{r}) = -\mathbf{d} \cdot \mathbf{E}$ where $\mathbf{d}$ is the dipole moment induced on the atoms and $\mathbf{E}$ the electric field of the light.

In terms of the complex polarizability this potential can be written in the form [Grimm et al., 2000]:

$$U_{dipolar}(\mathbf{r}) = -\frac{1}{2\epsilon_0 c}\mathrm{Re}\{\alpha\}I(\mathbf{r}), \tag{55}$$

where α is the polarizability (state dependent) and $I(\mathbf{r})$ the spatially dependent intensity of the light.

5.3.3.1 *Trap Geometry*

For reasons that will become clear in Chapter 6 we designed an ODT formed by three Gaussian beams: the first beam propagates along $\mathbf{x}$, has a waist w_1 and power P_1. The second beam propagates along $\mathbf{y}$ having a waist w_2 and power P_2, while the third propagates along $\mathbf{x}_R = R(\phi_o)\mathbf{x} = \cos(\phi_o)\mathbf{x} + \sin(\phi_o)\mathbf{y}$, where ϕ_o is about 6°.

The total intensity is then given by:

$$\begin{aligned} I(\mathbf{r}) = &\frac{2P_1}{\pi w(w_1,x)^2}\exp[-2(y^2+z^2)/w(w_1,x)^2] + \\ &\frac{2P_2}{\pi w(w_2,y)^2}\exp[-2(x^2+z^2)/w(w_2,y)^2] + \\ &\frac{2P_3}{\pi w(w_3,x_R)^2}\exp[-2(y_R^2+z^2)/w(w_3,x_R)^2], \end{aligned} \tag{56}$$

where $w(w_m,n) = w_m\sqrt{1+n^2/(\pi w_m^2/\lambda)^2}$ for $m = 1,2,3$ and $n = x,y,x_R$ and $\lambda = 1560\,\mathrm{nm}$. The rotated direction $y_R = -\sin(\phi_o)\mathbf{x} + \cos(\phi_o)\mathbf{y}$ can be written in terms of the non-rotated coordinated applying the rotation matrix $R(\phi_o)$.

Using the expression Equation 56 we write the potential experienced by the atoms, which is the sum of the dipolar potential and gravitational attraction:

$$U(\mathbf{r}) = -U_0 I(\mathbf{r}) + mgz, \tag{57}$$

with $U_0 = \mathrm{Re}\{\alpha\}/(\pi\epsilon_0 c)$ being the potential depth identified as the light shift of the ground state at maximum intensity.

Typically atoms occupy the bottom of the potential since their thermal energy is about ten times lower than the potential depth. In this cases it is useful to expand the potential Equation 57 in its Taylor series around the minimum $\mathbf{r}_o$:

$$U(\mathbf{r}) \simeq U(\mathbf{r}_o) + D_U(\mathbf{r}_o)(\mathbf{r}-\mathbf{r}_o) + \frac{1}{2}(\mathbf{r}-\mathbf{r}_o)^T H_U(\mathbf{r}_o)(\mathbf{r}-\mathbf{r}_o) \quad (58)$$

$U(\mathbf{r})$ is continuous as well as its second partial derivatives. In this expression the second term containing the first derivative at the minimum $\mathbf{r}_o$, $D_U(\mathbf{r}_o)$ vanishes. The third contains the Hessian matrix H_U evaluated at the minimum. This expansion represents the harmonic approximation to the potential.

Because H_U is symmetric and has real entries, there exist an orthonormal basis $\mathbf{e} = \{\mathbf{e_1}, \mathbf{e_2}, \mathbf{e_3}\}$ formed by the eigenvectors of H_U, as stated by the spectral theorem [Hawkins, 1975]. H_U has a diagonal representation in the basis $\mathbf{e}$, here denoted by $H_U|_{\mathbf{e}}$. The corresponding eigenvalues are related to the oscillation frequencies of the harmonic potential through:

$$H_U|_{\mathbf{e}} = \sum_{i=1}^{3} M\omega_i^2 \mathbf{e_i} \quad (59)$$

where M is the mass of the atoms.

In order to estimate the expected frequencies following Equation 59 as function of the optical powers and waist we numerically find the minimum of Equation 57 and calculate the Hessian matrix at that point. Figure 14 shows the potential at full power of the three traps combined.

5.3.3.2 *Technology*

In order to create a far off resonance dipole trap we exploit one the most important technologies for long-range optical fiber communications: an Erbium-doped fiber amplifier (EDFA) which can amplify 100 mW of light in the 1.5 µm wavelength region to a maximum power of about 15 W (CEFACBOHPPM42-NL1-OM1-B301-FA-FA-3m, Keopsys). This type of amplifier contains a single mode fiber doped with Erbium ions (Er^{3+}) which is pumped

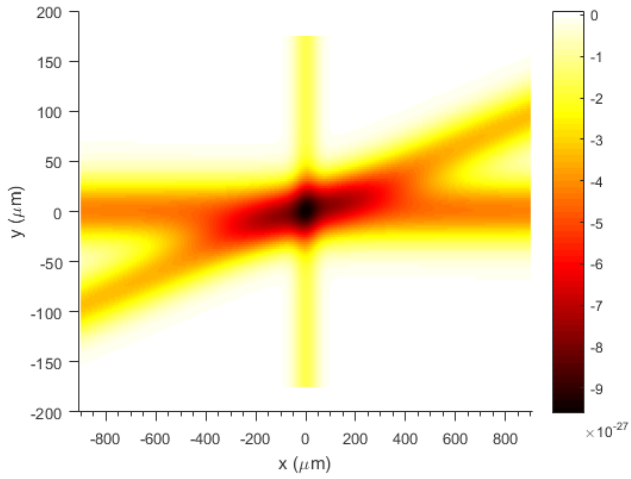

Figure 14: Potential (J) in the xy-plane induced by the dipole trap formed by the three beams: ODT1,2,3 at full power. From this perspective we can appreciate the large volume created by ODT1 and 3, and the small dimple-like confinement induced by ODT2.

with a laser diode that excites the ions to a high energy level, in this state the ion decay via multi-phonon transition to its first excited state from which light in the 1.5 µm wavelength can be amplified by stimulated emission. The output of the amplified optical field is inherently single mode in space and narrow linewidth.

5.3.3.3 *Power stabilization*

An all-optical evaporation process requires power control of the dipole beams over a range of up to30 dB. For this reason we implemented a noise eater with controllable setpoint (see Figure 15) where the in-loop PD is a large dynamic range logarithmic chip (AD8304, Analog Devices) with a transimpedance amplifier.

A fraction of optical power is split from the laser and sent to the PD. The generated voltage enters a PI feedback loop where a variable gain amplifier (VGA) outputs an RF signal with the adjusted amplitude. This RF is fed to an AOM in the optical path of the laser. The bandwidth of the feedback loop is 20 kHz.

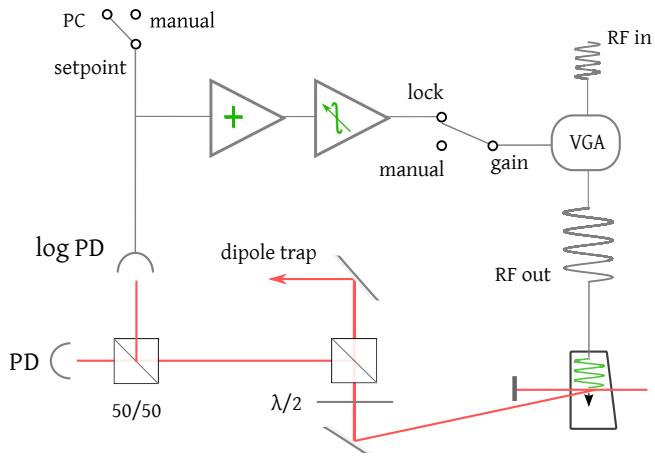

Figure 15: Power lock scheme with in and out of loop PD to control the dipole trap power and reduce its optical noise below 20 kHz.

Many different technical noise sources could in principle reduce the noise measured in-loop compared to an out-of-loop, such as photodiode internal low-frequency noise, resistor Johnson noise, beam pointing in combination with spatial inhomogeneous photodiodes, dust particles passing the beam, temperature fluctuations, photodiode bias voltage fluctuations, scattered light, electronic grounding noise, or polarization fluctuations. For this reason it is important to use an out-of-loop PD to monitor the power of the beam which contains the true noise of the beam.

Because the scattering rate of the atoms in a dipole trap scales with the inverse of the detuning squared, large detunings from resonance are used in dipole traps to reduce recoil heating rates [Miller et al., 1993] and excited-state trap loss collisions [Sesko et al., 1989]. Nevertheless laser intensity fluctuations and beam-pointing fluctuations may also play an important role in determining the minimum heating rates that can be obtained [Savard et al., 1997]. For this reason we characterize the intensity noise of our dipole laser in terms of its power spectrum to estimate the average energy given to the atomic system undergoing parametric excitation caused by light fluctuations. We recorded the power with an out of loop photodiode for different setpoints. From the

power spectral density of such signals we find the associated heating rate as described in [Savard et al., 1997]. Such a heating rate is negligible in the relevant spectrum (up to 2 kHz), compared to the loss rate caused by background collisions (typically 1/12 s and more than 1/20 s with low background pressure).

5.3.3.4 *Optical setup*

The optical bench of the dipole trap is shown in figure Figure 16. ODT1 is formed as follows. The output fiber of the first laser is connected to a fiber collimator (PAF-X-7-C, Thorlabs) that shapes the laser into a gaussian beam of waist 0.7 mm. The collimated beam (adjusted to have the minimum divergence angle, in this case 1.4 mrad) traverses an acousto-optic frequency shifter (I-FS040-2S2J-3-GH53, Gooch & Housego), that up shifts more than 90% of the total power. The remaining zero order is dumped in a high power beam trap. The up-shifted beam traverses a PBS where is combined with a 1529 nm beam (see Section 5.3.4), the reflected component, which has vertical polarization, is expanded by a 3X Galilean telescope and focused with a singlet (LA1708-C, Thorlabs). The last lens is mounted on a linear translational stage (M-SDS40, Newport).

The optics were chosen to have a beam waist $w_1 = 45\,\mu m$ at the focal point, this value was corroborated by measuring the beam waist using a beam profiler (BP209-IR/M, Thorlabs) obtaining: $D4\sigma_x = 88\,\mu m$ and $D4\sigma_y = 97\,\mu m$. $D4\sigma$ is the ISO international standard definition for beam width, for a perfect Gaussian beam $D4\sigma \equiv 2w$.

The ODT2 comes from a second amplifier with maximum power of 14 W. The fiber is coupled to a fiber collimator (PAF-X-7-C, Thorlabs) and down shifted by an AOM (I-FS040-2S2J-3-GH53, Gooch & Housego) by 40 MHz. The beam has the minimum divergence given by the collimator (1.4 mrad) and no extra telescope is present. The beam is then focused into the atoms with a 150 mm lens mounted on a translation stage. This beam has to traverse not only the glass cell but also a dichroic mirror we use to separate the collinear auxiliary imaging beam (see Fig-

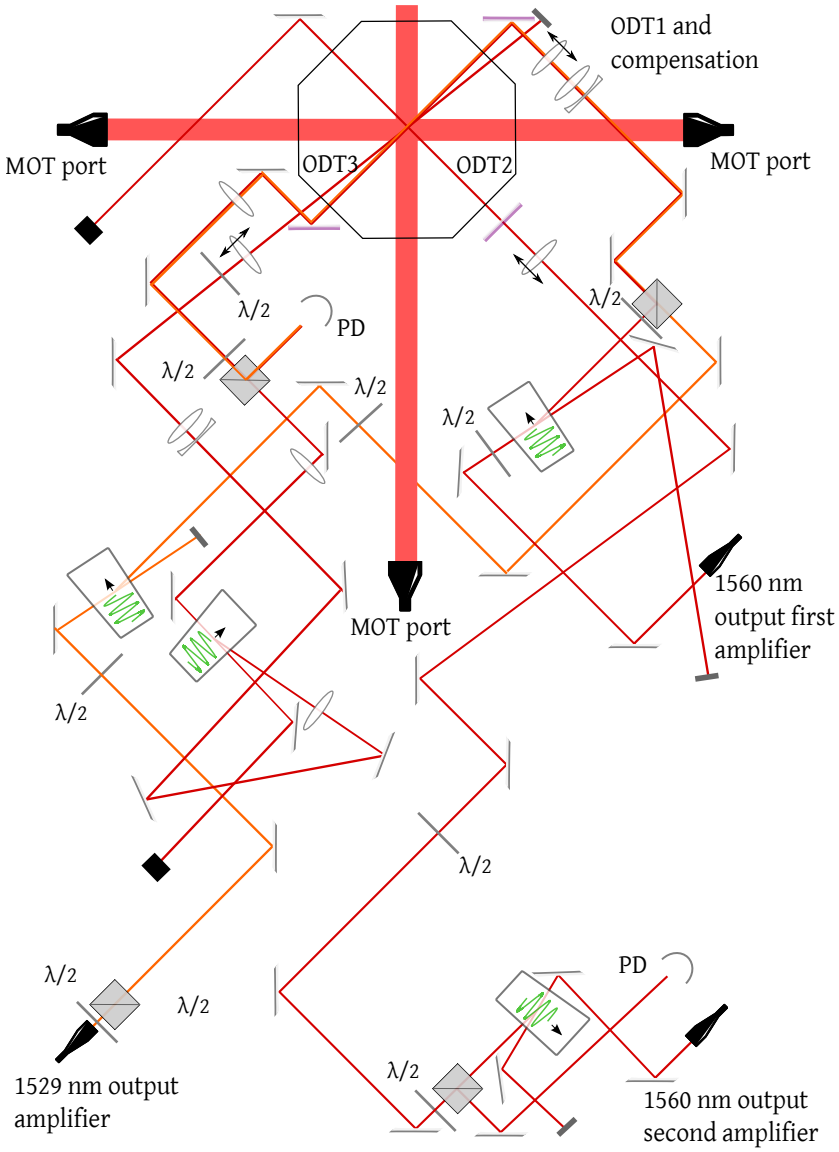

Figure 16: Optical layout of the dipole bench: Dark red ■ represents the ODT beams at 1560 nm, orange ■ the compensating beams at 1529 nm and soft red ■ the beams at 780 nm.

ure 22). The waists measured at high power are $D4\sigma_x = 129\,\mu m$ and $D4\sigma_y = 125\,\mu m$.

The ODT3 is a recycled beam from ODT1 with perpendicular polarization and 40 MHz frequency difference. To form it ODT1 is re-collimated by a 200 mm lens (LA1708-C, Thorlabs) at the output of the chamber. The beam, which is about 2 mm in waist is focused (LA1484-C, Thorlabs) into an AOM for the beam to fit into the active area. The AOM up-shifts the beam which is re-collimated back by a lens (LA1433-C, Thorlabs) which together with the previous one form a Keplerian telescope 0.5X. Before entering the chamber the beam is expanded by a 2X telescope and focused into the atoms by a 200 mm lens, to get a final waist at full power of $D4\sigma_x = 120\,\mu m$ and $D4\sigma_y = 140\,\mu m$.

The three beams are frequency shifted from one another by tens of MHz so any spatial interference between them effectively averages to zero from the atoms' perspective, since the atoms follow dynamics below a few kHz.

5.3.4 *1529 nm laser*

In the ^{87}Rb structure shown in Appendix A we can appreciate the existence of two excited transitions from $|5P_{3/2}\rangle \rightarrow |4D_{3/2,5/2}\rangle$, at around 1529 nm. It has been proposed to use this wavelength as part of a guide to continuously extract polarized atoms from a MOT [Vanderbruggen and Mitchell, 2013], and to study differential light-shifts that, in our particular experiment, play an important role in the loading process of the dipole trap.

Such wavelengths belong to the extreme of the telecommunication C-band at the opposite end of the 1560 nm, for which we could exploit techniques developed to build frequency references at 1560 nm and apply them to our 1529 nm. We have implemented a non-degenerate MTS setup completely analogous to Section 5.3.1.3 to stabilize the laser at the transition $|5P_{3/2}, F' = 3\rangle \rightarrow |4D_{5/2}, F'' = 4\rangle$. In this experiment the probe beam doesn't come from the same source but from the 1529 nm laser, this beam acquires the sidebands from the 780 nm modulated pump in the four-wave mixing process (see Figure 17). The modulated probe is detected and demodulated with the same signal the pump beam is modulated with. Such error signal is fed to a PI that

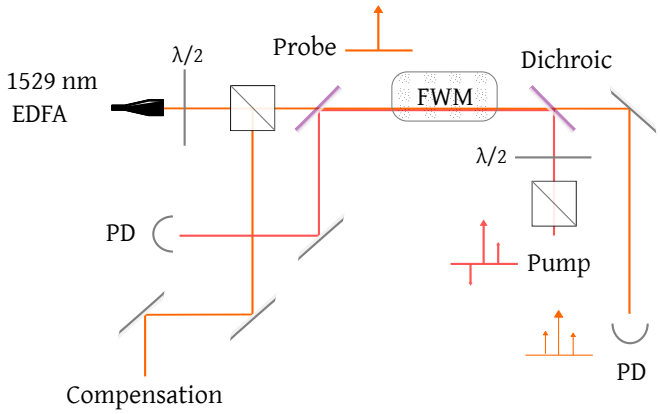

Figure 17: Bench for non-degenerate MTS using 1529 nm light.

feeds back the 1529 nm fiber laser. With this technique we demonstrated a short term Allan deviation of $\sigma(\tau) = 3.3 \times 10^{-12}\sqrt{\tau/s}$ and concluded that achieving an absolute accuracy of 1 kHz is realistic if standard stabilization techniques on the power, magnetic field, RAM and vacuum pressure are implemented [de Escobar et al., 2015].

Our light source is similar to that one for the 1560 nm laser: the seed is a fiber laser with maximum output power of 30 mW(AdjustiK, NKT) amplified by an EDFA (CEFA-C-PB-LPB201, Keopsys) with maximum output power of 32 dBm.

Hints

How do we align the position of the ODTs? First we adjust with the center of the chamber using irises (small aperture mask) and beam walk the beams. The irises were specially fabricated to mount on the chamber windows. Once the beams go through the center of the chamber we use the cameras to monitor in real time the ODTs position on the MOT. We can see the effect of the trap on the atoms because it induces a large differential light-shift that brings the atoms out of resonance from the MOT beams. This is observed as an "empty" region in the MOT wherever the

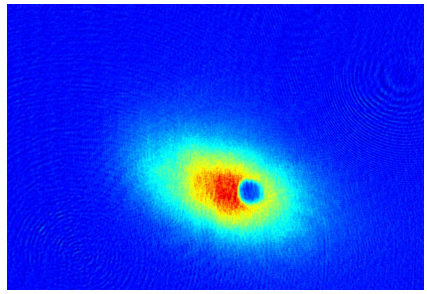

Figure 18: Absorption image of the MOT with a "hole" at the ODT2 position. This feature corresponds to a region with atoms out of resonance due to the induced differential lightshift. View along propagation axis of ODT2.

dipole is present (analogous to Figure 18). One can also use the copropagating 1529 nm beam to get a better signal. For the fine adjustment of the waist position, we load the ODT and hold them for several hundreds of ms. The atoms move to the focusing point and settle there, therefore by moving the translation stages the focusing lenses are mounted on, one can position the atoms distribution to the center of the MOT region (zero field crossing).

5.4 IMAGING

We use two standard techniques to characterize the atomic ensemble: fluorescence and absorption imaging. Both reveal the atom density distribution from which the number of atoms can be estimated, as well as their temperature. These are destructive techniques, with the first one being based on the detection of scattered resonant light in a long exposed single image, while the second one records the transmission of resonant light after part of the probing beam is absorbed.

There are different sources like [Reinaudi, 2013] where extensive descriptions of both imaging techniques are available. Since we mainly use absorption imaging in the saturating regime, only the implementation of this technique is detailed in this work.

5.4.1 *Absorption imaging in the saturating regime*

Absorption imaging is a standard technique in cold-atom experiments and a fundamental imaging technique in many branches of science. It maps the object of interest, in our case the atom distribution, on the flux of a resonant probe beam. By comparing this mapping with the original illuminating field we can extract information about the column density of the atoms.

It is implemented in the following way: a set of three images is taken, I_a which represents an image of the atoms illuminating with a probe light, I_p which is an image of only the probe light and I_b which is a background image where no atoms nor probe light is present. The images are projective representations of a 3D space and we have obviated the dependence in two spatial variables. In the low saturation regime the transmission of the light through the ensemble is well described by Beer's law: $I_f = I_i \exp\{-OD\}$, where $I_f = I_a - I_b$, $I_i = I_p - I_b$, and $OD = -n(x,y)\sigma_0(\gamma, \hat{\mathbf{e}}, I, ...)$, is the optical depth of the atoms. The column density distribution of the atomic ensemble $n(x,y)$, can be inferred from previous equation provided the scattering cross section σ_0 is known.

An example of typical images from an absorption imaging sequence are presented in Figure 19, where the eradication of inhomogeneities caused by undesirable scatter and interference patterns become evident in image OD.

In order to estimate the number of atoms we take the OD signal, which contains information about the column density and integrate it to get a 1D signal to which we fit a Gaussian distribution $A_F \exp\{-(x-x_0)^2/2\sigma_F^2\}$:

Assuming a thermal distribution described by Maxwell-Boltzmann distribution.

$$N = \sqrt{2\pi}\sigma_F A_F d_{px}^2/\sigma_0, \tag{60}$$

with d_{px} being the pixel size (m) (see Table 3). σ_0 = is the resonant cross section at the probing frequency and correspondent polarization. We probe the atoms with linearly polarized light resonant with the $|F = 2\rangle \rightarrow |F' = 3\rangle$ transition.

This approximation is only valid for low OD 's (well below 1), denser clouds like a condensate would absorb most of the pho-

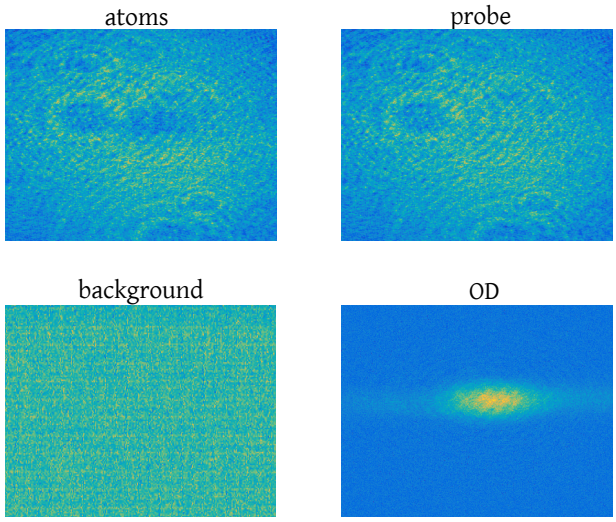

Figure 19: Typical example of raw images and OD for absorption imaging. Images are 1392×1040 pixels each. Atoms, probe and background images display the photon counts on each pixel. The OD image is dimensionless.

tons in their center, surpassing the dynamic range of the technique. To overcome this limitation we may use higher intensities for which the analysis has to be modified.

In the strong saturating regime, where the intensity of the probing light surpasses the saturating intensity associated to the transition used for imaging (I_0^{sat}), Beer's law is modified to the form:

$$OD(\alpha^*) = -\alpha^* \ln\left(\frac{I_f}{I_i}\right) + \frac{I_i - I_f}{I_0^{sat}} \tag{61}$$

where $I_{eff}^{sat} = \alpha^* I_0^{sat}$, this means that α^* is an adjusted absorption coefficient that takes into account polarization corrections, excited state structure and ground state population occupation of different Zeeman states, that could modify the effective cross section [Reinaudi et al., 2007]. In practice, this parameter is found experimentally in the following way. We start assuming $I_0^{sat} = 3.577\,13 \pm 0.000\,74\,mW/cm^2$ [Steck, 2001] which is such for the

$|F = 2\rangle \rightarrow |F' = 3\rangle$ transition and isotropic light polarization. This chosen value is not really important since the measured value of α^* will correct to match the effective saturation intensity which depends also on the light polarization. We then take absorption images at different light intensities and compute $OD(\alpha)$ for different values of α in the range $[0.25, 2.0]$. We then have OD values that vary for different light intensities and different chosen α's. α^* is then chosen to be the value of α that minimizes the variations on the OD for different light intensities, such variations are represented by $\text{std}(OD(\alpha))$.

The probe polarization is linear at the entrance of the coated chamber but it enters at a large angle, that may cause changes in the polarization.

As shown in Figure 20 the calibration for our optical system with total magnification of 2 is $\alpha^* = 1$ whereas for that one with total magnification of 5 is $\alpha^* = 1.25$.

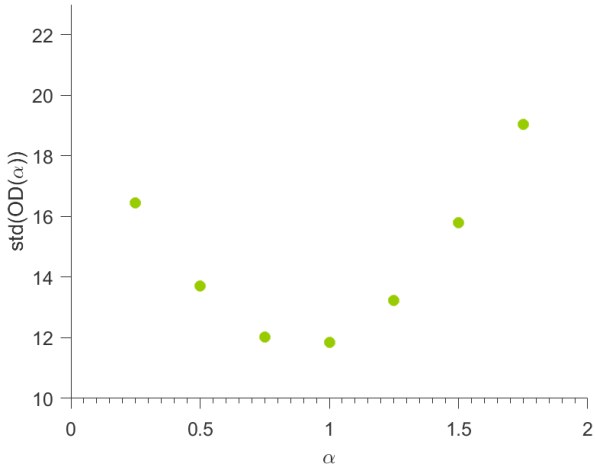

Figure 20: Variations on the computed OD for different light intensities as a function of α. The correspondent α^* is 1. This calibration correspond to the imaging configuration with total magnification 2.

Estimating the number of atoms now becomes the same procedure now with OD given by Equation 61 with the cross section $\sigma_0 = 1.356\,456\,704\,270 \pm 0.000\,000\,000\,031 \times 10^{-9}\,\text{cm}^2$ [Steck, 2001] and the respective calibrated α^*.

5.4.2 *Optics: magnification and resolution*

The most basic system is formed by an objective and a detector array like a CCD. Ideally this system has a limited resolution given by the Rayleigh criterion:

$$r_{res} = \frac{1.22\lambda}{2NA} \tag{62}$$

where λ is the wavelength of the light to be collected (the resonant probe beam which is 780 nm), and therefore it is desirable to use optics with the highest possible numerical aperture (NA) in order to have the best spatial resolution of the object.

This can be accomplished by using a large lens as close as possible to the chamber. Our chosen objective lens is a telecentric lens (Xenoplan 1:2 0.14, Schneider) with working distance of 195 ± 12 mm and NA of 0.14. This defines a limiting resolution of 3.4µm. Telecentric lenses are designed to minimize distortion and perspective errors, what makes them key elements in high accuracy imaging applications. The main advantage, nevertheless is the fact that they have constant magnification for different object positions: the Xenoplan can be focused within 6mm and the magnification stays constant at 0.5, which is particularly useful since we perform imaging in a large range of time of flights where the distance the atoms drop to can be in the mm scale like when revealing the double structure of the condensate.

The next step is dealing with the digitalization of this analogue signal. According to Nyquist criterion a sampling interval equal to twice the highest specimen spatial frequency is required to accurately preserve the spatial resolution in the resulting digital image. This is, at least two pixels are needed to resolve a feature [Department, 2014]. In commercial cameras a useful number of interest is the modulation transfer function (MTF) usually expressed in line-pairs per mm, the camera resolution is then the inverse of this number.

Our CCD camera has 14bit with 1392×1040 pixels, each one $6.45\,\mu m \times 6.45\,\mu m$ for a total sensor size of $9\,mm \times 6\,mm$ (Pix-

elfly USB, PCO). Its MTF is 77.5lp/mm and therefore we can calculate the object resolution if we know the magnification of the objective used:

$$\mathrm{ObjectResolution} = \frac{\mathrm{CameraResolution}}{\mathrm{Magnification}} = \frac{1}{\mathrm{MTF} \times \mathrm{Magnification}} \tag{63}$$

From this equation we can see that high MTF and magnifications are desired when converting into a discretized space. In the case of our camera when imaging with the telecentric lens, this limit is $1/(77.5 * 0.5)\mathrm{mm} = 26.7\mu\mathrm{m}$ which is worse than the Rayleigh limited resolution defined by the optical path.

For imaging a MOT of typical sizes of a few mm this imaging works perfectly, nevertheless when smaller atoms distributions are of interest, a more complex imaging system with higher magnification is required in order to improve the digital resolution given by Equation 63.

To do so, we add extra optical elements to the telecentric plus camera system: the image taken by the telecentric is collected by a microscope objective (N10X-PF,N4X-PF,Nikon) which creates the image of the atoms at infinity (see Figure 21). Both are designed to work with an infinity-corrected tube lens of 200 mm (ITL200, Thorlabs) which refocus the rays and form an image on the CCD. The combination lens tube plus 10X objective, has a $NA = 0.3$ whereas the combined lens tube plus 4X objective has $NA = 0.13$.

Both microscopes provide high magnifications, that in combination to the telecentric lens are 2X and 5X when using N4X-PF and N10X-PF respectively. These magnifications improve the digital resolution to 6.5 µm and 2.5 µm and therefore our best imaging setup, which uses the N10X-PF objective, is a Rayleigh limited system with resolution of 3.4 µm and 5X total magnification.

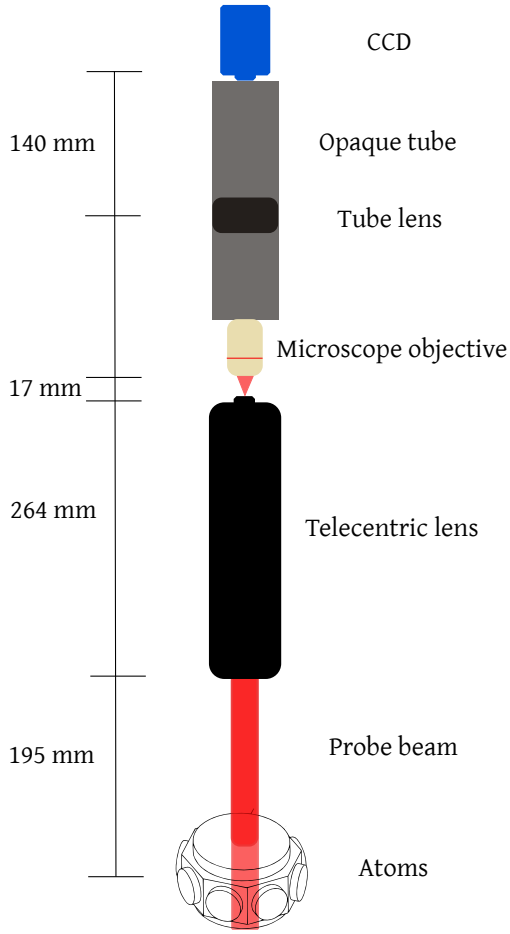

Figure 21: Main imaging system sketch. After telecentric lens the camera can be directly positioned to have a total magnification of 0.5, when the full system is used the magnification is modified depending on the used objective.

5.4.3 *Timing and exposure*

The Pixelfly camera has a double shutter functionality that allows the sensor to be exposed two times before completing the readout of the first image. In this way, the camera doesn't represent a limitation to the time elapsed between the atom and the probe images. A long time delay between the two images

Magnification	Resolution	Scale conversion	Transmission (780 nm)	α^*
0.5X	26.7 µm	12.9 µm/px	0.8730	
2X	6.5 µm	3.2 µm/px	0.7333	1
5X	3.4 µm	1.3 µm/px	0.6722	1.25

Table 3: Main parameters of the different imaging configurations.

(~ 100 ms) allow noise sources like polarization fluctuations to degrade the quality of the absorption imaging technique.

We take the atom image and the probe image within 500 µs. This time is used to depump the atoms to a dark state.

5.4.4 *Angle of view calibration*

As sketched in Figure 22 the probing beam traverses the chamber at an angle of around 45°. In order to find the exact position of the view we track the free falling atoms in time. The displacement in the image is the projected displacement along gravity. Plotting the displacement vs $gt^2/2$ we find the slope corresponding to a view with elevation = 48.9°. The azimuth is $\pi/4$.

5.4.5 *Auxiliary camera*

In addition to the main imaging system described above we set an auxiliary basic imaging system with view along ODT2. It is composed by a camera (BFLY-PGE-03S2M-CS, PointGrey) and a fixed focal length imaging lens (TECHSPEC, Edmund Optics).

This view is specially useful for crossing the dipoles in the vertical direction. ODT2 appears integrated and can easily be moved towards ODT1 in an unmistakable way, in contrast with the principal view which is a projected image of the vertical and plane directions. The probe beam used in this configuration is split from ODT2 with a dichroic mirror (DMLP1180L, Thorlabs). See Figure 22.

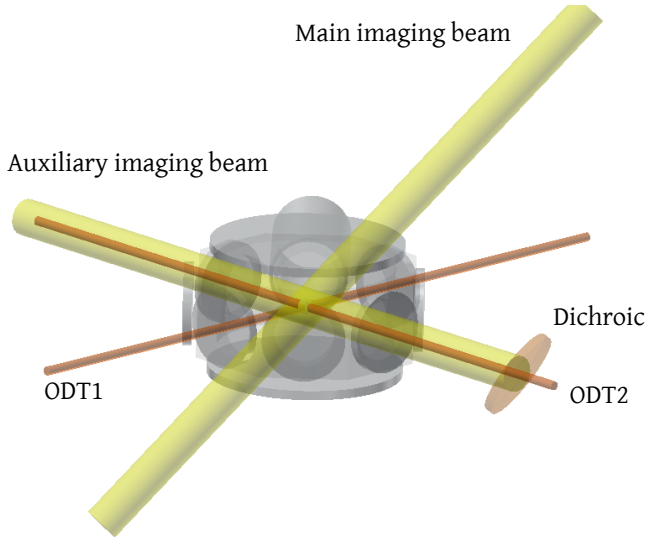

Figure 22: Sketch of the two imaging views that we use in the optimization and characterization of our trapped atoms.

5.4.6 *Estimating the atom temperature*

In order to determine the temperature (T) of the atoms we use the relation of the free expansion of a Gaussian distribution with T:

$$\sigma_x(t_{tof})^2 = \sigma_x(0)^2 + \frac{k_B T}{M} t_{tof}^2, \tag{64}$$

where $\sigma_x(t_{tof})$ is the width of the Gaussian distribution at the time t_{tof}. This relation is found computing the convolution of a Gaussian distribution with the Maxwell-Boltzmann Green's function to find the density as a function of time. [Weiss et al., 1989].

The width of a thermal distribution in a harmonic trap of oscillation frequency ω is well described by: $\sigma_x(0) = \sqrt{k_B T/M\omega^2}$, such that:

$$\begin{aligned}\sigma_x(t_{tof})^2 =& \frac{k_B T}{M\omega^2} + \frac{k_B T}{M} t_{tof}^2, \\ =& \frac{k_B}{M}\left(1/\omega^2 + t_{tof}^2\right) T, \end{aligned} \tag{65}$$

therefore T can be estimated by linearly fitting $\sigma_x(t)^2$ vs t_{tof}^2. When the time-of-flight t_{tof} is much longer than the oscillation period of the trap we can make the approximation:

$$\sigma_x(t_{tof})^2 \simeq \frac{k_B T}{M} t_{tof}^2 \tag{66}$$

this allows us to estimate T from only one measurement of $\sigma_x(t_{tof})$, which is obtained by fitting the optical density of the atoms after an expansion time t_{tof}.

5.5 LOADING THERMAL ATOMS INTO A DIPOLE TRAP

A sketch of the evolution of the most relevant parameters during the sequence is shown in Figure 23. In the following sections we give more details on each step of the experimental sequence.

5.5.1 *3D MOT*

We form a 3D MOT directly from background pressure. The loading sequence is as follow: we shine the six cooling beams 15 MHz detuned from the $|5S_{1/2}, F = 2\rangle \rightarrow |5P_{3/2}, F' = 3\rangle$ transition and power around 20 mW each, the intensity of the light is then well above the saturation intensity, $7\,mW/cm^2$ for the re-expanded beams. At the same time we shine the repumper beam resonant with the $|5S_{1/2}, F = 1\rangle \rightarrow |5P_{3/2}, F' = 2\rangle$ transition but much lower power, only 0.5 mW per beam. The gradient field is kept on at 11 G/cm by circulating 8 A of current in the MOT coils.

With these parameters we are able to collect from 10^8 to 10^9 atoms in 10 s to 40 s depending on the background pressure. We have calibrated that the MOT loading time is 40 s when the pressure is 4×10^{-11} Torr and because the loading time scales inversely proportional to the pressure [Arpornthip et al., 2012], a

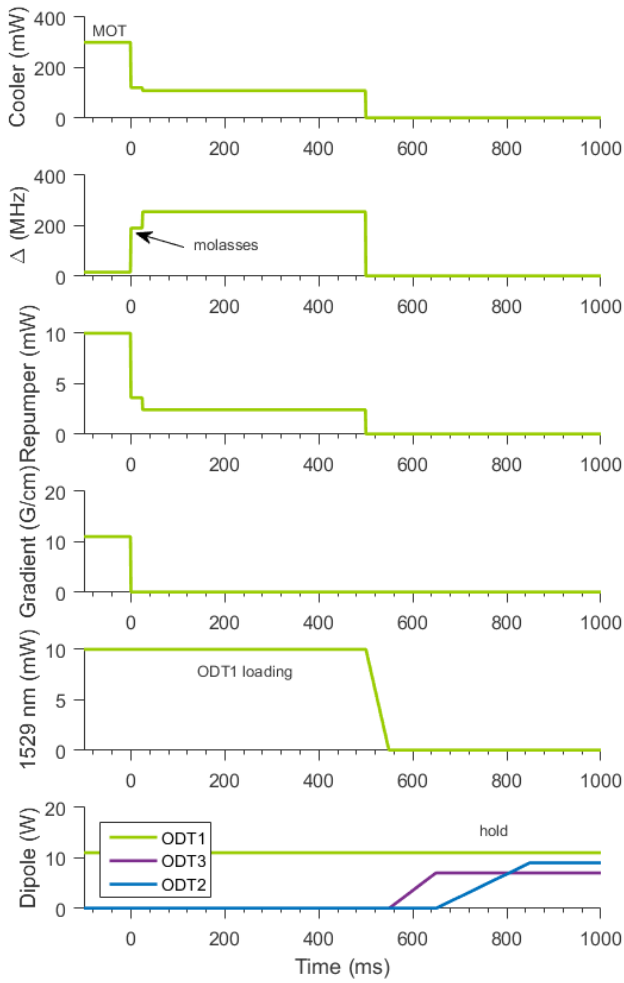

Figure 23: Evolution of the most relevant parameters during the loading sequence of the dipole trap.

loading time of 10 s indicates a pressure of around 2×10^{-10} Torr. The atoms in the MOT have an average temperature of 150 µK to 400 µK.

With a fully loaded MOT we proceed with a Molasses phase where we further detune the cooling beam to 190 MHz on the red

from the $|5S_{1/2}, F = 2\rangle \rightarrow |5P_{3/2}, F' = 3\rangle$ transition, reduce the repumper power by a factor of three and switch off the gradient field. This technique cools down the atoms below 20 µK in 20 ms. We use the temperature of the molasses to adjust the bias magnetic field compensation. A slow isotropic expansion indicates a good zero magnetic bias.

In our experiment the bias that has to be compensated is mainly the earth magnetic field which in the laboratory is 0.454 G [NGDC], the only source of high field around is the magnets of the ion pump which are shielded (see Figure 3) and generate a maximum field nearby the chamber of 0.56 G.

5.5.2 *Transfer to an optical dipole trap*

Because the wavelength of the ODT laser (1560 nm) is close to the transition $|5P_{3/2}\rangle \rightarrow |4D_{3/2,5/2}\rangle$, a large differential lightshift is induced in the trap region: the red shift caused by the dipole in $|5P_{3/2}\rangle$ is 47.7 times stronger than that caused in $|5S_{1/2}\rangle$ due to the difference in values of the scalar polarizability for each level [Bernon, 2011]. This differential light-shift offers the possibility to perform a tomography of the atoms in the trap [Brantut et al., 2008] and provides an inherent mechanism to create an effective dark- MOT at the center of the trap, which could in principle allow to reach higher densities after the loading [Clément et al., 2009]. The loading process of this trap is, nevertheless more delicate compared to most experiments using dipole traps at 1064 nm. In this section we will detail the procedure that allows us to load up to $\simeq 7 \times 10^6$ atoms.

In an old version of the experiment the trap was designed to have a maximum differential lightshift of around 250 MHz to be able to exploit the dark-MOT technique: the cooler beam is far detuned to be well on the red side of the $|5S_{1/2}, F = 2\rangle \rightarrow |5P_{3/2}, F' = 3\rangle$ transition without crossing to the red side of the $|5S_{1/2}, F = 2\rangle \rightarrow |5P_{3/2}, F' = 2\rangle$ and still provide some cooling in all the spatial region (with and without dipole beam). The repump beam, on the other hand, is resonant in free-space but blue detuned at the center of the trap thanks to the lightshift in-

duce by the trap. The fact the repumper is less efficient at higher intensity regions of the trap, allow the atoms to accumulate in the $|F = 1\rangle$ state, where higher densities can be achieved as the reabsorption of scattered photons by atoms undergoing multiple excitations in the cooling cycle are avoided and trap loss due to excited state collisions drop [Ketterle et al., 1993].

This old trap allowed us to optimize the key parameters during the loading finding the following results:

1. repumper: power has to be very weak to avoid repumping atoms back from $|F = 1\rangle$ to $|F = 2\rangle$, set to 200 µW per arm.

2. cooler power is similar to molasses optimum power 10 mW per arm, the detuning optimum is 255 MHz, right above the $|5S_{1/2}, F = 2\rangle \rightarrow |5P_{3/2}, F' = 2\rangle$ transition. As shown in the scan Figure 24 a sharp loss on the loaded atoms is observed when the cooling light crosses to the blue side of $|5S_{1/2}, F = 2\rangle \rightarrow |5P_{3/2}, F' = 2\rangle$ where cooling can not occur any more.

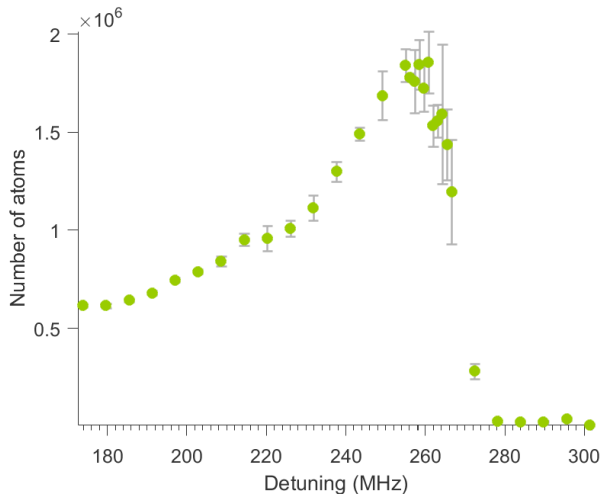

Figure 24: Number of atoms loaded versus detuning of the cooler beam from the closed transition $|5S_{1/2}, F = 2\rangle \rightarrow |5P_{3/2}, F' = 3\rangle$.

3. ODT loading time is limited by the lifetime of cold atoms reservoir (Figure 25), typically 500 ms.

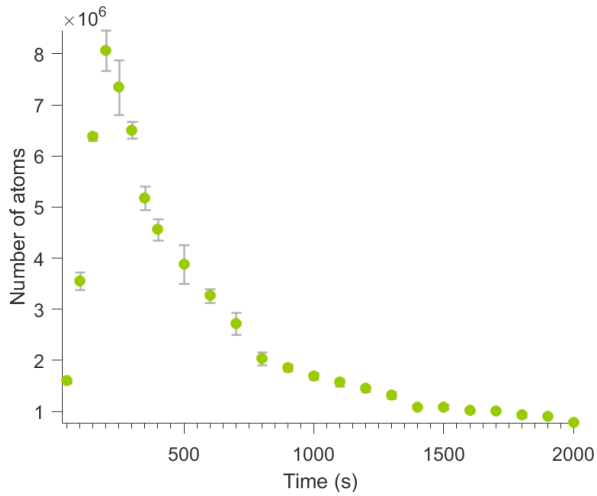

Figure 25: Finite lifetime of reservoir of cold atoms undergoing molasses phase.

This first trap was a beam focused to 55 µm and 11 W of power and an orthogonal beam focused to 70 µm and 7 W of power. We modified the geometry of this trap for we could not observe a condensate evaporating in such a trap. I'll give more detail on this in the evaporation section. One of the key parameters on the new design which allowed us to achieve condensation was increasing the volume of collection keeping a high two body collision rate and deep potential depth without weak escape channels.

In the current design, ODT1 has 11 W of maximum power and 45 µm waist, inducing a potential with depth $-320\,\mu K$ according to Equation 57. This potential depth is equivalent to a shift of the ground state of 6.7 MHz whereas for the excited state is 318 MHz. The differential lightshift at the center of the trap is then 308 MHz. Notice that the maximum differential lightshift is larger than the hyperfine splitting between $|F' = 2\rangle$ and $|F' = 3\rangle$ which is 266.65 MHz as sketched in Figure 26. This large differential lightshift complicates the loading of the trap as the cooler will always be blue detuned at the center of the trap.

There are two things than can be done to overcome such a limitation. The first one is to reduce the power of ODT1 during

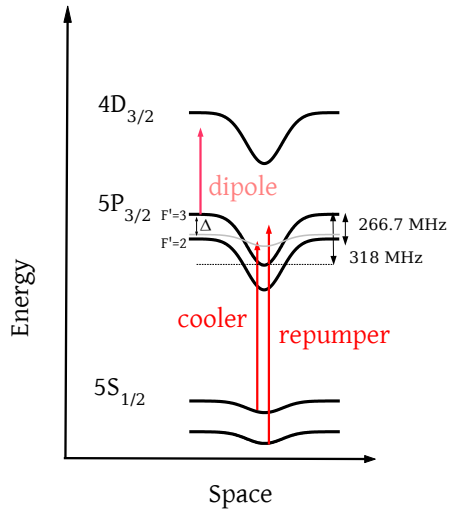

Figure 26: Sketch (not to scale) of differential lightshifts induce by the dipole trap which can be exploited to create a dark MOT at the center of the dipole trap.

the loading process such that the maximum differential lightshift never exceeds 266.65 MHz. We have confirmed the number of atoms loaded is maximum for a loading power of 8.5 W as shown in Figure 27 and limited to 4.5×10^6atoms.

The second approach consists in compensating the excessive differential lightshift in order to be able to load ODT1 with maximum power and therefore exploit the benefits of having maximum depth in all the spatial extension of the trap. We implemented this strategy shining a laser with a wavelength of 1529.20 nm, which is blue detuned from the $|5P_{3/2}\rangle \rightarrow |4D_{3/2,5/2}\rangle$ transitions. The idea is illustrated in Figure 28 where continuous lines correspond to the effective bending of the energy levels in presence of both the dipole at 1560 nm and the blue laser at 1520.2 nm and the dashed lines the lightshift induce by only the dipole.

In order for this compensation to work, the mode match of both lasers has to be nearly perfect. We have adjusted the size and alignment of the compensating beam profiling the combined beams with the beam profiler (BP209-IR/M, Thorlabs) at the focus point. The optics of the compensating beam is the same as for

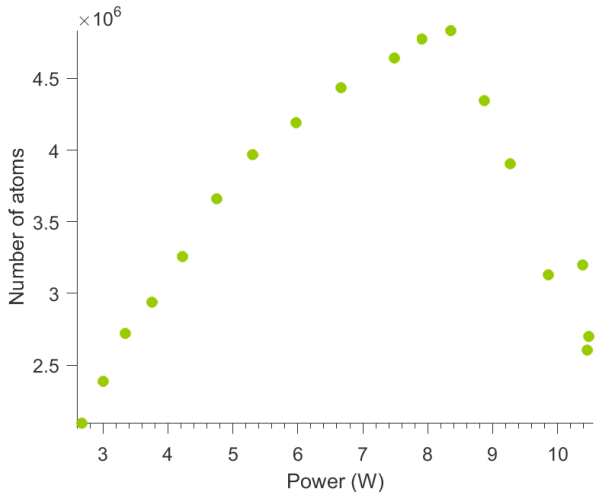

Figure 27: Number of atoms loaded as function of ODT1 power in absence of the compensating beam.

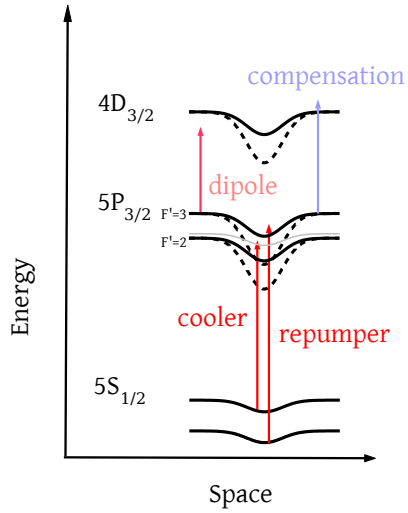

Figure 28: Sketch (not to scale) of differential lightshift compensation of the $|5S_{1/2}, F = 2\rangle \rightarrow |5P_{3/2}, F' = 3\rangle$ transition to be able to implement the dark MOT loading technique.

ODT1, and because both wavelegths are very similar, fine tuning of the beam divergence using the adjustability of the output collimator (PAF-X-7-C,Thorlabs), is enough to match the waists. Mir-

rors before the combining PBS (ODT1 and compensating beam have orthogonal polarizations) allow one to beam walk the compensating beam and perfectly overlap with the dipole. The measured waists of the beam are: $D4\sigma_x = 96\,\mu m$ and $D4\sigma_y = 87\,\mu m$.

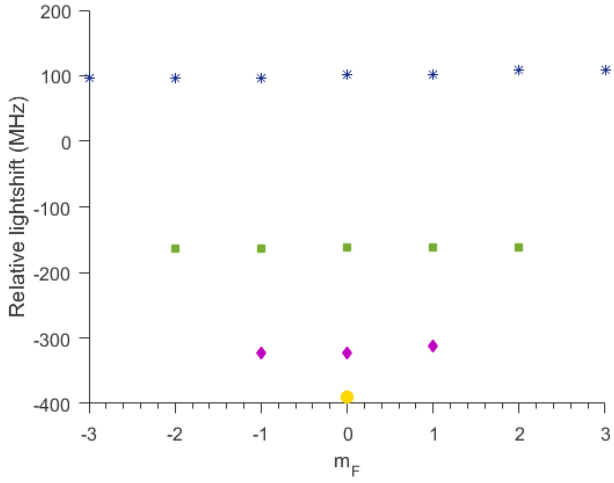

Figure 29: Lightshifts of the excited state in the presence of 6 mW of 1529.22 nm. Blue asterisk, green squares, violet diamonds and yellow bullets show the lightshift for $|F' = 3, 2, 1, 0\rangle$ states, respectively, relative to the $|F' = 3\rangle$ state in free space. Courtesy of Simon Coop. Estimations based on Floquet theory as in [Coop et al.].

Using the compensation we were able to load up to 7×10^6 atoms, 50% more with respect to the best scenario without compensation. We found the best compromise between wavelength and power scanning the power of the compensating beam for different wavelengths. This laser is not frequency stabilized and therefore large detunings were chosen to be less sensitive to drifts. The best results where found for a detuning of 0.04 nm $\lambda =$ 1529.22 nm and 6 mW power. For the power and wavelength of the compensating beam we have estimated a polarizability of the excited state $\alpha_{5P_{3/2}}(\lambda = 1529.22\,nm, 6\,mW) \simeq 8.2 \times 10^{-35}\,J/(V/m)^2$. As shown in Figure 29 the lightshift induced in the $|F' = 3\rangle$ state is 100 MHz on the blue side respect that in free space, as well as

the states $|F' = 2, 1, 0\rangle$. Energies are shown relative to the $|F' = 3\rangle$ state.

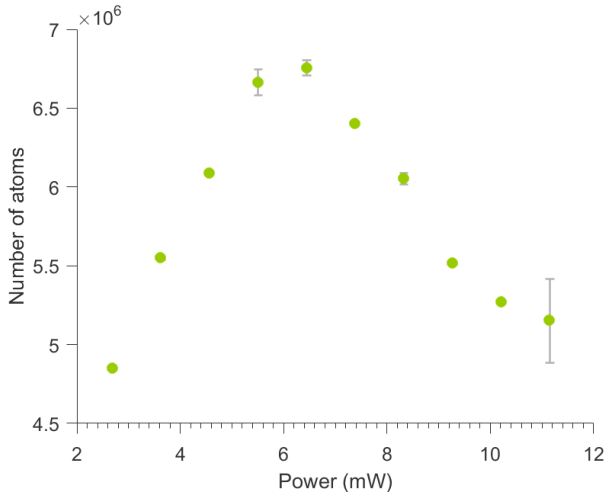

Figure 30: Number of atoms loaded in ODT1 at full power as a function of the power scan of the compensating beam at 1529.22 nm.

After we load ODT1 we ramp down the compensating beam power ending up with 7×10^6atoms at 50 uK in a potential that has large curvatures in the plane yz and very low in the propagation direction **x**.

In order to increase the curvature along **x** we ramp up the power of ODT3 in 100 ms. This boosts the mean oscillation frequency of the full trap and therefore speeds up the collisional dynamics which provides thermalization.

Finally, we ramp up ODT2 power in 200 ms which at the beginning provides an escape channel at a lower energy and forms a dimple beam which is key at the end of the evaporation as we will show in Chapter 6. The total hold time after loading is therefore 350 ms time during which free evaporation occurs. We end up with typically 5.5×10^6 atoms thermalized at 50 µK.

6

CREATING AN SPINOR BEC: ALL-OPTICAL EVAPORATION

As discussed in previous chapter, laser cooling in MOTs is fundamentally limited by the Doppler effect, setting the minimum attainable temperature to 145.57 μK in ^{87}Rb [Steck, 2001]. Further cooling has been achieved by other laser cooling techniques like optical molasses where the recoil energy involved in the scattering process places a new limitation on the minimum reachable temperature (361.96 nK for ^{87}Rb). Beyond the recoil limit techniques like Raman sideband cooling have been developed, where not only the limit on the temperature is pushed but also the obtainable phase-space densities as compared to conventional molasses (2×10^{-3}) [Kerman et al., 2000], desirable scenario when condensation is pursued. Other techniques like velocity-selective coherent population trapping have been developed to reach temperatures below the recoil limit [Aspect et al., 1988], as well as the more conventional evaporative cooling [Ketterle and Druten, 1996].

In order to produce a condensate, we follow the conventional strategy for ^{87}Rb which is MOT, molasses and forced evaporation. In this chapter I describe in detail the last evaporative phase.

Forced evaporation is a technique that exploits the shape of the Maxwell-Boltzmann distribution of the atoms in the sense that the high thermal energy tail is cut by the release of the hottest atoms. A subsequent process of re-thermalization among the remaining atoms is essential to achieve the desired lower temperature equilibrium. Such a mechanism is two-body elastic collision.

thermal quasiequilibrium, strictly speaking

The first evaporative cooling implementation that lead to condensation was done in a magnetic trap [Anderson et al., 1995] where only low-field seeking states can be trapped. Such traps were for a long time the ubiquitous cold atom traps, often created

by a quadrupole magnetic field and a rotating bias field (TOP traps) to avoid zero field crossing which cause atom losses due to Majorana spin-flip transitions [Brink and Sukumar, 2006]. The associated frequencies of the trap in the harmonic approximation scale with the square of the quadrupole field and are inherently anisotropic at high values of the field strength. More complicated geometries have to be implemented to create an isotropic trap with only magnetic fields [Lobser D. S. et al., 2015; Hodby et al., 2000]. Strong magnetic fields are required to have deep traps and yet the oscillation frequencies are low ($\simeq 100\,\mathrm{Hz}$). This sets high requirements to the vacuum environment to have long lifetimes (associated to background collisions) since low oscillation frequencies imply slow thermalization process and therefore evaporation times that typically exceed 30 s.

A different strategy was developed in Chapman's group: all-optical evaporation where atoms are trapped in a state insensitive optical potential (all the m_F magnetic sublevels are trapped), and the hottest atoms are removed by lowering the confining potential itself. For many experimental configurations it is technically easier to generate high-curvature potentials with optical fields, therefore optical traps can easily provide high oscillation frequencies above 1 kHz, which boosts the collision rates and reduces the evaporation time to typically a few seconds.

In the all-optical evaporation strategy not only the potential depth of the trap is modified but also the curvature of the trap, which in turn, modifies the collisional dynamics of the remaining atoms. In order to better understand the process, a theoretical description is done in the next sections.

6.1 THEORETICAL UNDERSTANDING OF ALL-OPTICAL EVAPORATION COOLING

The system consists of N ^{87}Rb bosons with mass M at temperature T, confined in a 3D harmonic trap with oscillation frequencies such that the geometric mean is $\bar{\omega} = (\omega_x\omega_y\omega_z)^{1/3}$. The scattering cross section is $\sigma = 8\pi a^2$, being a the relevant scattering length of the collision channel, in our case a_0 for $|F = 1\rangle$ (see

Table 1). For this system we explicitly write the relevant parameters: [Olson et al., 2013]

The phase-space density:

$$\rho = N\left(\frac{\hbar\bar{\omega}}{k_B T}\right)^3 = n_0\lambda_{dB}^3 \tag{67}$$

the peak density:

$$n_0 = N\bar{\omega}^3\left(\frac{M}{2\pi k_B T}\right)^{3/2} \tag{68}$$

the de Broglie wavelength:

$$\lambda_{dB} = \sqrt{\frac{2\pi\hbar^2}{M k_B T}} \tag{69}$$

and the two body collision rate [O'Hara et al., 2001]:

$$\gamma = 4\pi N\sigma\bar{v}^3\frac{M}{k_B T} \tag{70}$$

or [Olson et al., 2013]

$$\gamma = n_0\sigma\bar{v}\frac{1}{2\sqrt{2}} \tag{71}$$

for the mean velocity: $\bar{v} = 4\sqrt{k_B T/(\pi M)}$ and atoms trapped in a 3D harmonic potential.

The phase transition to a condensed state in a 3D harmonic potential is expected to appear when the phase-space density is $\rho = \zeta(3)$ where $\zeta(3) \simeq 1.202$ is the Riemann zeta function or, equivalently, with the temperature is below the critical temperature: [Pethick and Smith, 2002]

$$T_c = \frac{\hbar\bar{\omega}}{k_B}\left(\frac{N}{\zeta(3)}\right)^{1/3}. \tag{72}$$

As a tool to qualitatively understand evaporation cooling in optical traps, scaling laws have been written to describe number of atoms N, phase space density ρ and collision rate γ along the evaporative process.

Scaling laws

For the sake of simplicity one can assume the confining trap is adiabatically lowered in such a way that the mean oscillation frequency $\bar{\omega}$ scales with the potential depth as $\sqrt{U(t)}$. This is true for a single Gaussian beam with given waist and power being lowered, as the frequencies scale proportionally to $\sqrt{P}$, while the potential scales as P. A second supposition is to consider the ratio between the potential depth and the temperature of the atoms $\eta \equiv U(t)/T$ remains constant. Under these conditions and assuming $\eta \gg 1$ [O'Hara et al., 2001] deduced the following scaling laws for the number of atoms, the elastic collision rate and the phase space density as the continuous evaporation takes place:

$$\begin{aligned}
\frac{N(t)}{N_0} &= \left(\frac{U(t)}{U_0}\right)^{3/(2\eta'-6)}, \\
\frac{\gamma(t)}{\gamma_0} &= \left(\frac{U(t)}{U_0}\right)^{\eta'/(2\eta'-6)}, \\
\frac{\rho(t)}{\rho_0} &= \left(\frac{N_0}{N(t)}\right)^{\eta'-4}.
\end{aligned} \tag{73}$$

where $\eta' = \eta + (\eta-5)/(\eta-4)$. If we plot the predicted final values as a function of the parameter η assuming the final gain in phase-space density has to be 10^3 (see Figure 31) we can notice that for high values of η great gain in phase-space density is possible at the expense of a moderate decrease on number of atoms.

It has been assumed the value of η stays constant which defines the time evolution of the potential. The specific evolution was found to be:

$$U(t) = U_o\,[1 + At\gamma_o]^{(-2\eta'+6)/\eta'}, \tag{74}$$

$$A = \frac{2}{3}\eta'(\eta-4)\exp\{-\eta\}. \tag{75}$$

From previous expressions we can estimate the time it would take to increase the phase-space density by a factor of 1×10^3

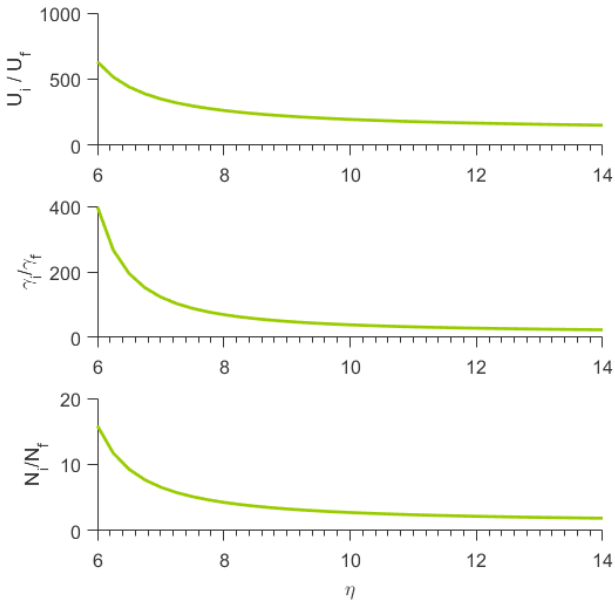

Figure 31: Scaling laws during forced all-optical evaporation as a function of parameter η [O'Hara et al., 2001].

for example. As function of η we plot the ratio t_{evap}/γ_0 in Figure 32 where we can identify an order of magnitude for the collision rate so the evaporation lasts only a few seconds: around 1×10^4 Hz. We can also notice that for large values of $\eta > 10$ the evaporation rate slows down dramatically, because of which is preferable to quickly ramp down the trap at the beginning of the evaporation to decrease η and to be in better conditions to proceed with the evaporation.

These laws have successfully described experiments like [Barrett et al., 2001] and provide a good first insight into the expected evolution of the phase-space density and the necessary initial conditions. From these scaling laws we have learned our trap should provide initial collision rates around 1×10^4 Hz and that η should be around 8 to minimize the evaporation time. It is useful to see how other groups have achieved condensation. In Table 4 we make a list of some examples.

we designed the trap based on this values as well as the anisotropy requirements discussed in the following sections.

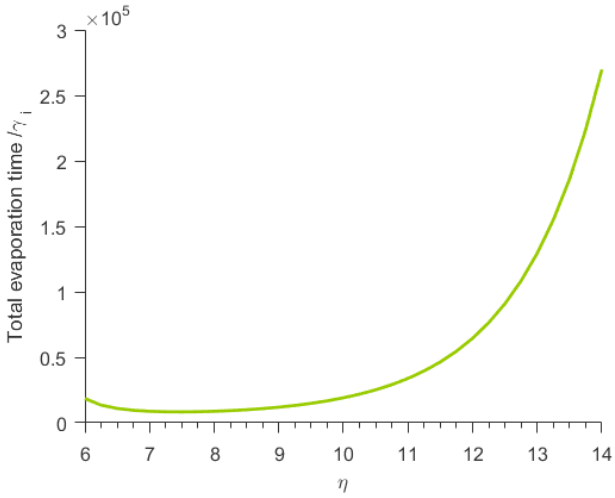

Figure 32: Expected evaporation time needed to increase the phase-space density by a factor of 10^3 per elastic collision rate as a function of η.

Notice all of them have very similar conditions $\gamma \simeq 2 \times 10^4$ Hz and $\eta \simeq 9$ but the final number of atoms they achieve is about two orders of magnitude lower than the initial (last three cases), a much greater loss with respect to what is predicted by the scaling laws.

The *efficiency of the evaporation* describes the gain in phase-space density per atoms lost and is quantified as follows:

$$\gamma_{eff} = -\frac{\ln(\rho_f/\rho_0)}{\ln(N_f/N_0)}. \tag{76}$$

Before describing our approach I would like to point out that better efficiencies of the evaporation can be attained as in the case shown in Table 4 from [Olson et al., 2013]. They found that in the more general case $\bar{\omega}(t) \propto [U(t)]^{\nu}$, one can write the evolution equations for the energy and the number of atoms based on Kinetic theory, and concluded it is possible to find optimum ν and η values for each initial conditions such that the final number of atoms in the condensate is the maximum possible.

Reference:	[Olson et al., 2013]	[Barrett et al., 2001]	[Clément et al., 2009]	[Arnold and Barrett, 2011]
N_0	5×10^5	2×10^6	3×10^6	2×10^6
T_0 (μK)	60	75	65	200
$\bar{\omega}_0$ (rad/s)	$2\pi \cdot 1000$	$2\pi \cdot 1500$	$2\pi \cdot 1200$	$2\pi \cdot 1200$
γ_0 (Hz)	2.4×10^4	2.6×10^4	2.3×10^4	5×10^3
ρ_0	2.5×10^{-4}	1.8×10^{-3}	2.1×10^{-3}	4.5×10^{-5}
γ_{1B}^{-1} (s)	12	6	-	6
η	8.5	7.2	11	10
ν	0.22	0.5	0	-
N_f	5×10^4	1.8×10^4	1.5×10^4	3.5×10^4
γ_{eff}	4	2.7	2.8	2.9

Table 4: Relevant parameters for all optical evaporation in different experiments that have achieved condensation.

Kinetic model of evaporative cooling

In the deep trap limit $\eta > 6$ [Olson et al., 2013] found that is possible to find optimum relations between T, U_0 and $\bar{\omega}$ for different initial conditions of the system, by solving the evolution equations for the energy E and the number of atoms:

$$\begin{aligned} \dot{E} &= -N\gamma_{ev}(\eta + \kappa)k_B T + \nu E\frac{\dot{T}}{T} - \gamma_{1B}E - \gamma_{3B}\frac{2}{3}E, \\ \dot{N} &= -(\gamma_{ev} + \gamma_{1B} + \gamma_{3B})N. \end{aligned} \tag{77}$$

The first terms describe the effects of evaporation where the evaporation rate is given by $\gamma_{ev} \simeq (\eta - 4)\exp\{-\eta\}\gamma$. The second term in the evolution of the energy accounts for trap shape changes which are negligible in the evolution of N. Finally the last two terms in both equations account for one and three-body loss respectively. γ_{1B} is the rate of losses due to background collisions $t_{lifetime} = \gamma_{1B}^{-1}$ and $\gamma_{3B} = K_3 n_0^2/(3\sqrt{3})$ where $K_3 = 4.3 \pm 1.8 \times 10^{-41}\,m^6/s$ for thermal atoms of ^{87}Rb in $|F = 1\rangle$ [Burt et al., 1997] and n_0 the peak density.

For the total energy of the system $E = 3Nk_BT$ one can solve system 77 as a function of both parameters ν and η and find the values that maximized the number of atoms in the condensate.

6.2 OUR INITIAL CONDITIONS

In our particular the initial experimental conditions are:

Parameter	ODT1 and ODT3	region ODT2 crossing
N_0	5.5×10^6 atoms	$\sim 2 \times 10^6$ atoms
T_0	50 µK	$\sim$ 50 µK
$\bar{\omega}_0$	$2\pi\cdot 430$ Hz	$2\pi\cdot 1.0$ kHz
γ_0	840 col/s	4×10^3 col/s
ρ_0	3.3×10^{-4}	1.8×10^{-3}

Table 5: Initial condition to optical evaporation in our experiment. See Section 5.5.2.

The number of atoms and temperature are measured with absorption imaging whereas the oscillation frequencies are measured with parametric excitation and breathing mode excitation. From those values we estimate the collision rate and the phase-space density. The lifetime of the trap is under typical background pressures 12 s. It is measured from the exponential decay of the number of atoms in hold time when the dipole trap is deep enough so no free evaporation occurs.

According to the kinetic model of the evaporation, maximum efficiency in our system is expected when $\eta = 8.5$ and $\nu = 0.45$, as shown in Figure 33.

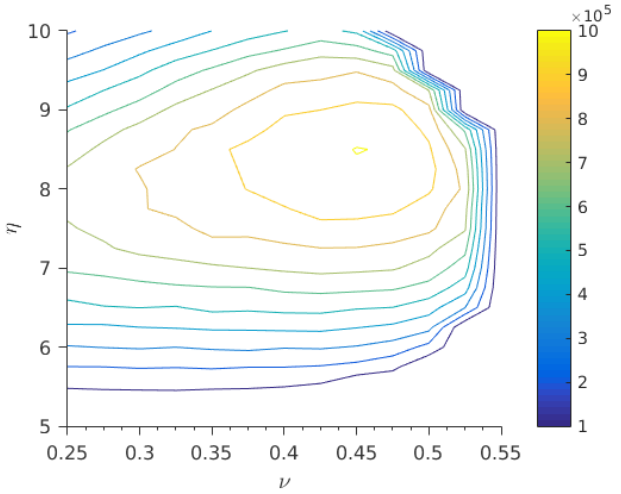

Figure 33: Expected N when crossing T_c for our initial conditions (Table 5).

To estimate the value of η we plot the potential depth of our trap at full power of only ODT1 and ODT3:

The effective potential depth is 410 MHz and therefore $\eta = 8.2$, very close to the optimum. When we add ODT2 at full power the potential is modify as follows:

Here we can see there a dimple like region along the propagation direction of ODT1 which at this point we will neglect. More important is the escape channel formed along the ODT2 propagation direction (eigenvector green line) at about 100 µK atoms that go into the arms formed by ODT2 do not come back to the center of the trap, the curvature is negligible. This would be the first evaporation channel for which the effective potential depth is around 410 µK. This is a good scenario for starting forced evaporation since η stays at the value 8.2.

One has to be specially careful with the scape channels created when working with cross traps, they effectively diminish the potential depth.

The optimum predicted value for our initial conditions is very close to 0.5, for this reason we just set the geometry where all beams cross at the waists and optimized the temporal evolution of the various dipole beam powers, to maximize the number of

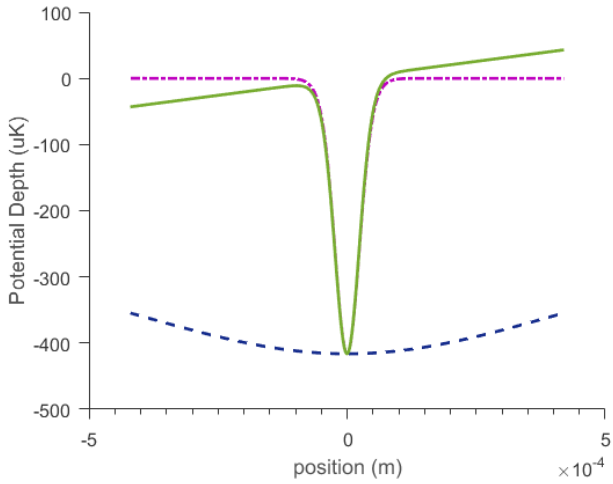

Figure 34: Potential depth of trap formed by ODT1 and ODT3.

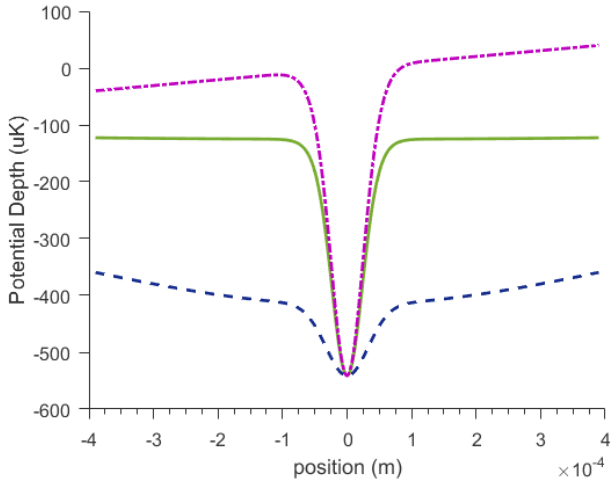

Figure 35: Potential depth of trap formed by ODT1, ODT2 and ODT3 at full power.

atoms at the end of the evaporation. Values of $\nu < 0.5$ require tailoring waist ratios, crossing points or ramp time constants of the different beams so that the potential depth changes without modifying so much the frequencies.

6.3 TEMPORAL EVOLUTION OF THE BEAM POWERS

We started fixing the total evaporation time to 5 s; the power evolution was divided in four segments with final power chosen so the number of atoms at the end of the evaporation was maximum. In this way we got our first condensate with 1.2×10^4 atoms in 5 s.

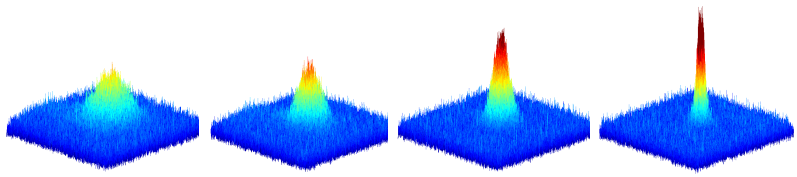

Figure 36: Time of flight images showing the momentum distribution of the atoms during the evaporation. A narrow peak emerging above the thermal distribution shows the unequivocal signature of a condensate. Images of our first BEC.

In order to improve the final number of atoms an algorithm based on the simplex method described in [Nelder and Mead, 1965] was implemented. It consist in the minimization of an objective function of n variables using the idea of a simplex (n+1 vertices "triangle") whose vertices represent test points of the function. It evaluates the function at each of those initial points and replaces the worse of them with a new one which is the reflected point through the centroid of the other points. If such a point provides a better result it tries to go further in the same direction; if that is not the case it brings closer all the points to the best point in the initial evaluation. Every time it choses a new test point it re-evaluates all the n+1 points, which is very convenient for our experiment since across the day the pressure of the chamber varies inducing drifts on the final number of atoms we condense.

The way we implemented is taking the powers of ODT1 and ODT2 at each point in time: $t = 3000, 3500, 4600, 5100$ ms as the variables, such that the figure of merit: $-N/\sigma$, obtained fitting one Gaussian to the final distribution (after 5100 ms of evaporation), is minimized. It is important to choose a proper figure

of merit that guaranties the final number of atoms in the condensate is maximum; maximizing for example only N_c from the fit of a double Gaussian is not ideal since it is difficult for the fit to distinguish what Gaussian corresponds to the thermal and which one to the condensate, this means the algorithm would converge to hold the traps at full power maximizing N_T.

The result of the algorithm was the power evolution shown in Figure 37, getting a pure condensate with 6×10^4 atoms in 4.8 s. Subsequent fine tunning of the dipole crossing allowed us to create a pure condensate with 1×10^5 atoms in just 4.5 s.

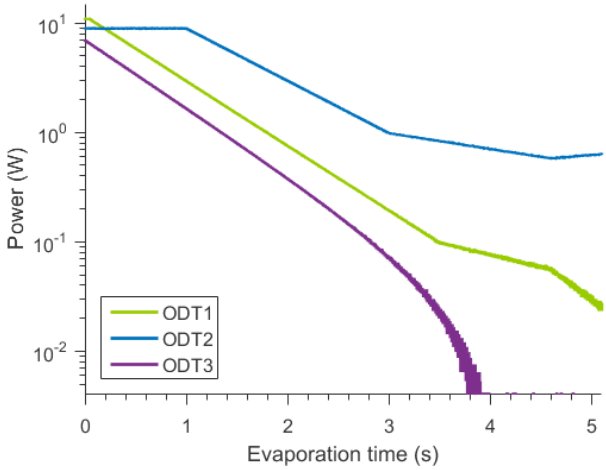

Figure 37: Measured optical powers of the three dipole beams as function of time. All-optical evaporation.

As an illustration of the importance of ODT2 we plot the evolution of N and T during evaporation with and without this beam. Notice that the lack of longitudinal confinement is especially important at later stages of the evaporation when rethermalization greatly slows as the rate of elastic collisions drop. Comparing Figure 38 and Figure 39 makes evident that condensation is not possible without the extra beam providing longitudinal confinement as well. Many groups implement a dimple beam at the end of evaporation for the same reason: re-boost collisions to proceed evaporation. We start with ODT2 from the beginning of the evap-

oration since it seems to benefit the final number of atoms with the increase of initial density in the crossing region.

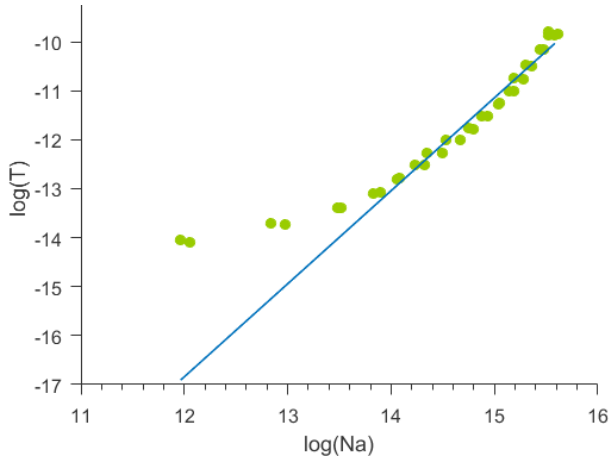

Figure 38: Evaporation efficiency in the space $\log(T) - \log(N)$ when the dipole trap is formed by only ODT1 and 3. This trap has a large volume but no tight longitudinal confinement, which provides no efficient evaporation at low temperatures.

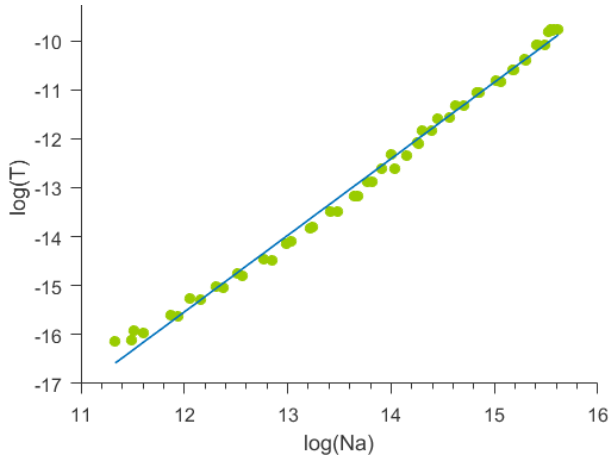

Figure 39: Evaporation efficiency in the space $\log(T) - \log(N)$ when the dipole trap is formed by ODT1,2 and 3. This trap has strong confinement in the three directions at low temperatures, which is essential for the rethermalization process to achieve condensation.

The system reaches $T_c = 140 \pm 5\,\mathrm{nK}$ with 2.3×10^5 atoms and produces a pure condensate (distribution with no visible thermal fraction) at $\rho_f = 2.5$ with 1×10^5 atoms. The efficiency of the evaporation is $\gamma_{eff} = 2.2$.

In order to estimate the final phase-space density we measure N, T and $\bar{\omega}$ at the end of the evaporation. N, T and c_F are measured by absorption imaging. To measure $\bar{\omega}$ we vary number of atoms we load into the dipole trap by varying the loading time. The final powers are fixed. Using Equation 72 and the well known relation for the condensed fraction:

$$c_F = 1 - \left(\frac{T}{T_c}\right)^3, \tag{78}$$

we estimate $\bar{\omega} = 2\pi \cdot 55 \pm 10\,\mathrm{rad/Hz}$ at the end of the evaporation (for more details, see Section 9.2).

According to the kinetic model of the evaporation in our initial conditions (see Figure 33), the system should reach T_c with three times more atoms for the assumed $\nu = 0.5$ relation. A possible explanation for this discrepancy is the following: we have observed that the position of the waist of the recycled beam ODT3 moves when decreasing the power of ODT1 diminishing the effective size at the atoms position. This suggests a softening of the trap with decreasing power, i.e. a trap-frequency to power relation with larger ν. By kinetic theory (as shown in Figure 33), this can be very detrimental to the efficiency if ν exceeds 0.5. Solving this problem should in principle ramp up the efficiency to the best possible value 3.8 boosting the number of atoms in the condensate to five times the current value.

6.4 MEASURING OSCILLATION FREQUENCIES

As we have previously described (Equation 58), the potential generated by various intersecting Gaussian beams can be approximated by a harmonic oscillator where the eigenvectors not necessarily match the axis of propagation of the beams. In this more general scenario we identify $\omega_i^2 = H_U(\mathbf{r}_o)_{ii}/m$ as the oscillation frequencies of the trap where H_U is the Hessian matrix

of the optical potential. The Hessian matrix is symmetrical assuming the second derivatives of the potential are continuous, which would be the case of a Gaussian function describing a beam. And because $U(\mathbf{r})$ is real $H_U(\mathbf{r})$ has only real components, this means that $H_U(\mathbf{r})$ is hermitian and therefore it exists a basis where the Hessian matrix is diagonal and where we can identify the eigenvalues as the oscillation frequencies of the trap ω_{ii}. Notice that the corresponding eigenvectors not necessarily will be the Cartesian system defined by the direction of propagation of the orthogonal beams. ODT3 propagates at a small angle with ODT1 and therefore the eigenvectors are rotated respect to the propagation axis of ODT1.

In order to estimate such frequencies we write the potential created by the three Gaussian beams in the configuration described in Section 5.3.3 with given powers and waists, find the minimum and calculate the Hessian matrix at this point. The matrix is then diagonalized to get the eigenvalues from which we estimate the oscillation frequencies.

In order to verify the actual frequencies of the trap at any point of the evaporation, two main techniques are used: breathing modes and parametric excitation. When there is only one beam and the eigenvectors are unambiguous the simplest way to measure the frequency is by exciting the atoms for example by releasing them from the dipole trap for 1 ms to allow them to freely fall before we recapture them. The width of the distribution of the recaptured atoms would follow a damped oscillation at the breathing mode frequency which is twice the resonance frequency of the trap. A breathing mode excitation example is shown in Figure 40.

We measure the oscillation frequencies for different powers of ODT1 (see Table 6) confirming our prediction based on Equation 59 and the measured waist, finding the relation $\log(\omega) \propto 0.52 \log(P)$, very close to the expected scaling 0.5.

We have observed that in ODT2, in contrast to ODT1, there are thermal effects that alter the waist size of the beam as a function of optical power. This has the consequence that the curvature of the potential or the oscillation frequencies drops faster than

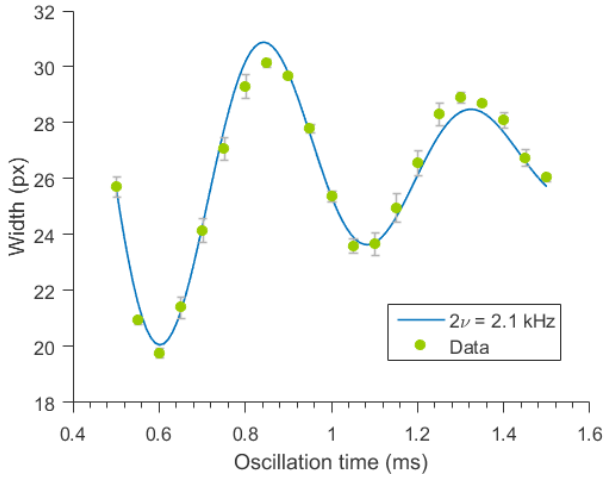

Figure 40: Breathing mode excitation of ODT1 at full power.

expected with optical power. This is reflected in the measured scaling of the waist size with power: $\log(w) \propto 0.68 \log(P)$.

Parametric excitation on the other hand can show the frequencies of a trap formed by more than one beam. The concept is to perturb a parameter, in this case the trap restoring force in a periodic way. When the periodicity is twice the natural period a maximal transfer of energy occurs. Higher orders nevertheless can also add energy to the system $\omega = 2\omega_o/n$ for any natural n [Landau and Lifschitz, 1969; Butikov, 2004]. In typical experi-

P(W)	ω(rad/Hz)
$1P_0$	$2\pi \cdot 1071$
$1/2P_0$	$2\pi \cdot 720$
$1/4P_0$	$2\pi \cdot 507$
$1/8P_0$	$2\pi \cdot 350$
$1/16P_0$	$2\pi \cdot 262$

Table 6: Measured oscillation frequencies of ODT1 for different powers. $P_0 = 11W$.

ment only the parametric resonances at twice and once the trap frequency are usually observed [Grimm et al., 2000].

The way we experimentally observe parametric excitations is by modulating the optical power of the dipole trap with a sinusoidal function with an amplitude typically $5-10\%$ the maximum power during 500 cycles. A minimum energy is needed to cause such excitations, the increment of energy during a period has to be larger than the amount of energy dissipated by friction during the same time [Butikov, 2004], but if the excitation is too strong the atoms occupy the anharmonic regions of the trap resulting in a broadening of the resonances.

An example of the parametric excitation signal is shown in Figure 41 at a very late stage of the evaporation when $P1 = 0.1\,W$ and $P2 = 2\,W$ and only the ODT2 is excited. We measure $\omega = 2\pi \cdot 110\,rad/Hz$, much lower compared to our estimates assuming the waists are constant with power.

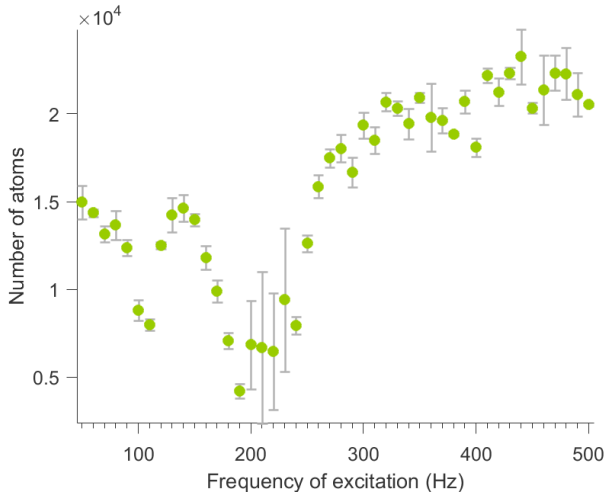

Figure 41: Parametric excitation of ODT2 in the presence of ODT1 (not excited), shows losses at 2ν and $\nu = 110\,Hz$

As an illustration Figure 42 shows the change in the losses when different dipole beams are modulated, the frequencies then can be identified as correspondent to the given excited beam.

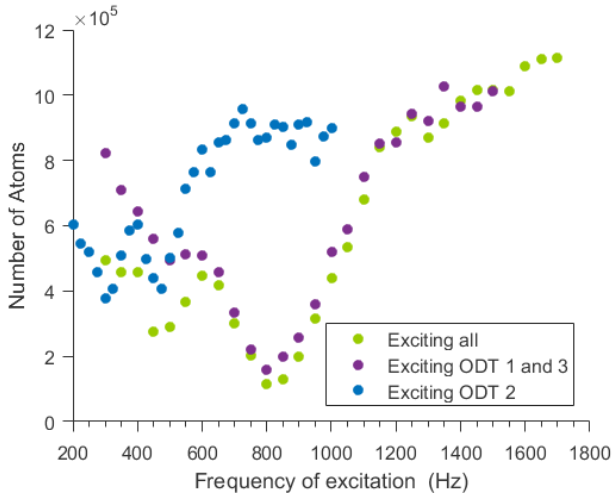

Figure 42: Example of selective parametric excitation.

6.5 SMOKING-GUN: CHARACTERIZATION

It is well known a signature that unequivocally shows the existence of a condensate is a narrow peak that come into sight over a thermal distribution in coordinate and momentum space. Because it is more simple to look at the momentum distribution, most groups image the atoms after a long time of ballistic expansion (about 30 ms) when only information about the momentum of the distribution is left. Such images shows a double structure composed by a thermal distribution, Gaussian, and a Thomas-Fermi one, a parabola. A thermal cloud occupies many energy states and therefore its distribution in momentum space is isotropic, in accordance to the equipartition principle. This means that no matter the initial spatial distribution in the trap the final momentum distribution is going to be isotropic. This is not the case for a condensate for which momentum distribution is determined, not by the thermal energy, but by a combination of trap geometry and pressure due to other atoms. This means that an anisotropic spatial distribution of condensed atoms correspond to an anisotropic momentum distribution. This clear distinction is a very powerful tool to demonstrate the existence of a condensed cloud.

the equipartition theorem doesn't hold anymore

The fact that the high density peak in a Thomas-Fermi distribution appears at the center of the Thermal distribution is due to the slower expansion of the condensed cloud respect to the thermal fraction. This is not the case in all spatial directions, as we will see in the following.

6.5.0.1 *Thermal expansion under free falling*

The size of a thermal distribution in a harmonic oscillator can be approximated as $R_T(0) = \sqrt{k_B T/M\omega^2}$ [Pethick and Smith, 2002], where R_T this is the standard deviation of the Gaussian distribution in the harmonic trap. It expands according to:

$$R_T(t) = \sqrt{R_T(0)^2 + \frac{k_B T}{M} t^2} \tag{79}$$

where we can see that for long expansion times the initial size of the cloud become irrelevant. A condensate with no interactions has the size:

$$R_{ni} = \sqrt{\frac{\hbar}{M\omega}} \tag{80}$$

but when interactions are taken into account and under Thomas-Fermi approximation the size becomes (see [Dalfovo et al., 1999]):

$$R_{TF} = R_{ni} \left(\frac{15 N a_0}{R_{ni}} \right)^{1/5} \tag{81}$$

According to [Castin and Dum, 1996] the equations describing the expansion of the condensate when suddenly opening the trap ($\omega_i(t) = 0,\ \forall t \neq 0$) read:

$$\frac{d^2 l_i}{dt^2} = \frac{\omega_i^2}{l_i l_x l_y l_z} - \omega_i^2(t) l_i,\ i = x, y, z \tag{82}$$

where $l_i(t)$ indicate the evolution of the size of the condensate in the direction i such that $R_{TF,i}(t) = l_i(t) R_{TF,i}(0)$ The initial conditions are $l_i(0) = 1$ and, because the gas is initially at rest,

$\dot{l}_i(0) = 1$. In the illustrating case of an anisotropic trap with $\omega_x = \omega_y = \omega_\perp$ and ω_z, one can solve Equation 82 for l_z and $l_\perp$ to find the expected size of the condensate as function of the expansion time for different values of the anisotropy parameter $\lambda = \omega_z/\omega_\perp$. In Figure 43 we show the ratio between a thermal cloud with same initial conditions and the same expansion time, with the estimated size of the condensate.

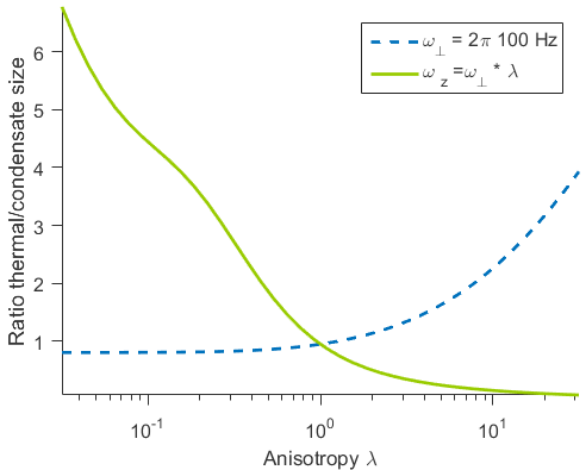

Figure 43: R_T/R_{TF} vs λ after an expansion time of 20 ms from the release of a dipole trap with frequencies $\omega_\perp, \omega_z$.

Notice that in order to distinguish a condensate as a peak at the center of the distribution this ratio has to be greater than one. This is the case when the anisotropy is prominent; for $\lambda < 1$ the peak would appear only the **z** direction, the weakest confined, whereas for $\lambda > 1$ the peak appears in the transversal direction, in this case also the weakest confined.

Another interesting consequence of Equation 82 is the evolution of the aspect ratio of the anisotropic distribution. Because the transverse and longitudinal direction evolve differently $\propto 1/l_\perp^3 l_z$ and $\propto 1/l_\perp^2 l_z^2$ respectively, there is a time where the radii are equal and from which the anisotropy inverts. This is not the case for a thermal distribution as previously discussed, when the anisotropy converges to 1.

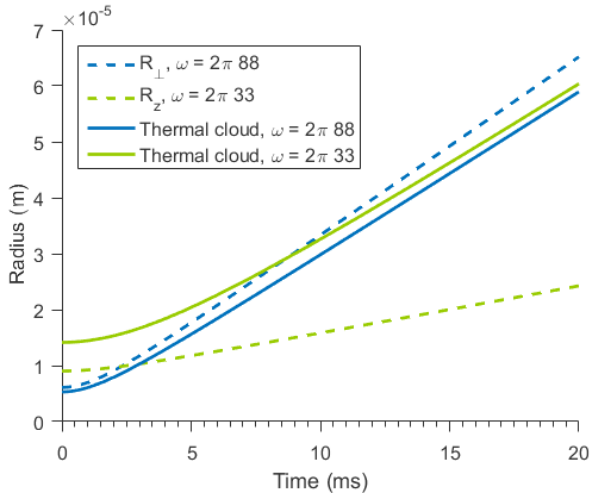

Figure 44: Expected size of the expanding cloud (condensed or thermal) as a function of t_{tof} for the estimated final geometry of our trap.

For different expansion times we plot the aspect ratio of the two Thomas-Fermi radii on the projected space. We confirm the inversion of the aspect ratio as shown in Figure 45.

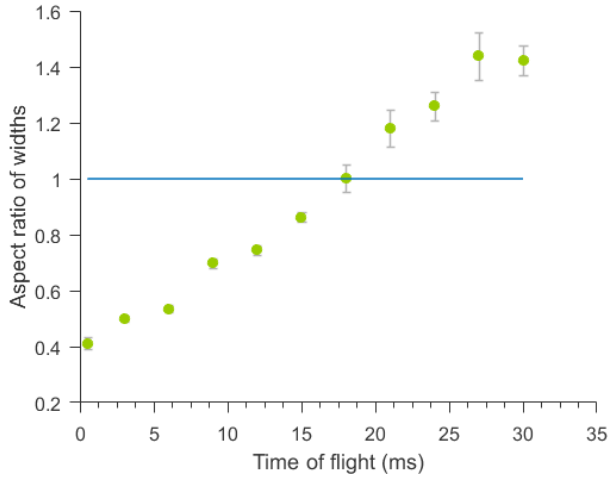

Figure 45: Inversion of aspect ratio of the original Thomas-Fermi distribution after expansion. Projected space.

Imaging

In order to estimate the number of atoms in the condensate we fit the 1D optical density (see Figure 46) to a bimodal function of two Gaussians or a Gaussian and a parabola:

$$\begin{aligned} OD|_{1D} =& OD_{TF}^{peak} Max\left[1-\frac{(x-x_0)^2}{R_{TF}^2}, 0\right] + \\ & OD_{T}^{peak} \exp\left\{-\frac{(x-x_0)^2}{2R_{T}^2}\right\} + offset; \end{aligned} \tag{83}$$

From the Gaussian part we estimate the number of atoms in the thermal fraction N_T (see Equation 60), the total N is found integrating the fit so we can know the number of atoms in the condensate $N_c = N_{tot} - N_T$. Knowing the number of atoms total and in the condensate, we get the condensed fraction $c_F = N_c/N_{tot}$. The Figure 46 below shows the formation of the condensate as we increase the evaporation time and the 1D integrated signals used to fit Equation 83.

HINTS

In order to optimize the crossing alignment of the ODTs the best strategy is to go to late stages of the evaporation where holding the atoms is much more sensitive, only a precisely crossing trap can hold the atoms against gravity.

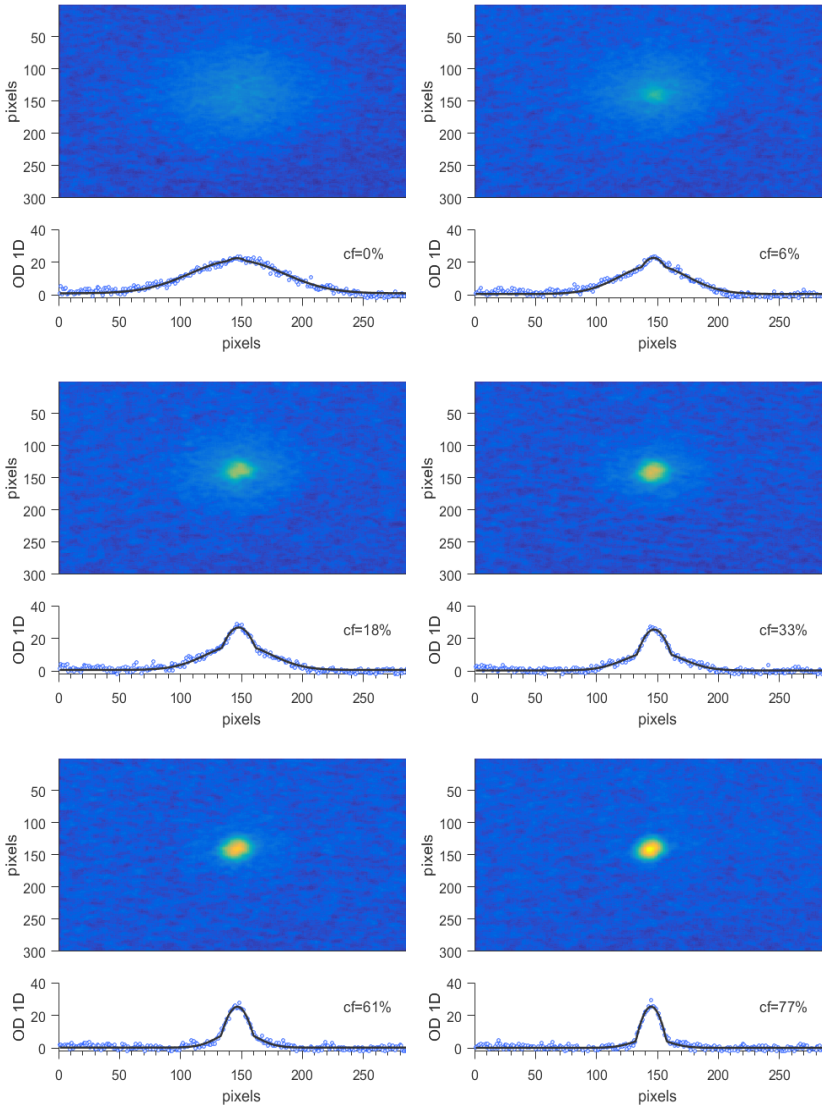

Figure 46: Each figure shows the absorption image, integrated OD signal (blue circles) and fit (black lines), to an atom distribution with a given condensed fraction (cf). A thermal cloud (Gaussian distribution) is shown in the first image and a fully condensed cloud in the last one (Thomas-Fermi distribution). Middle images show the bimodal distribution expected for partially condensed clouds.

7

SPIN STATE PREPARATION AND READOUT

In previous chapters we have studied how to create a condensate with no special attention to the spin state created. In this chapter I will describe the techniques we use to manipulate and create arbitrary spin states, an essential part in the study of spinor condensates.

7.1 SPIN PREPARATION: INCOHERENT POPULATION TRANSFER

7.1.1 *Optical Pumping*

The first step for manipulating the spin state of our atoms is optical pumping: because the forced evaporation procedure is highly insensitive to spin state, we would condense in a full mixed state with the atoms in all the magnetic sublevels $m_F = 1, 0, -1$. We can pump the atoms into a single Zeeman state by illuminating them with an optical pumping beam (OP), this has the effect of reducing the entropy associated with the spin state. The quantization axes is defined by an applied magnetic field $\mathbf{B} = B_y \mathbf{y}$, $B_y = 500\,\text{mG}$, same direction as the propagating of the OP beam (see Figure 49). This beam has σ^+ polarization and is resonant with the $|F = 1\rangle \rightarrow |F' = 1\rangle$ transition. Under multiple absorptions each atom remaining in $|F = 1\rangle$ is pumped into $|F = 1, m_F = 1\rangle$ which is a dark state of the interaction with the optical pumping beam (see Figure 47). Because some atoms can decay into the $|F = 2\rangle$ manifold, we pump them back into $|F = 1\rangle$ simultaneously illuminating the atoms with a beam tuned to the $|F = 2\rangle \rightarrow |F' = 2\rangle$ transition. This beam is delivered via the MOT beams, and create a polarization field which varies rapid in space. Every point in space has a single define polarization but since the atoms move during the pumping process on the scale of such polarization variation, an atom eventually encounter a

Remember the background field is always compensated

region with a proper polarization it can absorb so that an atom in any $|F = 2\rangle$ sublevel can returned to $|F = 1\rangle$.

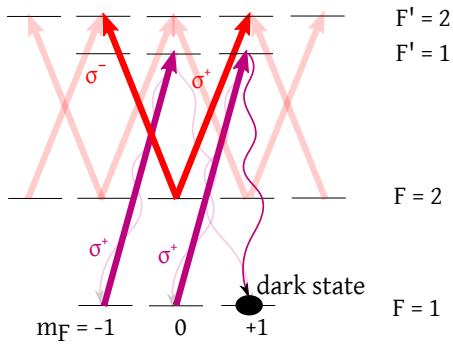

Figure 47: Optical pumping scheme. Violet lines represent the optical pumping beam while the red the depump beam to recover the atoms that fall into $|F = 2\rangle$.

Because this method requires multiple absorption of photons it is unavoidable that the average temperature of the atoms increases due to the multiple recoil kicks, each one providing about 360 nK [Steck, 2001], which is already three times larger than the typical temperature of our condensate. This means we have to optically pump the atoms well before reaching T_c so the increase in temperature is not prejudicial. We do so right after loading ODT1 when the average temperature is 50 µK. The optical pumping procedure consists on sending three pulses of 60 µs duration and separated by 5 ms between each other: We leave this time to avoid shadowing effects. After the third pulse, 90% of the atoms are in $|F = 1, m_F = 1\rangle$ as confirmed by Stern-Gerlach population measurements (see Section 7.3.1).

The setup

The OP beam comes from the zero order of the repumper beam and is frequency shifted by an AOM of center frequency 120 MHz in a double pass cat-eye configuration as shown in Figure 48.

This beam is fiber coupled, and sent to the experiment table where we collimate it to a waist of 0.5 mm (PAF-X-5-B) and ex-

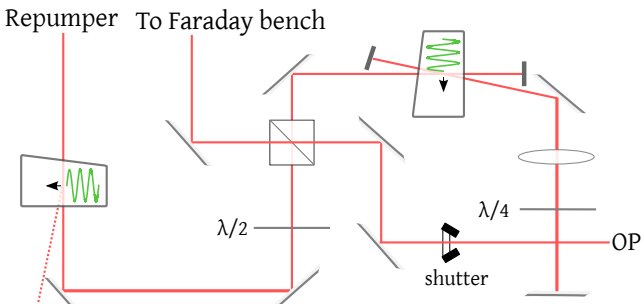

Figure 48: Optical bench for the control of the OP beam.

panded with a 4X telescope. At the atom position it has a size of 2 mm. It crosses ODT1 and ODT2 at nearly 45°, making a small angle with the $B_y\mathbf{y}$ field. After the beam crosses the atoms the transmitted signal is detected with a fast PD with a transimpedance amplifier (1801-FS, New Focus) with 25 MHz bandwidth, 4×10^4 V/A Gain and 3.3×10^{-12} W/Hz$^{1/2}$ NEP. See Figure 49.

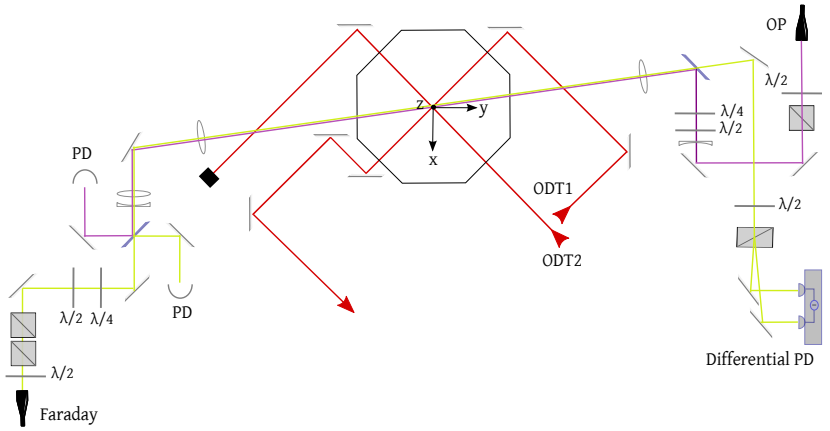

Figure 49: Setup of the optical pumping beam (violet) and the Faraday beam (lime) around the vacuum chamber. The beams polarizations are cleaned with PBS's and controlled by sets of waveplates. The beams are combined with beam splitters as they have the same wavelength. They cross the ODT's at 45° and propagate along $\mathbf{y}$. The axis are defined by the fields generated with the bias coils.

Frequency

To set the absolute frequency of the OP beam we perform spectroscopy in the following way. The atoms are prepared in the $|F = 1\rangle$ state. The OP beam illuminates them at the same time the probe beam resonant with the $|F = 2\rangle \rightarrow |F' = 3\rangle$ does. The OP is used to repump the atoms from the state $|F = 1\rangle$ to $|F = 2\rangle$ so the probe beam can be absorbed, as in absorption imaging. The number of atoms in the state $|F = 2\rangle$ is maximized when the OP is resonant with any transition. The relative frequency of the OP beam with the transition $|F = 1\rangle \rightarrow |F' = 1\rangle$ is plotted in Figure 50. Two peaks appear at the resonances with the $|F = 1\rangle \rightarrow |F' = 1\rangle$ and $|F = 1\rangle \rightarrow |F' = 2\rangle$ transitions, the transition $|F = 1\rangle \rightarrow |F' = 3\rangle$ is forbidden and although $|F = 1\rangle \rightarrow |F' = 0\rangle$ is not, the decay from $|F' = 0\rangle$ to $|F' = 2\rangle$ is. The highest peak corresponds to the resonant pumping on the transition $|F = 1\rangle \rightarrow |F' = 2\rangle$, 157 MHz from the $|F = 1\rangle \rightarrow |F' = 1\rangle$ as expected (see Appendix A).

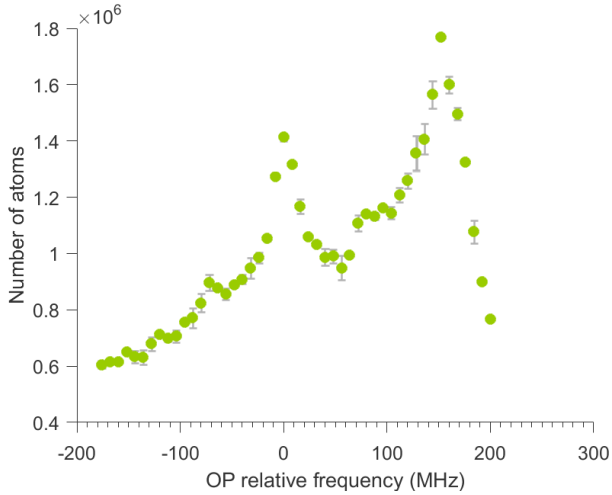

Figure 50: Frequency of optical pumping beam in free space relative to the transition $|F = 1\rangle \rightarrow |F' = 1\rangle$.

Coherence of the state

The optical pumping sequence described above allows us to generate the coherent state $(1, 0, 0)^T$ from a completely mixed state

which describes the atoms after the loading phase. This coherent state is a fully polarized state aligned with the magnetic field and therefore represents all the atoms occupying the state $|m = 1\rangle$ in the quantization axis defined by the magnetic field. The coherence of this state is characterized by the longitudinal relaxation time $\mathcal{T}_1$, this parameter characterizes how the longitudinal magnetization decays in time in an exponential way $\propto \exp\{-t/\mathcal{T}_1\}$. In isolated systems like ours the longitudinal relaxation is expected to be negligible. To estimate $\mathcal{T}_1$, we measure the populations in all the m_F states as a function of time. The value of the relaxation constant is found from an exponential fit to the relative population in $|m_F = 1\rangle$ as a function of time. As can be appreciated in Figure 51, the state doesn't decay in the second scale. From the fit we obtain $\mathcal{T}_1 \simeq \infty$.

Concepts originally developed in the field of nuclear magnetic resonances (NMR).

It is important to notice that the fit is performed on the relative population of $|m_F = 1\rangle$ where we have normalized by the total number of atoms (in all spin states). This ensures we don't confuse atom losses with the relaxation of the spins. For the thermal ensemble we are considering here, atom losses are given only by collisions with the background gas, which defines the lifetime. It has been confirmed $\mathcal{T}_1$ largely exceeds the lifetime of the atoms in our vacuum conditions.

This long coherence of the state allows us to create a condensate with all the atoms in the $|m_F = 1\rangle$ state. Since the magnetization is not affected during the evaporation process, we can polarize the atoms right after loading the trap and evaporate afterwards achieving condensation without altering the polarization state.

A more detailed study of the coherence properties of the system is presented in Chapter 8.

7.1.2 *Bell-Bloom excitation*

In 1961 Bell and Bloom invented a way to observe spin polarization rotation around an orthogonal magnetic field inducing such by stroboscopically pumping the atoms with pulses of light at frequencies matching the Larmor frequency. [Bell and Bloom,

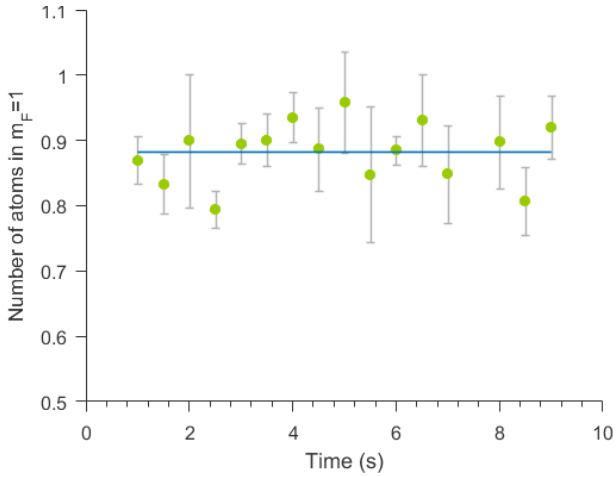

Figure 51: Relative population in $m_F = 1$ as a function of time showing the longitudinal magnetization is constant in the second scale. Measurements performed spatially separating the different spin components as described in Section 7.3.1.

1961] The effect can be observed when applying many short pulses (compared to the Larmor period) of circularly polarized light propagating orthogonal to a magnetic field bias. Any probing at frequency other than the Larmor frequency would result in polarization and depolarization, since the pumping is always along the propagation of the optical pumping beam. The developed polarization, revealed by the transmission of the optical pumping pulses, as a function of the probing period shows a Lorentzian shape centered at the period equal to the period of the Larmor precession. The transmission is maximum when the atoms are all occupying a dark state as shown in Figure 47 and the beam is not absorbed anymore. The polarized atomic state that is created is orthogonal to the magnetic field.

Applying a magnetic field $\mathbf{B} = B_z\mathbf{z}$ such that the Larmor frequency is $\nu_L = g_F\mu_B B_z/h = 100\,\text{kHz}$, a series of $10\,\mu\text{s}$ pulses at frequency $\nu_{BB} = \nu_L$ is sent to the atoms and the transmission recorded with the PD. An example is shown in Figure 52 where we can see the absorption is diminished with each pulse until

the transmission is maximum, indicating efficient pumping into an orthogonal state.

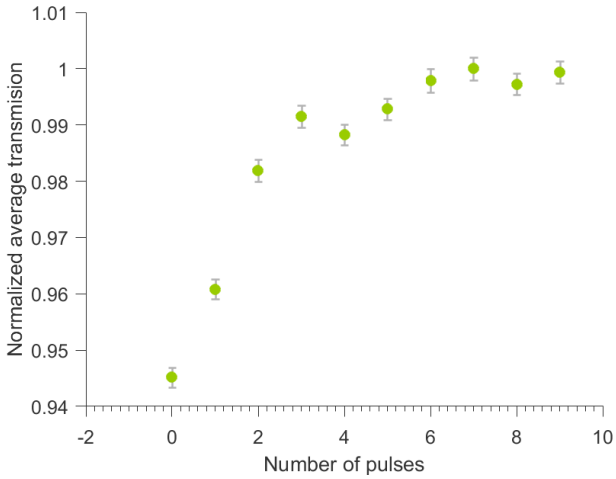

Figure 52: Relative transmission of the Bell-Bloom excitation pulses as a function of the number of pulses. The pulses are 1 µs long and sent at a frequency $\nu_{BB} = 100\,\text{kHz}$ which match the Larmor frequency ν_L of the atoms precessing around the magnetic field. The saturation indicates the atoms are optically pumped into a dark state where can not absorb more photons.

In order to match ν_{BB} and ν_L we send trains of pulses at the chosen rate $\nu_{BB} = 100\,\text{kHz}$ for different values of the field strength and therefore ν_L. We plot the difference between the last and the first pulse transmission as a function of ν_L. A Lorentzian distribution is expected on the transmission with peak at $\nu_L = n\nu_{BB}$ for any natural number n [Bell and Bloom, 1961]. As shown in Figure 53 we observe three peaks: $\nu_L = \nu_{BB}, 2\nu_{BB}$ and 0. At zero field the atoms do not rotate therefore no depolarization by unmatched probing occur.

Because this pumping technique requires multiple absorptions, it can not be implemented to pump atoms with temperatures close to the recoil temperature if significant heating is undesired. A Bell-Bloom polarization sequence is always therefore implemented in early stages of the evaporation. In addition, a state

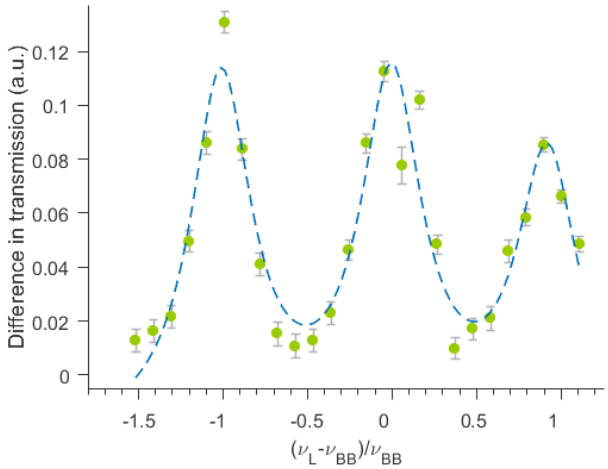

Figure 53: Transmission after multiple Bell-Bloom excitation pulses at frequency ν_{BB} as a function of the Larmor frequency ν_L referred to ν_{BB}. Peaks show efficient pumping into a dark state when both frequencies obey $\nu_L = n\nu_{BB}$ for any natural n.

with transverse polarization has a decay time of a few hundreds of ms, in contrast to a longitudinally polarized state. These conditions make the technique suitable for polarizing thermal atoms but not generate condensates with orthogonal polarization. For creating arbitrary spin states of the condensate, nevertheless, we employ coherent techniques based on radio or micro-wave frequency driven transitions. We detail those in the next section.

7.2 SPIN PREPARATION: COHERENT TRANSFER

7.2.1 *RF rotations*

Rotations are produced by a bias field together with an orthogonal resonant RF field. We typically use them to generate polarization states than can be related to a π or a $\pi/2$ rotation of the state $(1,0,0)^T$ produced by optical pumping. For example, a π pulse takes the state $(1,0,0)^T$ to $(0,0,1)^T$, the opposite stretched state in the same basis. A $\pi/2$-pulse on the other hand, transfer

the atoms into a stretched state transversally magnetized to the bias field $\left(1/2, 1/\sqrt{2}, 1/2\right)^T$.

The preparation state is done as follows. We first optically pump the atoms along $\mathbf{y}$ in $m_F = 1$ and proceed to adiabatically ramp down $B_y\mathbf{y}$ and up $B_x\mathbf{x}$. The atoms follow the field and end up pointing along $\mathbf{x}$, this changes the quantization axes to the $\mathbf{x}$ direction. Then we send two 100 µs pulses of RF radiation $\mathbf{B}_{RF} = B_{RF}\mathbf{z}$ at 200 kHz (40 cycles in total), maximizing the transfer of the population into $m_F = -1$ adjusting the final value of B_x. From a classical point of view, a torque is induced on the magnetization $\mathbf{M}$ by the total field $\mathbf{B}_T = \mathbf{B}_x + \mathbf{B}_{RF}$, such that $d\mathbf{M}/dt = \gamma\mathbf{M} \times \mathbf{B}_T$ [Hahn, 1950]. As can be seen in Figure 54, deviations from the frequency of B_{RF} of 0.5% greatly reduce the efficiency of a π-pulse to 70%.

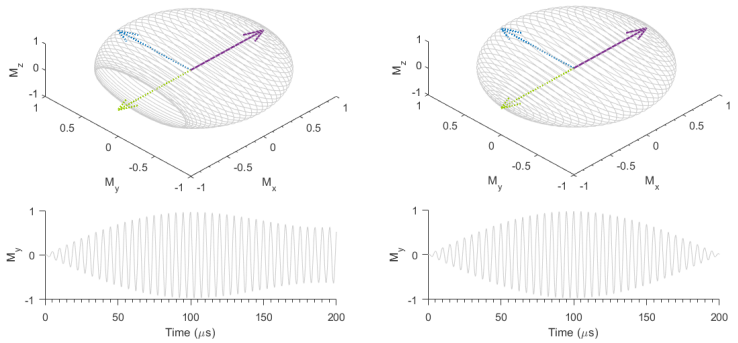

Figure 54: Classical view of spin rotations under the interaction with a bias field along $\mathbf{x}$ and a perpendicular RF field oscillating, in the first case, 0.5% off from the Larmor frequency and, in the second, at exactly the Larmor frequency. Violet: initial magnetization. Blue: magnetization after $\pi/2$-pulse. Green: magnetization after π-pulse.

Fine adjustment is done sending only one 100 µs pulse. The strength of the RF field is adjusted to prepare the state $\left(1/2, 1/\sqrt{2}, 1/2\right)^T$ by matching the populations to be 1/4, 1/2, 1/4 revealed by Stern-Gerlach imaging.

Good reproducibility of the state preparation requires synchronization of the RF pulses with the same point in the cycle of mains. Mains are the principal cause of magnetic field fluctuations which reach an amplitude of 10% around the mean across one cycle of mains. Recalibration of the bias fields is performed every day to account for .

7.2.2 *RF adiabatic sweep*

In order to transfer in a less sensitive way atoms from one stretched state to another or even transform a stretched state to a state that can not be obtained by a rotation in spin space from the original, one may use RF adiabatic sweeps. [Vitanov et al., 2001]

Lets consider the case of a spin pointing in **z** direction in the presence of a linear and quadratic Zeeman shift. The single atom Hamiltonian is: (see Chapter 3)

$$\hat{H}_{Zl} + \hat{H}_{Zq} = g_F \mu_B B_z \hat{F}_z + \frac{(g_F \mu_B)^2}{E_{hf}} B_z^2 \hat{F}_z^2 \tag{84}$$

The presence of an RF field in the perpendicular direction **y** , contributes as:

$$\hat{H}_{RF} = g_F \mu_B B_y \cos(\omega_R t) \hat{F}_y \tag{85}$$

where B_y is the peak amplitude of the RF field oscillating at ω_R.

We define the Larmor frequency $\omega_L = -g_F \mu_B B_z/\hbar$ and the quadratic frequency: $\omega_q = (g_F \mu_B B_z)^2/(\hbar E_{hf})$. $E_{hf}/h \simeq +6.8\,\mathrm{GHz}$ and $g_F = -0.5$ for ^{87}Rb in $|F = 1\rangle$. It is convenient to transform the total Hamiltonian $\hat{H}_T = \hat{H}_{Zl} + \hat{H}_{Zq} + \hat{H}_{RF}$ to a frame rotating at frequency ω_F, for this, we then apply the transformation: $\mathcal{U} = \exp\{i\omega_F t \hat{F}_z\}$. Notice that we can expand the transformation $\mathcal{U}$ in the Taylor series and get the expression:

$$\mathcal{U} = e^{i\omega_F t \hat{F}_z} = \mathbb{1} + i \sin(\omega_F t) \hat{F}_z + [\cos(\omega_F t) - 1] \hat{F}_z^2, \tag{86}$$

where we have used the fact that, for $F = 1$ and integer k, $\hat{F}_z^{2k} = \hat{F}_z^2$ and $\hat{F}_z^{2k+1} = \hat{F}_z$. Notice that the transformation leaves $\hat{F}_z$ invariant: $\mathcal{U}^\dagger \hat{F}_z \mathcal{U} = \hat{F}_z$ and that $\hat{F}_\pm$ transform according to $\mathcal{U}^\dagger \hat{F}_\pm \mathcal{U} =$

$\hat{F}_\pm e^{\pm i\omega_F t}$. Because this transformation is time dependent the Hamiltonian transforms as:

$$\begin{aligned}\widetilde{H} =& U^\dagger \hat{H}_T U - i\hbar U^\dagger \frac{\partial U}{\partial t}, && (87)\\ =& \hat{H}_{Zl} + \hat{H}_{Zq} + U^\dagger \hat{H}_{RF} U - i\hbar U^\dagger \frac{\partial U}{\partial t}, && (88)\end{aligned}$$

because $\hat{H}_{Zl}$ and $\hat{H}_{Zq}$ commute with $\hat{F}_z$. The last term is:

$$-i\hbar U^\dagger \partial U/\partial t = \hbar\omega_F \hat{F}_z, \tag{89}$$

whereas the transformation of $\hat{H}_{RF}$ is:

$$\begin{aligned}U^\dagger \hat{H}_{RF} U =& g_F \mu_B B_y \cos(\omega_R t)\frac{1}{2i}[e^{i\omega_F t}\hat{F}_+ - e^{-i\omega_F t}\hat{F}_-]\\ =& g_F \mu_B B_y \frac{1}{4i}[e^{i\omega_R t} + e^{-i\omega_R t}][e^{i\omega_F t}\hat{F}_+ - e^{-i\omega_F t}\hat{F}_-].\end{aligned} \tag{90}$$

Because last expression contains fast and slow rotating terms we make the rotating wave approximation (RWA) dropping the terms oscillating at $|\omega_F + \omega_R|$ and get:

$$(U^\dagger \hat{H}_{RF} U)_{RWA} \simeq g_F \mu_B B_y \frac{1}{4i}[-e^{i(\omega_R-\omega_F)t}\hat{F}_- + e^{i(\omega_F-\omega_R)t}\hat{F}_+]. \tag{91}$$

Combining previous expressions we can write the Hamiltonian in the rotating frame oscillating in the RWA:

$$\begin{aligned}\widetilde{H}_{RWA} =& -\hbar\omega_L \hat{F}_z + \hbar\omega_q \hat{F}_z^2 + \hbar\omega_F \hat{F}_z\\ &+ g_F \mu_B B_y \frac{1}{4i}[e^{i(\omega_F-\omega_R)t}\hat{F}_+ - e^{i(\omega_R-\omega_F)t}\hat{F}_-],\\ =& \hbar(\omega_F - \omega_L)\hat{F}_z + \hbar\omega_q \hat{F}_z^2 - \hbar\Omega\frac{1}{4i}[e^{-i\Delta t}\hat{F}_+ - e^{i\Delta t}\hat{F}_-],\end{aligned} \tag{92}$$

where we have defined $\Delta = \omega_R - \omega_F$ and the Rabi frequency $\Omega = -g_F \mu_B B_y/\hbar$. It is particularly useful to choose a rotating frame oscillating at ω_R, in this case $\Delta = 0$ so the Hamiltonian is time independent in the simplified form:

$$\widetilde{H}_{RWA} = \hbar\delta\hat{F}_z + \hbar\omega_q\hat{F}_z^2 - \hbar\Omega\frac{1}{2}\hat{F}_y, \tag{93}$$

for $\delta = \omega_F - \omega_L = \omega_R - \omega_L$, acquiring the matrix form:

$$\widetilde{H}_{RWA} = \hbar\begin{pmatrix} \delta + \omega_q & i\frac{\Omega}{2\sqrt{2}} & 0 \\ -i\frac{\Omega}{2\sqrt{2}} & 0 & i\frac{\Omega}{2\sqrt{2}} \\ 0 & -i\frac{\Omega}{2\sqrt{2}} & \omega_q - \delta \end{pmatrix}. \tag{94}$$

In order to visualize the sweep we find the eigenvalues of Equation 94 as a function of the detuning δ. For the most used state preparation from $m_F = 1$ to $m_F = -1$, we apply a low magnetic field bias $B_z \simeq 300\,\text{mG}$ and $B_y = 10\,\text{mG}$. The energy spectrum is shown in Figure 55, adiabatically sweeping the frequency in a 100 kHz range allows us in this scheme to transfer the population between $m_F = \pm 1$ states. The sweep time is typically 10 ms, enough time to guaranty adiabaticity as we will see.

For a complete transfer of the population, this technique is more robust than the RF pulses we described in previous section as it is more insensitive to laser intensity, detuning and interaction time or offset field variations. What is more, this technique is more powerful allowing the possibility to prepare states that can not be related by a rotation from the original state. Tailoring the sweep times for the different ranges of the detuning one can change transition probability between two crossing states. Such probability is approximately well described by the Landau-Zener-Formel formula:

$$P = 1 - \exp\{-\pi\Omega(t_0)^2/2|\dot{\delta}(t_0)|\}, \tag{95}$$

where the change rate of the detuning $\dot{\delta}$, is evaluated at time t_0 as well as the Rabi frequency [Vitanov et al., 2001]. To illustrate this scheme we obtain the energy spectrum for a high bias field

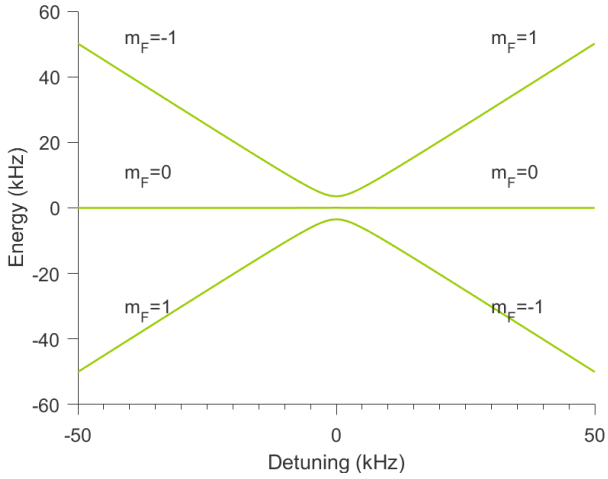

Figure 55: Energy spectrum of Hamiltonian Equation 94 with a bias field of 300 mG. We use this scheme to transfer atoms from $m_F = 1$ to $m_F = -1$.

$B_z = 5\,G$ and $B_y = 10\,mG$ (shown in Figure 56). In this spectrum we distinguish the three expected avoiding crossing points at $\delta = \pm\omega_q, 0$. Using Equation 95 we find that a sweep time of 1 ms over the hole range is enough to guaranty the full transfer of population to the $m_F = -1$ state.

For creating the state $\left(0, 1/\sqrt{2}, 1/\sqrt{2}\right)^T$ starting at $(1,0,0)^T$, for example, one has to split the sweep range into two parts, first a fast sweep of 12 µs of the range −50 kHz to ω_q. This results in the transfer from state $m_F = 1$ to $m_F = 0$ with probability of 0.5. This is followed by a second slow sweep (hundreds of ms) on the range 0 kHz to 50 kHz to guarantee adiabaticity. This resulting in the final state with populations 0, 1/2, 1/2. For other examples of different state preparation see [Erhard, 2004].

7.2.3 *Microwave transitions*

Exploiting the linear Zeeman splitting caused by the presence of a magnetic field one can selectively address transitions between two magnetic levels belonging to different hyperfine manifolds

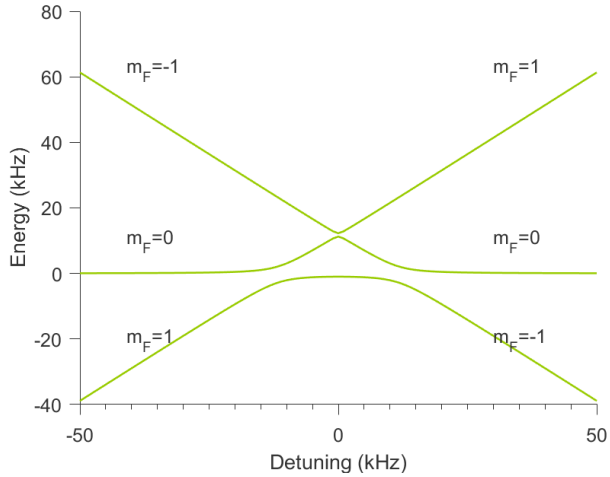

Figure 56: Energy spectrum of Hamiltonian Equation 94 with $B_z = 5\,G$ and $B_y = 10\,mG$ showing the strong bending of the energy levels, which offers the possibility to transfer population between consecutive magnetic sublevels by tailoring the RF frequency and sweep time.

$|F = 1\rangle$ and $|F = 2\rangle$. This is achieved by tuning to resonance a Microwave (MW) radiation (around 6.83 GHz) with the appropriate polarization as can be seen in Figure 57.

An alternative to the RF sweep described in previous section to transfer all the population from $m_F = 1$ to $m_F = -1$, is to use two π-pulses in the MW transitions shown in yellow in Figure 57. More interesting is the possibility to generate the state $(0, 1, 0)^T$ departing from $(1, 0, 0)^T$, which is impossible by means of a rotation. The procedure is as follows. A magnetic field is applied to separate consecutive magnetic levels by $\Delta_{Zl} = 200\,kHz$. Then, a π-pulse of resonant MW radiation with σ^+ polarization is sent to transfer all the atoms to $|F = 2, m_F = 0\rangle$ (see blue I bullet in Figure 57), followed by another π- pulse of MW with π polarization to transfer the atoms to $|F = 1, m_F = 0\rangle$. The interaction time to produce a π-pulse is found from the oscillation period of the Rabi oscillations between the states of interest. An example is shown in Figure 58.

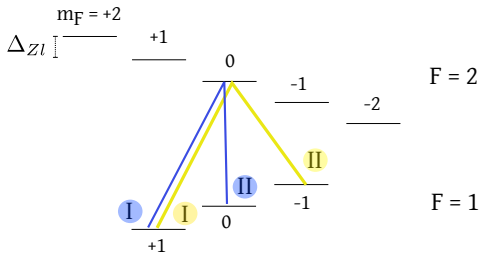

Figure 57: Hyperfine transitions driven by microwave field in the ground state of ^{87}Rb .

The resonant frequencies for each transition are found by scanning the MW frequency at a given magnetic field and fitting a Lorentzian to the transferred population as a function of detuning.

The MW source is a microwave horn antenna with linear polarization but oriented to an elevation of about 45° respect to the atoms, this has the consequence that the radiation has nonzero

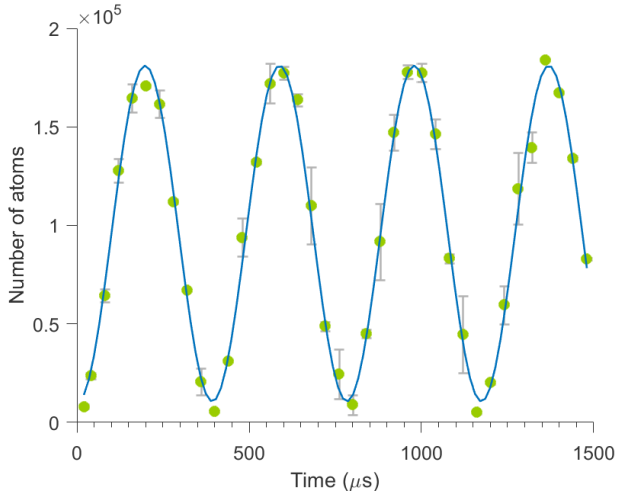

Figure 58: Population in $|F = 2, m_F = 0\rangle$ in the presence of MW radiation showing Rabi oscillations between the states $|F = 1, m_F = 0\rangle \leftrightarrow |F = 2, m_F = 0\rangle$.

overlap with the σ^+, σ^- and π polarization for quantization axis along **x** , **y** and **z** .

7.3 READ-OUT TECHNIQUES

7.3.1 *Stern-Gerlach imaging*

This imaging technique combines the dependence on the direction of the force a magnetic gradient exerts on an atom according toits angular momentum, with standard absorption imaging. Under free falling and in presence of a magnetic gradient dB/dr, atoms in consecutive Zeeman states separate in space a relative distance $x(t) = 1/2(f/M)t^2$ with $f = g_F \mu_B m_F dB/dr$. When this displacement is larger that the thermal expansion of the atoms, the different Zemann states can be imaged independently. For a typical gradient of 20 G/cm and time of flight of 20 ms the separation is 1.3 mm and because the atoms expand as $R_{TH} \simeq k_B T/Mt^2$ (see Equation 66) we can conclude atoms with temperatures above 2 µK can not be spatially distinguished unequivocally. In our experiment, we release a condensate from the ODT and apply a typically gradient field of 13 G/cm generated with the MOT coils during 15 ms. At the same time, we apply a bias field of 0.5 G along a chosen direction to define the quantization axis. It is important to avoid zero crossing points at the atoms position, as they may induce Majorana transitions that in an optical trap do not represent losses but can induce Zeeman relaxation [Stamper-Kurn and Ueda, 2013].

An example of Stern-Gerlach images is shown in Figure 59. A state prepared in $(1,0,0)^T$ is rotated due to an applied orthogonal RF magnetic field. The initial state followed by consecutive $\pi/2$ pulses rotate to the states $\left(1/2, 1/\sqrt{2}, 1/2\right)^T$, $(0,0,1)^T$, $\left(1/2, 1/\sqrt{2}, 1/2\right)^T$ and back to $(1,0,0)^T$.

Another example showing Rabi oscillations between the $|F = 1, m_F = 1\rangle \leftrightarrow |F = 2, m_F = 0\rangle$ states is presented in Figure 60 A microwave field drives the transitions .

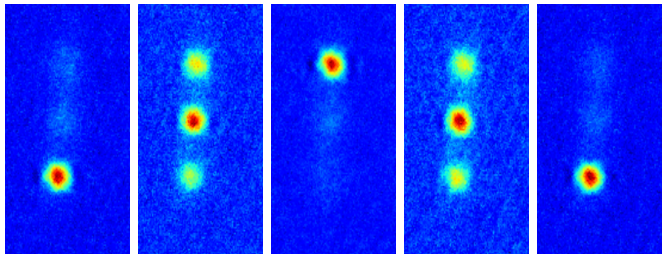

Figure 59: Stern-Gerlach images that show the evolution of the state $(1,0,0)^T$(first from the left) in the presence of an orthogonal RF field. The second image shows the state $\left(1/2, 1/\sqrt{2}, 1/2\right)^T$ generated after a $\pi/2$ pulse. The next image corresponds to a π pulse, the next to a $3\pi/2$ pulse and finally the last state is the original after a full rotation 2π.

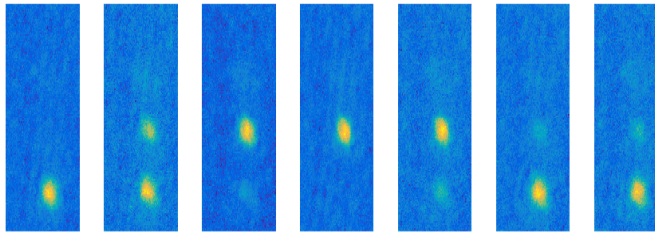

Figure 60: Stern-Gerlach measurement showing Rabi Oscillations between $|F = 1, m_F = 1\rangle \leftrightarrow |F = 2, m_F = 0\rangle$ states.

This bias field is not always present during the experiment and is ramped up with the gradient itself. This bias field defines the basis of the SG measurement, which could in principle be different than the bias field present prior to the start of the SG measurement. In the last case, the switching has to be non-adiabatic, otherwise the spin state will follow the bias pointing direction. Adiabaticity is ensured when the change rate of the bias is much lower than the Larmor frequency. Lets' take the scenario where the atoms originally point along $\mathbf{y}$ and a small bias B_y is present. We desire to project onto the $\mathbf{z}$ axis for which we ramp up the field in a time t_f to $B_z(t_f) = 0.5\,G$:

$$
\begin{aligned}
\frac{1}{|B(t)|}\frac{d|B(t)|}{dt} &> g_F|B(t)| \\
\frac{d}{dt}\left(\sqrt{B_y^2 + B_z(t)^2}\right) &> g_F|B(t)|^2 \\
\frac{B_z(t)}{|B(t)|}\frac{dB_z(t)}{dt} &> g_F|B(t)|^2 \\
\frac{[B_z(t_f)]^2 t}{t_f^2} &> g_F|B(t)|^3 \text{assuming } B_z(t) = \frac{B_z(t_f)}{t_f}t \\
t_f &< \frac{[B_z(t_f)]^2}{g_F|B(t_f)|^3} \text{ at } t = t_f
\end{aligned} \tag{96}
$$

in this scenario the above relation implies the change in the bias has to be done in less than 3 µs in order to be non-adiabatic, which is impossible for our coil driver. To guarantee we are projective in the quantization axis **z** a bias on this direction has to be set during the experiment.

7.3.2 *Faraday rotation measurements*

The most useful tool we have for characterizing the spin state of the atoms is Faraday probing, which is not only sensitive to the populations like the Stern-Gerlach technique, but also can reveal the coherence between states. As we have detailed in Chapter 2 the interaction $\hat{H}_F \propto \hat{S}_z\hat{F}_z$ gives rise to a rotation of the polarization of the probing beam around the axis **z** which is proportional to the total spin component along such an axis. In the following sections we describe the experimental setup and the calibration of the atom-light interaction for this technique.

The setup

The Faraday beam is taken from the zero order of the repump beam and frequency shifted by a 80 MHz AOM in double pass cat-eye configuration. After this is coupled into a pm fiber we send it and collimate it on the experiment table to a waist 2 mm (PAF-X-18-B, Thorlabs). We split the beam in a 50/50 splitter, one to the monitor PD and the other to a telescope 2X before

focusing it into the atoms with a 300 mm focal length lens. The estimated waist at the atoms is 18 µm. Good quality of the polarization of this beam is essential, to guarantee a linear state of polarization we set two consecutive polarization beam splitters at the output of the collimator. To generate arbitrary states of polarization at the atom position only one half and one quarter wave plates are needed (since the input state is always linear). The layout is shown in Figure 49, where it can be appreciated that the beams OP and Faraday overlap inside the chamber. The beams are combined in a 50/50 beam splitter at the input side of the Faraday and with a 70/30 beam splitter at the output. After traversing the atoms the Faraday beam enters a polarimeter, this is described in the next section.

Polarimeter

The polarimeter was designed to detect the difference in the number of photons in the diagonal basis $\{|D\rangle, |A\rangle\}$, and therefore sensitive to the stokes parameter $\hat{S}_y$. As shown in Figure 61, it consists on a half-wave plate to rotate the polarization to the basis $\{|H\rangle, |V\rangle\}$, followed by a Wollaston prism that separates both polarization components. Those components are detected on a differential detector that outputs a voltage proportional to the difference in the number of photons.

$|D\rangle(|A\rangle)$ *is polarized at* $+(-)45^o$ *with respect to* $|H\rangle$.

The performance and design of the differential photodetector we use is extensively explained in [Ciurana et al., 2016]. It consists of a pair of high quantum efficiency photodiodes (S3883, Hamamatsu) connected in series. The difference of the photocurrents from the photodiodes is coupled to an integrator that utilizes a charge-coupled amplifier (CR-110, CREMAT), a capacitor and a discharge resistor. The signal exhibits a discharge behaviour characteristic of an integrator with a relaxation time constant of 110 µs. The rise time of the photodetector is 50 ns.

As compared to the 290 µs *of the original design.*

A pulse short compared to the relaxation time of the differential detector generates a signal proportional to the difference in the number of photons that we call N_{diff}. Such a pulse defines ΔV (see green line in Figure 62) the conversion factor is $N_{diff} = C_y \Delta V$ where $C_y = -6.075 \times 10^5\ V^{-1}$.

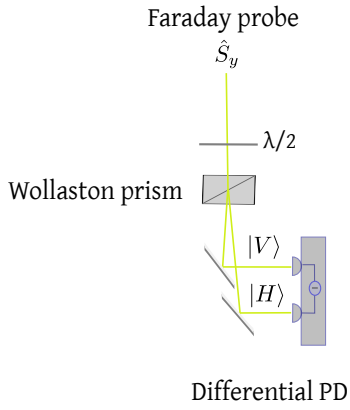

Figure 61: Shot-noise limited polarimeter for the detection of the Stokes parameter $\hat{S}_y$.

The total number of photons entering the polarimeter N_L is estimated from the signal of a photodiode with a trasimpedance amplifier that monitors the power of the Faraday probe (violet signal in Figure 62). The mean value of the monitor signal $\langle V_x \rangle$ is related to N_L through:

$$N_L = \frac{\lambda}{hc} T c_x \langle V_x \rangle \tau_p \equiv C_x \langle V_x \rangle \tau_p \tag{97}$$

where λ is the wavelength of the probe beam, τ_p the pulse duration, $c_x = 2.35 \times 10^{-4}\,\mathrm{W/V}$ and T the relative transmission to the polarimeter path, where we typically include attenuating filters such that $T = 7 \times 10^{-3}$. This values together define $C_x = 6.46 \times 10^{12}\,(\mathrm{Vs})^{-1}$.

In a more general case when the probing state is evolving in time and so the Stokes operators, the signal of the polarimeter is given by:

$$V(t) = \frac{1}{C_y} \int_0^t \frac{\hat{S}_y(t')}{t'} dt' \tag{98}$$

Consider the case of an ensemble of atoms orthogonally polarized to the bias field ($B_z \mathbf{z}$) and therefore rotating around it

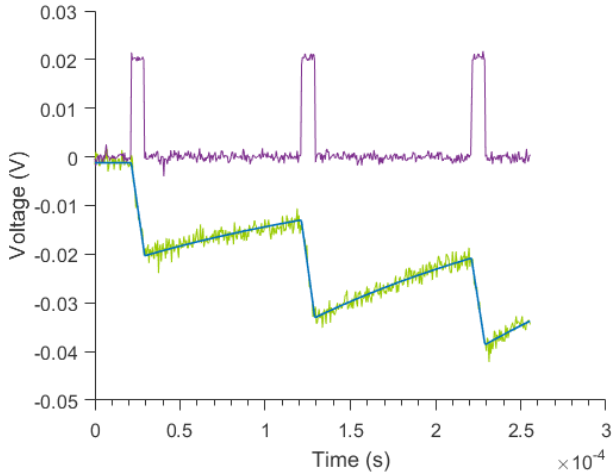

Figure 62: Violet: monitor signal (V). Green: differential photodetector signal (V). Blue: fit function of a rising voltage during pulses followed by a discharge of the integrator.

at the Larmor frequency. Probing the ensemble during a time longer that the period of the Larmor oscillation results in $\hat{S}_y^o \propto \sin\theta(t)$ and therefore a signal on the polarimeter which is $V(t) \propto \int \sin\theta(t')dt'$, like that shown in Figure 63. The amplitude of the signal is therefore proportional to $1/\omega_L$ but not the noise. In consequence, slower signals exhibit better signal to noise ratios.

Noise

We model the noise of the detector with the known relation:

$$\text{var}\,(N_{diff}) = n_{L0}N_L^0 + n_{L1}N_L + n_{L2}N_L^2. \tag{99}$$

The first therm n_{L0} represents the electronic noise. The second term is the shot noise (SN) contribution that for a coherent state is $\text{var}\left(N_L'\right) = N_L'$. The coefficient n_{L1} accounts for the non ideal quantum efficiency of the detector. The third term is the technical noise. By studying the scaling of the noise of the signal as a function N_L, we have demonstrated the differential photodetector is shot-noise limited in the interval $(0.2 - 10) \times 10^6$

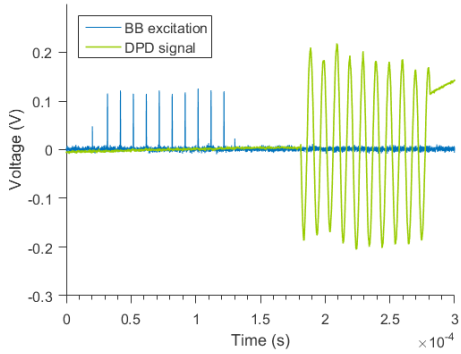

Figure 63: Bell-Bloom pulses at rate matching the Larmor precession of the atoms (blue) and therefore preparing the atoms in a polarized state orthogonal to the applied magnetic field. Green: differential detector signal showing the precession of the atoms at the Larmor frequency.

photons. To perform this characterization we send to the differential detector fifty independent pulses each one with number of photons N_L and measure $\Delta V(N_L, \mathrm{repeat})$ for each pulse. We compute the variance of the fifty $\mathrm{var}(\Delta V(N_L))$ and repeat the same for a different number of photons. The signal of the polarimeter and the monitor are acquired by a system with FPGA and CPU (STEMLAB 125-14, redpitaya) with a sampling rate of 125 MS/s, analogue-to-digital converted (ADC) resolution of 14 bit and a memory depth of 16 kS when synchronizing acquisition to an external trigger.

Using the conversion factor C_y to express ΔV as N_{diff}, we plot $\mathrm{var}(N_{diff})$ as a function of N_L (see Figure 64). A fit function of the form Equation 99 shows the differential photodetector has electronic noise $n_{L0} = 2.4 \pm 0.6 \times 10^5$ and a quantum efficiency defining $n_{L1} = 1.17 \pm 0.04$. The technical noise on the scale of the measurement is negligible, we found it to be $n_{L2} N_L^2 = 2 \pm 4 \times 10^{-9} N_L^2$.

Coupling constant calibration

In Section 2.4 we have detailed the interaction between a Faraday probe and a polarized state and found that the outcome for $\hat{S}_y$ is

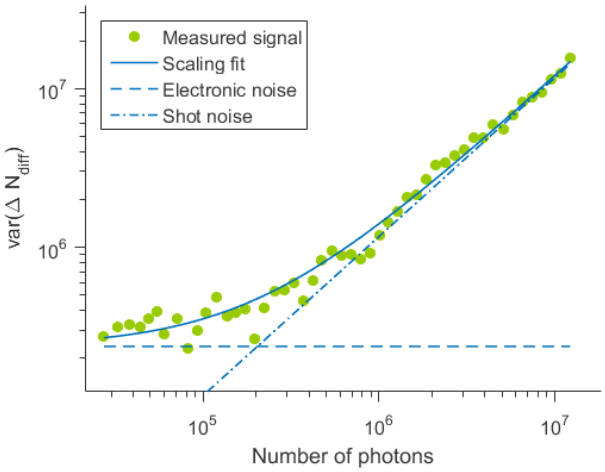

Figure 64: Noise scaling of the differential detector signal N_{diff}. The linear trend demonstrates it is shot-noise limited in the range $(0.2 - 10) \times 10^6$ photons. Electronic noise is $n_{L0} = 2.4 \pm 0.6 \times 10^5$, and the technical noise $2 \pm 4 \times 10^{-9} N_L^2$.

given by $\hat{S}_y^o = \hat{S}_x^i \sin(\theta) + \hat{S}_y^i \cos(\theta)$, where here we have noted with super-index i the initial state and o for the output state. We noticed than in the case where the Faraday rotation angle $\theta << 1$ the output simplifies to $\hat{S}_y^o = \hat{S}_x^i \theta + \hat{S}_y^o \equiv \hat{S}_x^i G_1 \hat{F}_z + \hat{S}_y^i$. The coupling constant G_1 characterizes the interaction strength defined by the vectorial polarizability and the spatial mode match of the probing beam and the atomic distribution. We experimentally measure G_1 in the following way: the polarization state of the probing beam is prepared such that $\langle \hat{S}_y^i \rangle = \langle \hat{S}_z^i \rangle = 0, \langle \hat{S}_x^i \rangle = N_L/2$ whereas the atomic state is prepared such that $\langle \hat{F}_z \rangle = N$, this is, all the atoms are pumped into $|F = 1, m_F = 1\rangle$. We probe the state with short pulses (20 us) so the relaxation of the differential photodiode do not disturb the measurement. For the given initial conditions we can write the output of the polarimeter to be $\langle \hat{S}_y^o \rangle = \langle \hat{S}_x^i \rangle G_1 N$. So we plot $\langle \hat{S}_y^o \rangle / \langle \hat{S}_x^i \rangle$ as a function of N and fit a linear trend. The slope is G_1. The number of atoms is measured with absorption imaging. The detuning of the Faraday probe is $\Delta = 276\,\text{MHz}$ from the $|F = 1\rangle \rightarrow |F' = 0\rangle$ transition.

As we said before, G_1 depends on the geometrical coupling between the atoms and the probe beam, for which we calibrate G_1 at different points of the evaporation. The results are plotted in Figure 65. The pure condensate is formed after 4.8 s of forced evaporation, at this point the coupling is maximum with a value of $G_1(t_{evap} = 4.8\,s) = 10^{-7}$ rad/atoms.

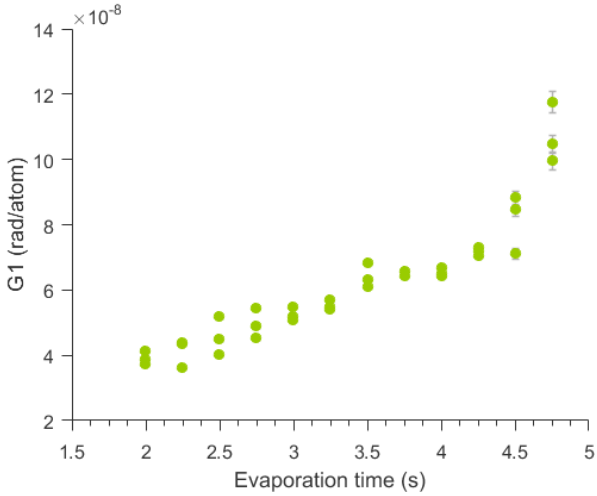

Figure 65: Estimated coupling constant G_1 at different stages of the evaporation. The increment as a function of evaporation time indicates the geometrical coupling is better for smaller clouds. A pure condensate is formed after 4.8 s of evaporation.

It is interesting to estimate the sensitivity of the Faraday probing considering a coherent state has a limitation in the angular resolution given by $\Delta\theta' = 1/\sqrt{N_L'}$. For the rotation angle θ defined as:

$$\theta \equiv \frac{\hat{S}_y^o}{\hat{S}_x^i}, \tag{100}$$

and following from the above results, we can write the spin resolution as given by: [Koschorreck, 2010]

$$\Delta N_s = \frac{\Delta\theta}{G_1} = \frac{1}{\sqrt{N_L}G_1}. \tag{101}$$

In the pure condensate with 10^5 atoms using 1.2×10^6 photons, we estimate to have a resolution of 10^4 spins. It is natural to think on using a larger number of photons when considering Equation 101, to increase the spin resolution. Nevertheless, probing of the atomic state leads to depolarization induced by the interaction itself. The rate of depolarization is in good approximation proportional to the number of photons [Koschorreck, 2010]. We can write then:

$$\langle \hat{F}_z^o \rangle = \langle \hat{F}_z^i \rangle exp(-\gamma_L N_L) \tag{102}$$

where γ_L quantifies the induced depolarization per photon.

From the magnetization as a function of the number of photons in the probing pulse, we find $\gamma_L = 2.15 \times 10^{-8}$. For our typical conditions probing with 1.2×10^6 photons the induced damage is 2%. Increasing the number of photons by a factor of ten results in an induce depolarization of 20% with only a factor of 3 gain in the spin resolution.

Faraday rotation angle calibration

The conversion factor of the angle θ is found by recording the output signal of the polarimeter as a function of the angle of the input polarization when there are no atoms present. The angle is set by rotating the waveplate at the input of the polarimeter such that the angle between the initial polarization and the axis of the waveplate is α. The rotation to the polarization of the light is therefore 2α from the original axis. The Faraday rotation angle is defined by θ in the Poincaré sphere. A rotation β on this sphere corresponds to a rotation of $\beta/2$ in coordinate space. Therefore, the rotated polarization is a rotation by 4α from the original state in the Poincaré sphere. We found the relationship:

$$\theta(\text{rad}) = C_\theta \frac{\Delta V}{\langle V_x \rangle \tau_p} \tag{103}$$

with $C_\theta = -9.4 \times 10^{-8}$ s.

Detuning

To set the detuning of the Faraday beam we first perform spectroscopy to find the resonance frequency with the $|F = 1\rangle \rightarrow |F' = 0\rangle$ transition. We do that in two possible ways, the first one following the strategy described for the OP beam (see Figure 50). The second is inducing atoms losses when resonant with the different transitions: we prepare the atoms in the state $|F = 1\rangle$ and evaporate to 0.5 µK. We then illuminate the atoms with the probe beam resonant with the $|F = 2\rangle \rightarrow |F' = 3\rangle$ transition as well as with the Faraday probe during 40 µs. When the Faraday beam is resonant multiple photon absorptions occur and consequently atom losses are observed. Figure 66 shows three peaks of losses corresponding to the transitions $|F = 2\rangle \rightarrow |F' = 0, 1, 2\rangle$ from left to right respectively.

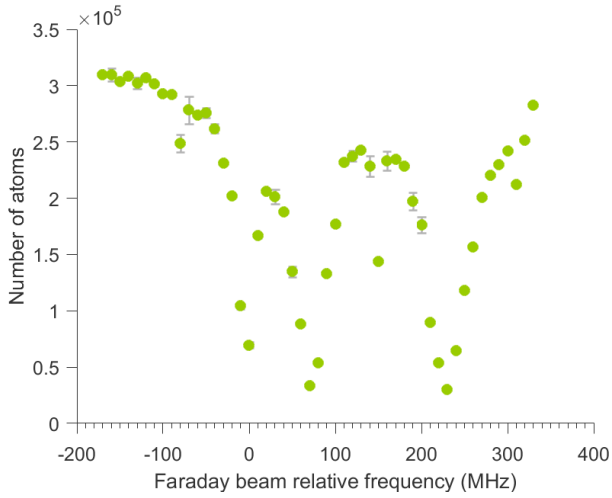

Figure 66: Faraday probe frequency relative to the $|F = 1\rangle \rightarrow |F' = 0\rangle$ transition. The peaks indicate the resonances with the $|F = 1\rangle \rightarrow |F' = 0, 1, 2\rangle$ transitions.

Part III

COHERENCE PROPERTIES OF THE SPINOR CONDENSATE: ON THE MAGNETIZATION AND ITS APPLICATION TO ULTRASENSITIVE MAGNETOMETRY

8

ATOM LOSS AND SPIN RELAXATION PROCESSES

In this chapter we discuss various processes that detrimentally affect the spinor condensate. Firstly the atom losses which are originated by collisions with the background gas or between the atoms in the condensate. The second type of processes are related to the relaxation of the spins and therefore the coherence. The coherence of an atomic system is commonly studied in terms of the concepts originally developed for nuclear magnetic resonance (NMR): the longitudinal spin relaxation time $\mathcal{T}_1$, describing the decoherence on the spin projection along the magnetic field, and the transverse spin relaxation time $\mathcal{T}_2$, which characterizes the dephasing of the spin oriented orthogonal to the magnetic field.

We have discussed already the longitudinal relaxation (see page 97), here we expand the discussion including also the transverse relaxation.

8.1 LOSSES CAUSED BY COLLISIONS

One-body losses are due to collisions with the background gas. In a thermal distribution the lifetime can be thought of in terms of the atoms kicked out of the trap. In a condensate on the other hand, much smaller energies in the order of the chemical potential are enough to kick atoms out of the condensate. Because some background atoms have energies in the low energy-tail of the Boltzmann distribution, one may expect to have lower lifetimes in a condensate as compared to a thermal system. We model the one-body losses as $\dot{N} = -N/\tau$, where τ is identified as the lifetime. In order to quantify τ we form the condensate and increase the power of the dipole trap to avoid free evaporation. In Figure 67 the number of atoms N is plotted vs time in a semi-log plot. An exponential fit yields lifetime $\tau = 7.7 \pm 0.4\,\mathrm{s}$.

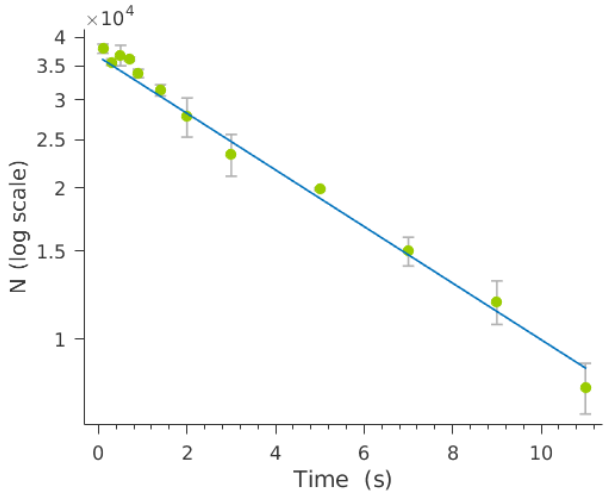

Figure 67: Lifetime of condensed atoms in $|F = 1, m_F = 1\rangle$: $7.7 \pm 0.4\,s$

Two-body collisions cause spin relaxation due to the the magnetic dipole interaction $g_F \mu_B B$ causing a spin-flip accompanied by an increase of the kinetic energy given by the Zeeman interaction. This interaction becomes a loss mechanism in magnetic traps, where a transition to a non-trapped high-field seeking state is possible. In optical traps all the Zeeman states can be trapped but two-body collisions may cause a decay into a lower hyperfine state accompanied by the release of 6.8 GHz of kinetic energy. Because we trap the atoms in the lowest hyperfine manifold $F = 1$, two-body collisions do not represent a loss mechanism.

Three-body collisions are the strongest density-dependent loss mechanism in condensates, and are usually the main cause of losses. A collision between three particles may result in the formation of a dimer or molecule plus a third atom carrying the released energy. This energy is usually very large compared to typical trap depths, so that the third atom is effectively kicked out and because the dimer can not be confined in the trap the three atoms are lost. The losses in this process can be modeled as $\dot{N} = -K_3 \int_V n(\mathbf{r}, t)^3 d\mathbf{r}$, where $\int_V n(\mathbf{r}, t)^3 d\mathbf{r} = \langle n^2 \rangle N$ and

in particular for a condensate having a Thomas-Fermi profile $\langle n^2 \rangle = c_3 N^{4/5}$ where: [Söding et al., 1999]

$$c_3 = \frac{7}{6}\frac{15^{4/5}}{(14\pi)^2}\left[\frac{M\bar{\omega}}{\hbar\sqrt{a_0}}\right]^{12/5} \tag{104}$$

We therefore write the loss equation for the contribution of one and three-body losses as:

$$\begin{aligned}\dot{N} &= -K_3\int_V n(\mathbf{r},t)^3\,d\mathbf{r} - \frac{N}{\tau}\\ &= -K_3 c_3 N^{9/5} - \frac{N}{\tau}\end{aligned} \tag{105}$$

Last expression is a Bernoulli equation that can be rewritten in terms of $u \equiv N^{1-9/5} = N^{-4/5}$ as a linear equation:

$$-\frac{5}{4}\dot{u} = -K_3 c_3 - \frac{u}{\tau} \tag{106}$$

which has the solution:

$$u(t) = (u_0 + K_3 c_3 \tau)e^{4t/5\tau} - K_3 c_3 \tau \tag{107}$$

In Figure 68 plot $u(t) = N(t)^{-4/5}$ as a function of time and fit Equation 107 to find the free parameters $K_3 c_3$ and τ. We obtain: $\tau = 7.7\,\mathrm{s}$ and $K_3 c_3 = 3.0 \pm 1.6 \times 10^{-6}\,\mathrm{Hz}$. For condensed atoms $K_3^{cond} = 5.8 \pm 1.9 \times 10^{-30}\,\mathrm{cm}^6/\mathrm{s}$ [Burt et al., 1997] and therefore $c_3 = 5.2 \pm 3.2 \times 10^{23}\,\mathrm{cm}^{-6}$.

In typical experiments with BECs, the high densities make three-body collisions the main loss mechanism. We have found that in our system this is different. Because the densities are lower, the three-body losses are smaller than the one-body losses. At the pure condensate when we have about 4×10^4 atoms, $\dot{N}/N$ drops to $1/63\,\mathrm{s}$ compared to the $1/7.7\,\mathrm{s}$ of the one-body.

8.2 SPIN RELAXATION

Longitudinal relaxation time

The longitudinal relaxation time T_1 is associated with the magnetization component along the magnetic field $\mathbf{B} = B_x\mathbf{x}$, such that

In this thesis **x**, **y** *and* **z** *represent the unit vectors along the given direction.*

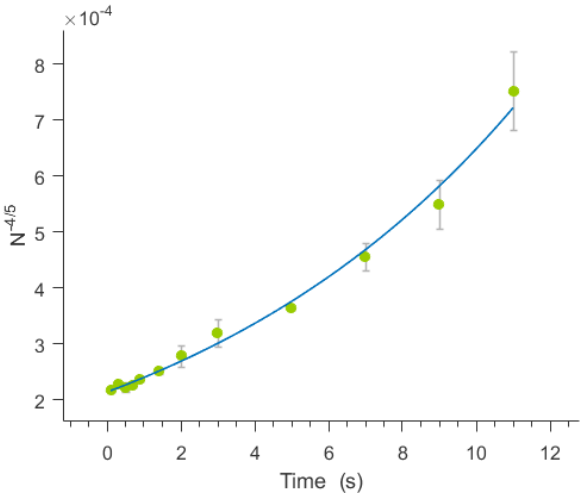

Figure 68: $N^{4/5}$ as a function of time the atoms are held in the dipole trap. By fitting function Equation 107 we find the one and three-body loss rates.

$\langle \hat{F}_x(t) \rangle = F_x^{eq} - [F_x^{eq} - F_x(0)] \exp\{-t/\mathcal{T}_1\}$, were $F_x(0)$ represents the initial mean value of the collective spin projection along $\mathbf{x}$ and F_x^{eq} represents the equilibrium component.

We measured $\mathcal{T}_1$ in the spinor condensate prepared in the state $(1,0,0)^T$ in the basis of the applied bias field $B_x\mathbf{x}$. It is interesting to notice that this configuration is the mean-field ground state of a ferromagnetic spin-1 condensate: the energy of the system is minimized when all the atoms are aligned along the magnetic field according to the functional energy in Equation 46, as described in [Kawaguchi and Ueda, 2012]. This implies $F_x^{eq} = F_x(0)$ and therefore it is expected $\langle \hat{F}_x(t) \rangle = F_x(0)$ or equivalently $\mathcal{T}_1 \simeq \infty$. In Figure 69 we plot the population in $m_F = 1$ normalized by the total number of atoms vs time, this is $\langle \hat{F}_x(t) \rangle / N(t)$. By fitting an exponential decay to the data we see that the relaxation is negligible in the 5 s time scale, and therefore $\langle \hat{F}_x(t) \rangle$ is only limited by the lifetime of the atoms: $\mathcal{T}_1 = \tau$.

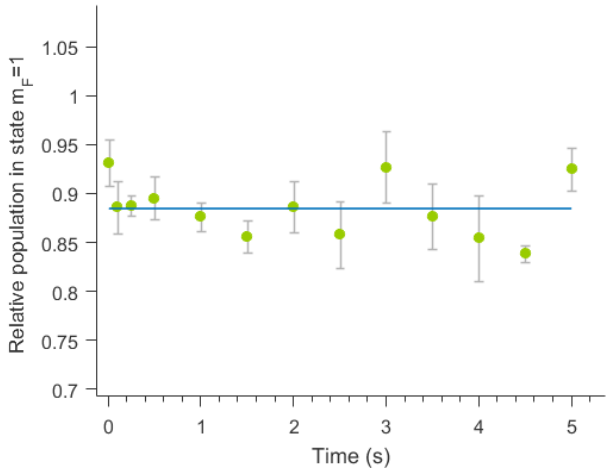

Figure 69: Relative population in $m_F = 1$ (measured with Stern-Gerlach imaging) as a function of time of a spinor condensate of atoms aligned with a bias field. The invariant population is the signature that the longitudinal relaxation time is much larger than the observation time.

Transverse relaxation time: Measurement of $\mathcal{T}_2$

There are more physical processes that contribute to the transverse relaxation than to the longitudinal relaxation. Two examples are the magnetic field fluctuations and the interactions between spins that can cause dephasing and decoherence.

For an individual atom interacting with a magnetic field $B_x\mathbf{x}$, the transverse relaxation time $\mathcal{T}_2$ is defined through: $|\mathbf{f}_\perp(t)| = |(\langle\hat{f}_y(t)\rangle, \langle\hat{f}_z(t)\rangle)| = f_\perp(0)\exp\{-t/\mathcal{T}_2\}$, where $f_\perp(0)$ indicates the initial magnitude of the spin on the plane yz.

For an ensemble of atoms, the individual spin operators would be replaced by the collective operators. Because the atoms occupy a finite volume, the average over the full ensemble contains also information about spatially dependent mechanisms which could affect the transverse magnetization. Those mechanisms do not originate from a relaxation process but cause dephasing or broadening in the same way relaxation does. The most common example is the effect of spatial inhomogeneities of the

magnetic field: if the spins precess around a field which depends on their position $\mathbf{B} = \mathbf{B}(r)$, different spins will precess at different Larmor frequencies and therefore the ensemble will dephase in time. This means that $\mathbf{F}_\perp(t)$ would show a free induction decay dynamics even if the system posses an infinite $\mathcal{T}_2$. This type of mechanism together with the transverse relaxation are usually characterized by $\mathcal{T}_2^*$ such that $|\mathbf{F}_\perp(t)| = |F_\perp(0)| \exp\{-t/\mathcal{T}_2^*\}$ [Abragam, 1961; Behbood et al., 2013].

In practice, $|\mathbf{F}_\perp(t)|$ would be measured averaging not only over the ensemble but also over different repetitions of the experiment to gain statistics. This has the consequence that the signal is strongly dependent on time fluctuations of the experimental conditions. If for example the magnetic field changes between repetitions, each experiment would generate a $\mathbf{F}_\perp(t)$ with a different phase, and thereby the average would show a relaxation-like behaviour independent of the processes described by $\mathcal{T}_2^*$. We will characterize the combined effect of all these processes causing relaxation or relaxation-like behavior with the transverse coherence $\overline{\mathcal{T}}_2$.

As we have seen in Chapter 3 the Zeeman dynamics of the atoms in a magnetic field is an oscillation at the Larmor frequency amplitude modulated by the quadratic Zeeman shift. In our trap, with atoms cooled near the transition temperature, and for moderate fields, the amplitude modulation is faster than any spin relaxation process. The spin evolution in our system is therefore observed not as the typical free induction decay but rather, an amplitude modulation of it such that: $\hat{F}_z(t) \propto \cos(\omega_Q t)\cos(\omega_L t)\exp\{-t/\overline{\mathcal{T}}_2\}$. To measure $\overline{\mathcal{T}}_2$ of our system we prepare the state $(1,0,0)^T$, defined by the quantization axis along the set bias magnetic field $B_x\mathbf{x}$, $B_x = 42\,\mu T$ and apply a $\pi/2$ pulse to rotate the atoms to the $\left(1/2, 1/\sqrt{2}, 1/2\right)^T$ state. The atoms are allowed to precess during a time evolution t_e around the magnetic field before they are probed with a τ_p =100 µs Faraday pulse containing 3×10^6 photons. The Faraday pulse gives us information about the mean value of the collective spin component along $\mathbf{z}$ (see Section 2.3.2). We perform measurements at different values of t_e ranging from 0 to 1 s in

We wrote the explicit equations when $\mathbf{B} = B_z\mathbf{z}$, for $\mathbf{B} = B_x\mathbf{x}$ its completely analogous due to the symmetries of the system.

steps of 10 ms, each one on a new preparation of the state. The signal from each pulse is fitted with a sinusoidal function that oscillates at the Larmor frequency ($\nu_L = 294\,\text{kHz}$). The signals are normalized by the total number of atoms to account for the atom losses. Figure 70 shows some example of the fits for different repetitions of the experiment after $t_e = 10\,\text{ms}$. Notice they exhibit large relative phases already at this time scale but that the amplitudes are constant. This is the case also for much longer time scales up to $t_e = 1\,\text{s}$, which was the longest observation time. The amplitude is modulated but the full visibility is always recovered. This implies the coherence is very large ($\mathcal{T}_2^* \simeq \mathcal{T}_2 \simeq \mathcal{T}_1$ in the s scale), and only the average over different repetitions contributes to the free induction decay.

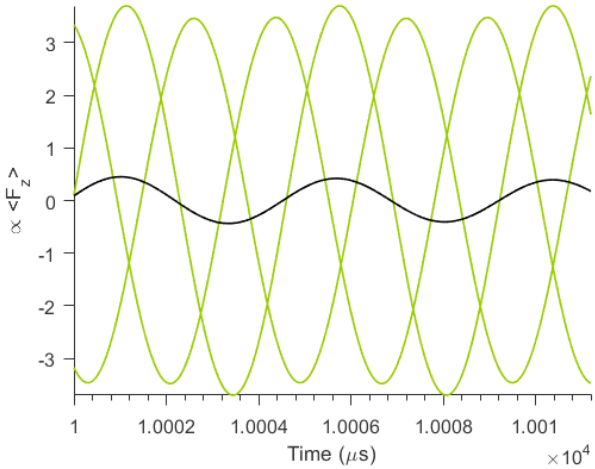

Figure 70: Fit to a signal proportional to $\langle \hat{F}_z(t) \rangle$ vs time for different repetitions of the same experiment when $t_e = 10\,\text{ms}$.

First, to illustrate the long coherence of the state, we take the fits to the individual signals (each one corresponds to a different trial) and recover the amplitudes. We plot the square of such amplitudes (remember they are normalized by the number of atoms) as a function of t_e as shown in Figure 71. The amplitudes square are fitted with a function $\propto [\cos(\omega_Q t)\exp\{-t/\mathcal{T}_2^*\}]^2$. From the fit, we find $\omega_Q = 12.4 \pm 2.0\,\text{Hz}$ and $\mathcal{T}_2^* >> 1$ (much longer than the observation time).

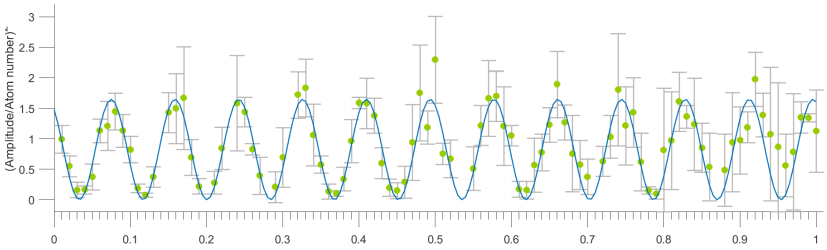

Figure 71: Normalized amplitude square (arb. units) vs time (s) of the Faraday rotation signal when probing condensed atoms undergoing Larmor precession with long $\mathcal{T}_2^*$.

Second, to measure $\overline{\mathcal{T}}_2$ one should take the average of the fits of the individual signals per each t_e and fit a damped oscillation decaying at rate $1/\overline{\mathcal{T}}_2$, as described before. However, we don't have enough statistics and with too few repetitions the average never becomes completely destructive even for very large random relative phases, which prevents from recovering a reliable value of $\overline{\mathcal{T}}_2$. Another alternative is built upon the identification of the variations of the magnetic field as the main mechanism of dephasing. Such variations of the ambient magnetic field between repetitions of the experiment have been studied in Appendix D In that appendix we developed a stochastic model of the field based on the measurements performed with a fluxgate sensor. The alternative to estimate $\overline{\mathcal{T}}_2$ consists on using such a model of the field and recreate the measurements we described above with more statistics. We perform simulations of the spin dynamics and compute the average of 200 traces. The average square is plotted and fit with a function $\propto [\cos(\omega_Q t)\exp\{-t/\overline{\mathcal{T}}_2\}]^2$, as shown in Figure 72. From the fit we find $\overline{\mathcal{T}}_2 = 1.3 \pm 0.1$ ms.

In conclusion, we have demonstrated that the spinor condensate exhibits neither homogeneous nor inhomogeneous dephasing: $\mathcal{T}_1 \simeq \mathcal{T}_2 \simeq \mathcal{T}_2^*$, all limited only by the losses of atoms characterized by the lifetime $\tau = 7.7 \pm 0.4$ s. Another type of relaxation-like behavior is actually present though. It is related with the average over different runs of the experiment and is characterized by the decay time $\overline{\mathcal{T}}_2 = 1.3 \pm 0.1$ ms. We argue this dephasing is primarily due to the amplitude fluctuations of the magnetic field, this means that a priori knowledge of the magnetic field to

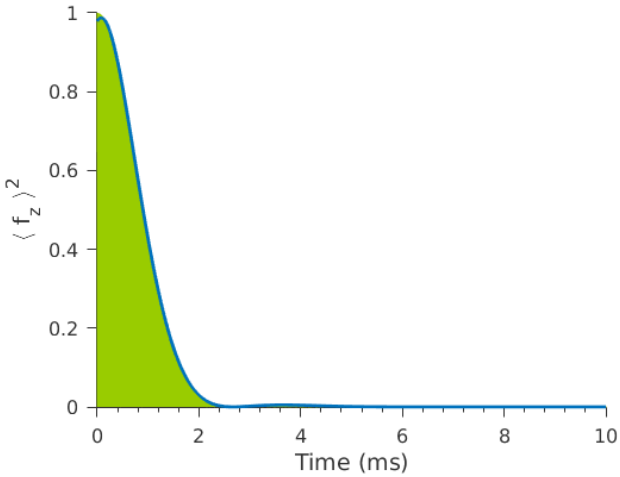

Figure 72: Amplitude square of the average of 200 traces showing the precession of the atoms in the present of a magnetic field than fluctuates in time (green). Damped oscillation fit (blue) from which we estimate $\overline{\mathcal{T}}_2$. Simulations based on the model of the magnetic field of the laboratory detailed in Appendix D.

rephase the individual signals, or active cancellation of the field to suppress it should extend $\overline{\mathcal{T}}_2$ by orders of magnitude.

Non-condensed atoms

In the same manner we study the coherence properties of non-fully condensed clouds. In Figure 73 we show the results of the same experiment described above to obtain $\mathcal{T}_2^*$. For ensembles when the condensed fractions are $c_F = 0\,\%$, $15\,\%$ and $40\,\%$, the corresponding decay times are measured to be: $\mathcal{T}_2^* = 2.4\,s$, $2.6\,s$ and $3.4\,s$, respectively. This shows the importance of using condensed systems when long coherence times are required.

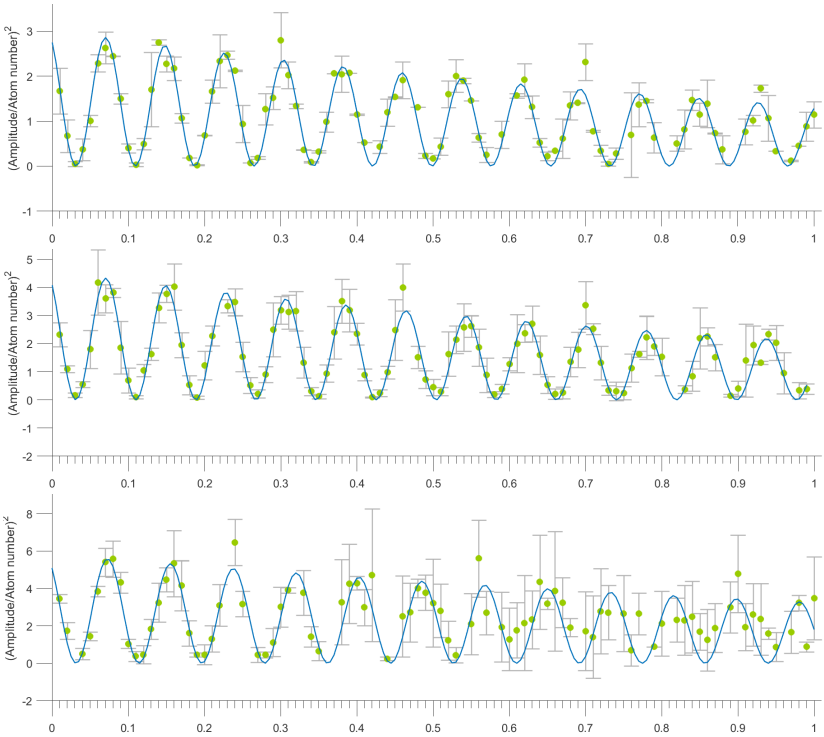

Figure 73: Normalized amplitude square (arb. units) vs time (s) of the Faraday rotation signal when probing atoms in the presence of a magnetic field. Different plots from top to bottom correspond to condensed fractions $c_F = 0\,\%$, $15\,\%$ and $40\,\%$, respectively. The exponential decay time is found to be $\mathcal{T}_2^* = 2.4\,\mathrm{s}$, $2.6\,\mathrm{s}$ and $3.4\,\mathrm{s}$, respectively.

9

MAGNETIC SENSING WITH SPINOR CONDENSATES

In recent years optical magnetometers became some of the most sensitive and versatile magnetic sensors, they even have surpassed the sensitivity of superconducting quantum interference devices (SQUID's) [Dang et al., 2010; Vengalattore et al., 2007], the ubiquitous technology for precise magnetic field measurements from geophysical purposes [Chwala et al., 2015] to neuroimaging [Wilson et al., 2016] and biomagnetism [Körber et al., 2016]. The operational principle is an indirect measurement of the spin state of an atomic ensemble undergoing Larmor precession around the magnetic field to be measured. Fundamentally, an optical magnetometer is only limited by the projection-noise inherent to the quantum nature of the atoms, nevertheless this limitation has been surpassed using squeezed atomic spin states [Colangelo et al., 2017; Koschorreck et al., 2010b] in cold atomic ensembles. The best sensitivities though have been achieved with high-density vapor cells reaching $\sim fT/Hz^{1/2}$. Hot atomic ensembles nevertheless have the drawback that their spatial resolution is in the cm^3-mm^3 scale [Dang et al., 2010], as compared to the sub mm scale of cold ensembles. Most of these optical sensors are limited by dephasing and decoherence that spin-exchange collisions and inhomogeneities can induce [Budker and Romalis, 2007], this translates into a limited interrogation time to the μs-ms scale.

In order to compare the performance of different magnetometers one has to account for both sensitivity and spatial resolution. The figure of merit in the field of magnetometry is often taken as the sensitivity vs square root of volume. In optical magnetometers the sensitivity times the root of the volume, scales as $1/\sqrt{n\mathcal{T}}$ with n being the density and $\mathcal{T}$ the coherence time. This relation suggests that the best magnetometer has to be built upon the most dense and coherent system available: a spinor condensate

appears to be the best candidate. Because of the small volume of the condensate, the spatial resolution is orders of magnitude better than for vapor cell magnetometers. In addition, the low energy of condensates prevents decoherence processes like hyperfine changing collisions, and leads to coherence times of seconds. A spinor condensate can be formed in a ferromagnetic ground state where the internal interactions protect the collective spin state from inhomogeneous magnetic fields [Vanderbruggen et al., 2015]. In this chapter we describe the experimental realization of our spinor condensate magnetometer.

[Jiménez-Martínez and Knappe, 2017] compared some of the records in each technology from SQUID's and Hall probes to Magnetic force microscopes and optical magnetometers. In this compilation it becomes evident that all these different technologies seem to be bounded in energy per unit bandwith resolution $\Delta E \Delta t$ by $\hbar$. In the case of SQUID's, it has been demonstrated the shot noise in the Josephson junctions place a limit of $\hbar$ [Tesche and Clarke, 1977], and some SQUID sensors [Schmelz et al., 2017] have already reached that limit. In contrast, as we describe below, standard descriptions of atomic sensors show no limitation. Moreover, in Section 9.1 we will show experimental evidence that this limit does not in fact exist.

9.1 STANDARD QUANTUM LIMIT IN ATOMIC SENSORS

An optical magnetometer infers information about the magnetic field from the spin state dynamics of the atoms. Its resolution is fundamentally limited by the projection-noise associated to quantum mechanics and can be written for a single measurement as: $\delta B_{PN}[T] = \hbar/(g_F \mu_B \mathcal{T}\sqrt{2fN})$ where g_F is the ground-state Landé factor, μ_B the Bohr magneton, N the number of atoms, $\mathcal{T}$ the coherence time of the system and $f = 1$ for a spin-1 system. This can be improved by repeatedly probing the state for a total time Δt, for which the sensitivity, now given in units of $T/Hz^{1/2}$ is: [Budker and Romalis, 2007]

$$\delta B_{PN}[T/Hz^{1/2}] = \frac{\hbar}{g_F \mu_B \sqrt{2N\mathcal{T}\Delta t}}. \tag{108}$$

As we stated earlier, one attractive feature of using a spinor condensate as a magnetometer is its small size, which implies great spatial resolution. For this reason we focus on the energy resolution defined by the volume of the system in the following way.

Consider a system with finite volume V in a magnetic field with amplitude B_0. The energy of this system is $B_0^2 V/2\mu_0$. A change in the magnetic field to a new value $B_0 + \Delta B$ and energy $(B_0 + \Delta B)^2/2\mu_0$ will give the system an extra energy $(\Delta B^2 + 2|B_0|\Delta B)V/2\mu_0$, that can be interpreted as the energy resolution. The uncertainty in the energy is minimized for $B_0 = 0$. In this case we can write the minimum uncertainty or energy resolution per unit bandwidth using $\delta B_{PN}[T]$ in the form:

$$\Delta E \Delta t \simeq \frac{\hbar^2 V}{4 g_F^2 \mu_0 \mu_B^2 N \mathcal{T}} \tag{109}$$

This relation shows that high densities and especially long coherences are desirable properties for high energy resolution sensors. In the following sections we detail the characterization of the relevant parameters V and $\mathcal{T}$ to estimate the sensitivity of our magnetometer.

Based on the measured properties of the system: $\mathcal{T} = 7.7\,s$ and $N = 5 \times 10^4$ atoms, and according to Equation 108 with $\Delta t = 1\,s$, the sensitivity is $27\,fT/Hz^{1/2}$. This is about two orders of magnitude less sensitive than the record with an atomic magnetometer, $160\,aT/Hz^{1/2}$ [Dang et al., 2010]. That instrument is, however, far larger than our system with a volume of $V = [0.76\,cm]^3$ compared to $V = [11.9 \pm 0.9\,\mu m]^3$ from our system (see Section 9.2). When compared in terms of the energy resolution, the cited work reports $44\hbar$, four orders of magnitude larger than the predicted value of our magnetometer $4.8 \times 10^{-3}\hbar$ according to Equation 109, which represents the best energy resolution per unit bandwidth that has been demonstrated or reported so far in atomic systems ($10\hbar$ was predicted for a spinor BEC in [Wood et al., 2015]).

In the following sections we detail the experiments to measure each of the relevant parameters defining our magnetometer.

9.2 SPATIAL RESOLUTION

In order to determine the volume of the condensate we estimate the Thomas-Fermi mean radius from the mean oscillation frequency $\bar{\omega}$ at the end of the forced evaporation, using the well known relation for non interacting bosons $c_F = 1 - (T/T_c)^3$, where c_F is the condensed fraction and $T_c = \hbar\bar{\omega}[N/\zeta(3)]^{1/3}/k_B$ [Pethick and Smith, 2002]. We vary only the initial number of atoms and fix the final configuration of the trap. In this way the temperature T and $\bar{\omega}$ stay constant, and only changes in N contribute to c_F.

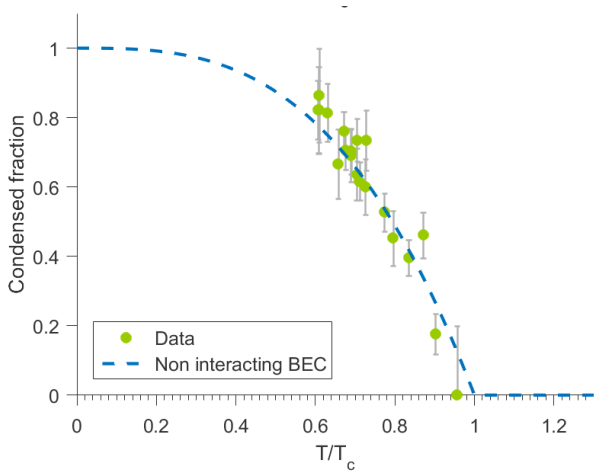

Figure 74: Condensed fraction as function of T/T_c. T and $\bar{\omega}$ are constant and only N varies.

Figure 74 shows c_F as function of T/T_c where the measured temperature is $T = 59(12)$ nK, from which we estimate $\bar{\omega} = 2\pi 55(10)$rad/s. This mean frequency is related to the mean size of the condensate, which in the Thomas-Fermi approximation is given by:

$$\bar{R}_{TF} = \left(\frac{15Na_0}{\bar{a}}\right)^{1/5} \bar{a} \tag{110}$$

where $\bar{a} = \sqrt{\hbar/(m\bar{\omega})}$ and a_0 is the scattering length (see Table 1), a_B is the Bohr radius, for the measured mean frequency

we estimate $\bar{R}_{TF} \simeq 7.5 \pm 0.5\,\mu m$ and therefore we conclude the volume is:

$$V = 4/3\pi\bar{R}_{TF}^3 = [11.9 \pm 0.9\,\mu m]^3 \tag{111}$$

The final shape of the atom distribution is just slightly anisotropic with the longest size being a factor of < 2 longer, as evidenced by the anisotropic expansion of the cloud (see Figure 45), which implies the Thomas-Fermi radius in each direction is about $R_{TF} \simeq (6, 6, 12)\,\mu m$.

The size of the condensate is smaller than the spin healing length $\xi_s \simeq 12\,\mu m$ (see Section 4.4), this implies it is too energetically costly for the system to break into different spin domains in contrast to other spinor magnetometers like [Vengalattore et al., 2007; Higbie, 2005]. This fact guaranties the system has a single spin domain.

9.3 THE COHERENCE AND MAXIMUM INTERROGATION TIME

Following the discussion and results presented in Section 8.2 the coherence time of our magnetometer $\mathcal{T}$ is not limited by relaxation nor by inhomogeneous effects, which means $\mathcal{T}_1 \simeq \mathcal{T}_2 \simeq \mathcal{T}_2^* >> 1\,s$. More evidence was given in the last section where we have concluded that the spinor condensate has only one spin domain, this is, all the atoms stay aligned protected from inhomogeneities by the ferromagnetic interactions.

The losses, on the other hand, represent a limitation at long interrogation times. Such losses are due to the one and the three-body collisions, and according to the values we measured and presented in Section 8.1, the lifetime is $\tau = 7.7 \pm 0.4\,s$ and the three-body loss rate $K_3 c_3 = 3.0 \pm 1.6 \times 10^{-6}\,Hz$. They represent a reduction of 10% in the number of atoms in 1 s.

In practical terms, there is another relaxation-like limitation that arises from extracting information by averaging over different repetitions of the experiment. We believe this is entirely caused by the fluctuations of the magnetic field in the laboratory,

and therefore does not represent a fundamental limitation to the performance of our system.

We can conclude that the coherence, indicating the decay of $|\mathbf{F}|$ not normalized by N, of our spinor condensate coincides with the lifetime $\tau = 7.7 \pm 0.4\,\mathrm{s}$. The interrogation time can be as large as 7.7 s, we have explicitly proven full visibility for single measurements with no significant reduction of SNR of the Faraday proving due to atom losses for up to 1 s. The interrogation time is conditioned by the quadratic Zeeman shift, which modulates the visibility of the magnetometer.

9.4 THE SENSITIVITY

The principle of the magnetometer is the utilization of atoms precessing around the magnetic field to be measured. Faraday probing is employed to read the spin state of the precessing atoms at two moments in time separated by Δt. The spin operator $\hat{F}_z$ associated to an ensemble of atoms undergoing Larmor precession around a magnetic field $B_x\mathbf{x}$ evolves according to $\hat{F}_z(t) = \hat{F}_z(0)\cos(\omega_L t) + \hat{F}_y(0)\sin(\omega_L t)$, analogously as we have shown in Equation 23. This ensemble interacting with a beam defines the Faraday rotation characterized by the dynamics:

$$\hat{S}_y(t) = \hat{S}_x(0)\sin\theta(t) + \hat{S}_y(0)\cos\theta(t) \tag{112}$$

$$\theta(t) = G_1[\hat{F}_z(0)\cos(\omega_L t) + \hat{F}_y(0)\sin(\omega_L t)] \tag{113}$$

Notice that for the typical values of the experiment: $G_1 = 10^{-7}$ rad/spin (see Figure 65), $F(0) \leqslant |m_F|N$, and $N \leqslant 10^5$, $|\theta| \leqslant |G_1 F(0)| \leqslant |G_1 N| \sim 10^{-2} \ll 1$. This allows us to rewrite Equation 112 as:

$$\begin{aligned}\hat{S}_y(t) &\sim \hat{S}_x(0)\theta(t) + \hat{S}_y(0), \\ &= \hat{S}_x(0)G_1[\hat{F}_z(0)\cos(\omega_L t) + \hat{F}_y(0)\sin(\omega_L t)] + \hat{S}_y(0).\end{aligned} \tag{114}$$

In order to estimate the uncertainty in the measurement of a spin state and consequently of the magnetic field, it is convenient

to rewrite the above expression as a function of one oscillating function with amplitude and phase:

$$\hat{S}_y(t) = A\sin(\omega_L \tau_p + \varphi) + d, \tag{115}$$

where now parameters of interest are related through:

$$A = G_1 \hat{S}_x(0)\sqrt{[\hat{F}_z(0)]^2 + [\hat{F}_y(0)]^2}, \tag{116}$$

$$\varphi = \text{atan2}(-\hat{F}_y(0), \hat{F}_z(0)), \tag{117}$$

for the four quadrant arctangent function:

$$\text{atan2}(y,x) = \begin{cases} \arctan\frac{y}{x} & x > 0 \\ \arctan\frac{y}{x} + \pi & x < 0, y \geqslant 0 \\ \arctan\frac{y}{x} - \pi & x < 0, y < 0 \\ \pi/2 & x = 0, y > 0 \\ -\pi/2 & x = 0, y < 0 \\ \text{undefined} & x = y = 0 \end{cases} \tag{118}$$

From Equation 115 we can see that performing two measurements separated by Δt with outputs A_1, φ_1 and A_2, φ_2 allows us to determine the strength of the magnetic field the atoms are precessing around as a function of the relative phase:

$$|B| = \frac{\varphi_2 - \varphi_1}{\gamma \Delta t} \equiv \frac{\varphi}{\gamma \Delta t} \tag{119}$$

where $\gamma = g_F \mu_B/\hbar = -2\pi \cdot 7 \times 10^9$ rad s^{-1}T^{-1} is the gyromagnetic ratio. Since Δt and γ are constants, the noise in B is only determined by the noise in the estimated value of φ:

$$\delta|B| = \frac{\delta\varphi}{\gamma \Delta t}. \tag{120}$$

In order to determine $\delta\varphi$ we make statistics on many measurements each one consisting in a pair of Faraday pulses of length l separated by Δt. Each measurement is synchronized with the

mains and because Δt is very short compared to the magnetic field fluctuations we have measured, we assume the background magnetic field is constant between both measurements and therefore ω_L can be fixed to the Larmor frequency. An example of the data is shown in Figure 75

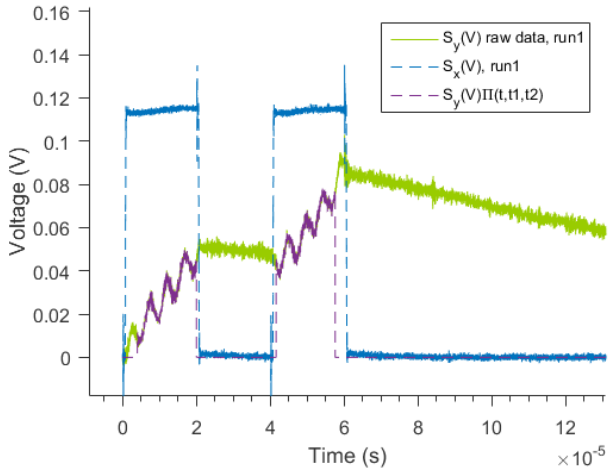

Figure 75: Raw signals showing $\hat{S}_x(V)$, and $\hat{S}_y(V)$, as well as the modified signal $\hat{S}_y(V)\Pi(t,t1,t2)$ where $\Pi(t,t1,t2) \equiv \Pi((t-t1)/l) + \Pi((t-t2)/l)$ for $t1$ and $t2$ being the times at the center of the pulses. $\Pi((t-t^*)/l)$ is the generalized rectangle function centered at t^* and full-width l.

The linear trend in the signals shown above is the result of an initial imbalance $\hat{S}_y(0) \neq 0$ and the discharge of the capacitor of the differential detector. This contribution doesn't contribute to the measurement of the magnetic field, for this reason we subtract it from the signal. The resulting signal is then fitted to a function:

$$\begin{aligned} M_f(t) = &[s_{f1}\sin(\omega_L t) + c_{f1}\cos(\omega_L t)]\,\Pi((t-t1)/l) \\ &+ [s_{f2}\sin(\omega_L t) + c_{f2}\cos(\omega_L t)]\,\Pi((t-t2)/l). \end{aligned} \tag{121}$$

for $t1 = 11.992\,\mu s$, $t2 = t1 + \Delta t$ with $\Delta t = 21.6\,\mu s$, $l = 16.0\,\mu s$, all known with a temporal resolution of $4\,ns$, limited by the ac-

quisition instrument. The frequency is fixed to the mean known value $\omega_L = 211.0\,\text{kHz}$. The rectangular function is defined as:

$$\Pi(x) = \begin{cases} 0 & |x| > 1/2 \\ 1 & |x| \leqslant 1/2 \end{cases} \tag{122}$$

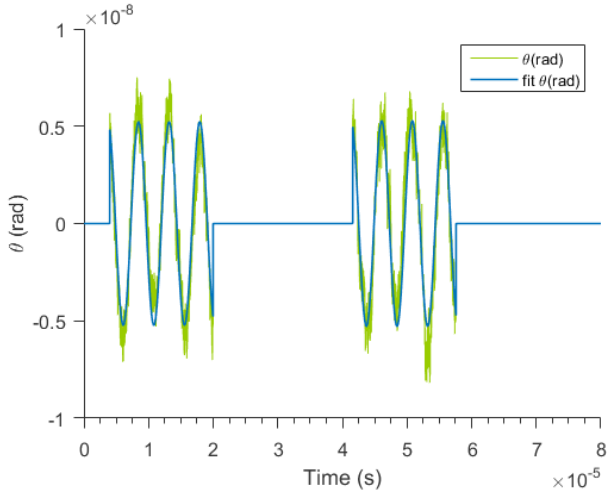

Figure 76: Example of signal of one Faraday measurement after the linear trend is subtracted. The linear fit follow the form shown in Equation 121.

An example of the fitted function is shown in Figure 76. The parameters are found using a least squares method and assuming the uncertainty in the data is not time dependent. From the parameters that minimize the error we can obtain the relative phase between the pulses $\varphi_f = \text{atan2}(c_{f2}, s_{f2}) - \text{atan2}(c_{f1}, s_{f1})$ for each measurement.

We perform the same fit procedure to $f_{rep} = 40$ different measurements and obtain the mean value of $\varphi = 1/f_{rep} \sum_1^{f_{rep}} \varphi_f$ and its standard deviation $\delta\varphi = \sqrt{\text{var}(\varphi)}$ for the variance given by $\text{var}(\varphi) = 1/f_{rep} \sum_1^{f_{rep}} |\varphi_f - \varphi|^2$. Because φ is a function of the four parameters $\mathbf{p} = (c_1, s_1, c_2, s_2)$, $\text{var}(\varphi) = \mathbf{J}\Gamma\mathbf{J}^T$, according to the propagation of error formula. J is the Jacobian matrix that explicitly reads:

$$\mathbf{J} = \left(\frac{\partial\varphi}{\partial c_1}, \frac{\partial\varphi}{\partial s_1}, \frac{\partial\varphi}{\partial c_2}, \frac{\partial\varphi}{\partial s_2}\right) \tag{123}$$

$$= \left(\frac{s_1}{c_1^2+s_1^2}, \frac{-c_1}{c_1^2+s_1^2}, \frac{-s_2}{c_2^2+s_2^2}, \frac{c_2}{c_2^2+s_{f2}^2}\right) \tag{124}$$

since for $x \neq 0$:

$$\begin{aligned}\frac{\partial}{\partial y}\text{atan2}(y,x) &= \frac{x}{x^2+y^2} \\ \frac{\partial}{\partial x}\text{atan2}(y,x) &= \frac{-y}{x^2+y^2}.\end{aligned} \tag{125}$$

and the variance-covariance symmetric matrix:

$$\Gamma \equiv \begin{pmatrix} \text{var}(c_1) & \text{cov}(c_1,s_1) & \text{cov}(c_1,c_2) & \text{cov}(c_1,s_2) \\ \text{cov}(s_1,c_1) & \text{var}(s_1) & \text{cov}(s_1,c_2) & \text{cov}(s_1,s_2) \\ \text{cov}(c_2,c_1) & \text{cov}(c_2,s_1) & \text{var}(c_2) & \text{cov}(c_2,s_2) \\ \text{cov}(s_2,c_1) & \text{cov}(s_2,s_1) & \text{cov}(s_2,c_2) & \text{var}(s_2) \end{pmatrix} \tag{126}$$

with $\Gamma_{ij} = \Gamma_{ji}$. The estimated variance is $\text{var}(\varphi) = 2.7 \times 10^{-3}\,\text{rad}^2$. For this value and $\Delta t = 21.6\,\mu\text{s}$, according to Equation 120, $\delta|B| = 54.7\,\text{nT}$, or equivalently $\delta|B| = 254\,\text{pT}/\text{Hz}^{1/2}$.

The noise of this measurement includes the noise of the detector, the shot noise in the light and the noise in the atomic state. We have demonstrated the detector is shot-noise limited for the used number of photons (see Figure 61), in addition, We perform relative measurements of the phase, therefore the preparation state noise cancels out. All this suggests that the major contribution to the noise is the fluctuations of the magnetic field from preparation to preparation. A detailed discussion of magnetic field noise is given in Appendix D were we conclude that the typical fluctuations of the magnetic field in the lab induce a relative variance of the order of $\sim$ mrad^2 for the time scales discussed in this section.

10

PERSPECTIVES

In this thesis I have described an efficient system for production of single-mode spinor BECs, paired with a high-sensitivity non-destructive spin measurement using Faraday rotation. As described in Chapter 9, the coherence properties of this system are already remarkable, and the system has taught us something fundamental about quantum effects in sensing, namely that there is no "$\hbar$ energy resolution limit" for field sensing.

In the following lines I describe a number of other open problems that could be studied in our spinor system.

Energy resolution bounds of quantum systems

Beginning in the 1980s, quantum limits to the energy resolution, i.e., to the minimum smallest energy difference that can be detected, of arbitrary quantum systems have been discussed. Such limits are related to the limited information-storing capacity of the system. According to Bekenstein it is the maximum entropy associated with the macroscopic observable that quantifies and delimits the amount of information that may be encoded and read out from the system. The system has finite entropy and therefore finite resolution because it has finite energy and size. [Bekenstein, 1984].

The bound he proposed is:

$$S/E < 2\pi R/\hbar c \tag{127}$$

where $S = \ln(\mathcal{N}(E))$ is the entropy of the system with $\mathcal{N}(E)$ being the number of states with energies lower that E. E is the total energy available (including rest masses but not considering vacuum energy nor zero-energy states) and R is a length characterizing characterizing the spatial extent of the motion of the particles of the system. He demonstrates this bound is necessarily

satisfied by simple quantum-mechanical systems (vibrators and rotators) and therefore relevant to the issue of storage of information in atomic or molecular degrees of freedom. He also concludes that for three dimensional systems, whose aspect ratios are not too extreme, that the knowledge of the first one-particle level suffices to estimate $\max(S/E)$, and shows that Equation 127 is respected in general.

Other works consider a bound rather in terms of the maximum speed of dynamic evolution, a bound on the maximum number of distinct states that the system can pass through, per unit of time if the system has finite energy. Margolus and Levitin found that for $\Delta E = E - E_0$ with E being the average energy of the initial state and E_0 the ground state energy, it would take a time [Margolus and Levitin, 1998]

$$\Delta t \geqslant \frac{h}{4\Delta E} \tag{128}$$

for any quantum system to evolve into an orthogonal state. Notice that $\Delta t \Delta E$, the energy resolution per unit bandwidth, is then limited by $\hbar/4$ for any arbitrary quantum system. It is important to note that this is not an uncertainty relation. Here ΔE indicates the average energy above the ground level, not its uncertainty.

[Tesche and Clarke, 1977] demonstrated that in SQUIDs, the shot noise in the Josephson junctions actually limits their sensitivity to $\hbar$. In the particular example of an atomic magnetometer, no theoretical work has formally described what physical process could set a bound. So far, the standard models predict an unbounded energy resolution (see Equation 109). Even though, as shown in [Jiménez-Martínez and Knappe, 2017] a number of different magnetometer technologies seem to be close to the $\hbar$ limit, despite very different dimensions and sensitivities.

There have been discussions on the potential explanations brought by John Kitching, Mike Romalis and Morgan Mitchell [Mitchell and Kitching; Mitchell], in terms of the contribution of the dipolar interactions between the atoms themselves: the field generated in a sphere of atoms is $\mathbf{B} = 2\mu_0\mathbf{M}/3 = 2\mu_0 g_F \mu_F \mathbf{F}/3V$, and

for the uncertainty in the angular momentum of a coherent state $\delta\hat{F}_x^2 \geqslant N/4$, one can associated to the given field an uncertainty:

$$\delta B_{dip} = \frac{g_F \mu_0 \mu_B \sqrt{N}}{3V}. \tag{129}$$

Adding the standard projection noise (Equation 108) to this dipolar noise as uncorrelated quantities one obtain:

$$\delta E = \frac{\delta B^2 V}{2\mu_0} \geqslant \frac{\hbar}{3\Delta t} \tag{130}$$

The question whether $\hbar$ represents a limit or not to a magnetometer sensitivity sets, in terms of our current knowledge, a great opportunity for the single domain spinor system to solve this dichotomy. We demonstrated in Chapter 9 that the predicted sensitivity of our magnetometer, according to standard magnetometry theory, is orders of magnitude below the conjectured limits Equation 128 and Equation 130.

Low magnetic field physics

In our system the limitation to the sensitivity comes from the magnetic field variations of the magnetic field as we perform statistics over different preparations of the state. To reach the projection-noise limited sensitivity, one can try different strategies. One is to reduce the environmental noise of the magnetic field applying an active cancellation signal that suppresses the undesired field. Many groups have implemented these technique and have demonstrated suppression to a level of up to 5 nT [Smith et al., 2011] using the atoms as feedback sensor. More interesting is the case when using an external sensor to feedback. [Pasquiou et al., 2011](see supplementary material) used the signal of a fluxgate sensor located 15 cm away from the condensate to feedback. Within the 20 cm spatial range around the atoms, they demonstrated stabilities of 10 nT at DC and 50 nT at AC. Passive cancellation or shielding of the chamber with a high-permeability enclosure would also provide better environmental conditions [Donley et al., 2007]

A second option to reach the desired sensitivity is to use an extra sensor to obtain information about the field in time an use it to better predict the evolution of the atomic sensor. A good option would be using our fluxgate which is more sensitive that the atoms although possess a much larger volume. In a similar direction one could perform differential measurements on two spatially separated spinor condensates to become insensitive to the common-mode field noise.

The combination of these strategies would not only allow us to solve the above-posed question on the energy resolution, it would also open the possibility to study a new experimental regime at ultralow magnetic fields where the magnetic dipole-dipole interactions (MDDI) dominate the dynamics of the system as compared to the typical case where the Zeeman energy overshadows the weak MDDI.

In such a regime, many interesting phenomena have been predicted, some examples are the existence of many quantum phases [Góral et al., 2002] some of them exhibit spontaneous magnetic ordering in the form of intricate spin textures [Yi and Pu, 2006]. Because MMDI couple the spatial and spin degrees of freedom, the geometry of the system plays a fundamental role in the magnetic ordering, [Yi et al., 2004] proposed that by changing the trap shape it is possible to effectively tune MDDIs and explore different phase transitions.

Magnetic sensing with spinor condensates beyond the standard quantum limit

Squeezing has been demonstrated in a number of experiments with atomic and light states, our group in particular has made many contribution to the field [Colangelo et al., 2017; Sewell et al., 2012; Wolfgramm et al., 2010, 2013]. Those techniques have been proposed to be applied to spinor condensates to exploit the additional long coherence times and small spatial resolution these systems offer [Esteve J. et al., 2008; Johnsson et al., 2013; Riedel Max F. et al., 2010]. One of the major challenges in the application of squeezing to spinor condensates involve achieving

superclassical scaling [Brask et al., 2015]. Scalability of squeezed states with atom number is threatened by the three body losses which limit the maximum densities. [Muessel et al., 2014] suggested that to keep these losses negligible the best strategy is to realize an array of many individual condensates with an optical lattice, instead of increasing the volume which could in principle limit squeezing due to uncontrolled nonlinear multimode dynamics. They have demonstrated sub-shot-noise sensitivity of $1.86 \pm 0.28\,\mathrm{nT/Hz^{1/2}}$ at a maximum interrogation time of 342 µs, limited by fluctuations in the magnetic field. Our demonstration of classical sensitivity $253\,\mathrm{pT/Hz^{1/2}}$ in a system with very low three-body losses, situate our experiment in a very promising position to profit from quantum enhancement.

Fundamental physics: on the origin of ferromagnetism

At the beginning of the 1980's Keiji Yamada [Yamada, 1982] described by means of statistical mechanics the so called Bose-Einstein Ferromagnetism (BEF), phenomenon that consists of an spontaneous development of a macroscopic magnetization in a system of ferromagnetic bosons, always accompanying condensation. Another result is the dependence of the critical temperature with the magnetic field, which is found to be higher for larger fields up to a saturation level.

Years latter other people return to the problem and try to give an explanation in terms of modern mean-field theory of spinor BECs. [Gu and Klemm, 2003] showed that the ferromagnetic coupling, regardless of its magnitude, induces a ferromagnetic phase transition at a temperature always above the critical temperature of condensation. Moreover, the ferromagnetic coupling also increases the critical temperatures of both phase transitions. Different studies show that the phase transition could occur in three different ways depending on the properties of the system, always with the ferromagnetic transition occurring before or at the same temperature that the condensation transition [Poluektov and Savchenko, 2015]. Other works have predicted sequences of BEC transitions for different in the different magnetic states, in

the case of ferromagnetic coupling temperatures lower than the condensation temperature induce phase separation of the spin states rather than condensation in the three states[Isoshima et al., 2000].

There is very little experimental verification of the relation between magnetism and condensation. The group of Stamper-Kurn show some evidence of spontaneous magnetization associated with condensation but failed to clarify its precise relation to the BEC transition [Vengalattore et al., 2010] in part because of the limited sensitivity of their probing technique. They claim the reproducibility of the spatial spin textures has to be associated to the thermal spin equilibrium of their system. Thermal equilibrium of the spin state is difficult to reach in ^{87}Rb in $|F = 1\rangle$. Many experiments including our own observations show the slow spin dynamics. In absence of actual spin thermalization it is not clear the possible path though which magnetic ordering can occur. In our experiment the sensitivity to magnetization we achieved is remarkable, the effectively 1D spin system we produce allow us to use all the atoms in the measurement. With the challenge of rethermalization to be pursue and because in our system the main limitation of the evolution times is the short lifetime, a 2D-MOT would benefit the vacuum conditions, lifetime and therefore attainable rethermalization times. In addition, the production rates would be lowered below 10 s, with the benefit of increasing the quality of the statistics of our experiments.

A

RUBIDIUM 87 RELEVANT ENERGY TRANSITIONS

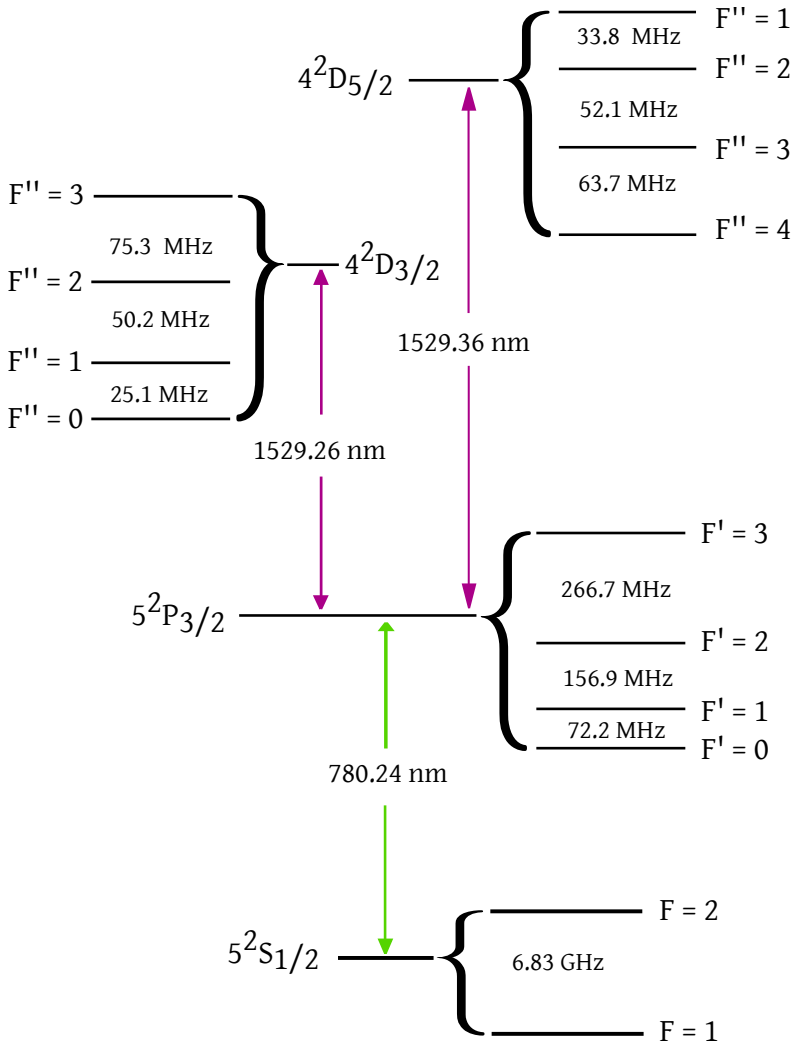

^{87}Rb structure. Data taken from [Steck, 2001; Lee et al., 2007; Noh and Moon, 2009; Safronova et al., 2004]

B

LASER DETUNINGS

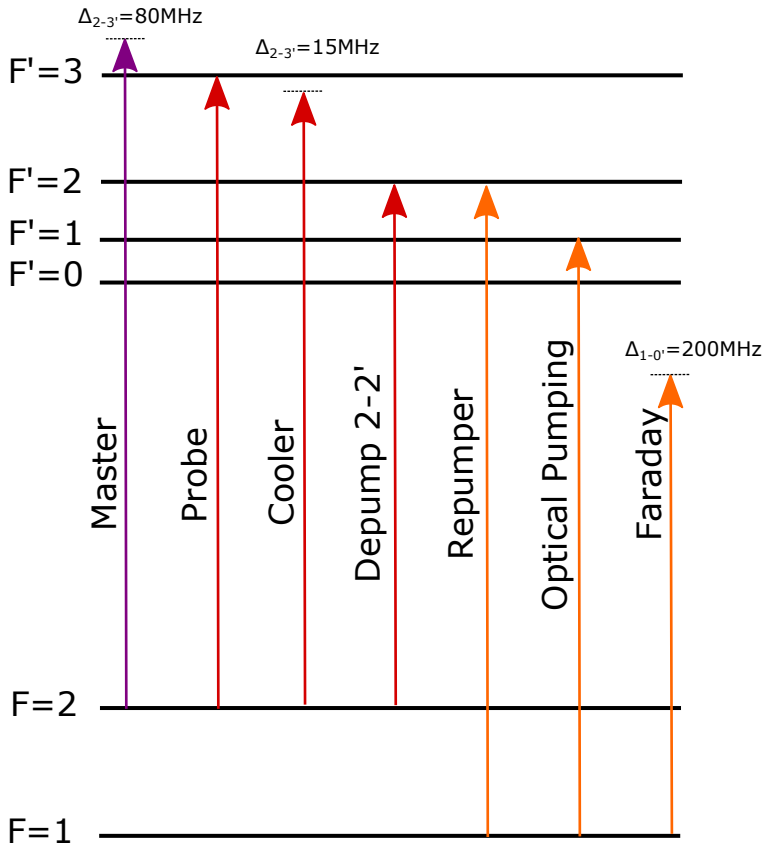

Different lasers used in the experiment and their detunings referenced to the ^{87}Rb D2 line.

C

CHAMBER

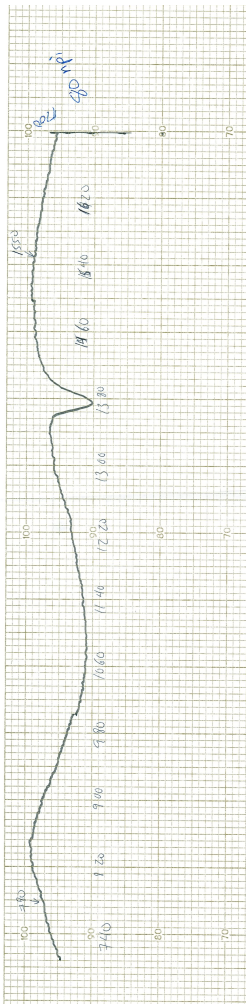

Measurement of the transmission through the glass cell sent by the manufacturer

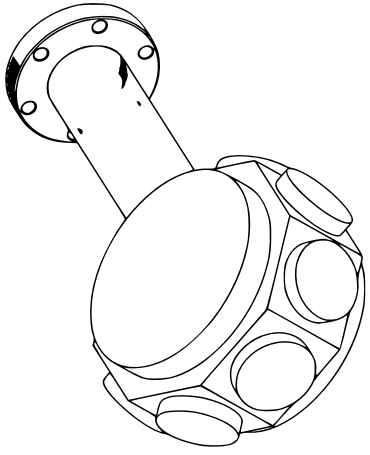

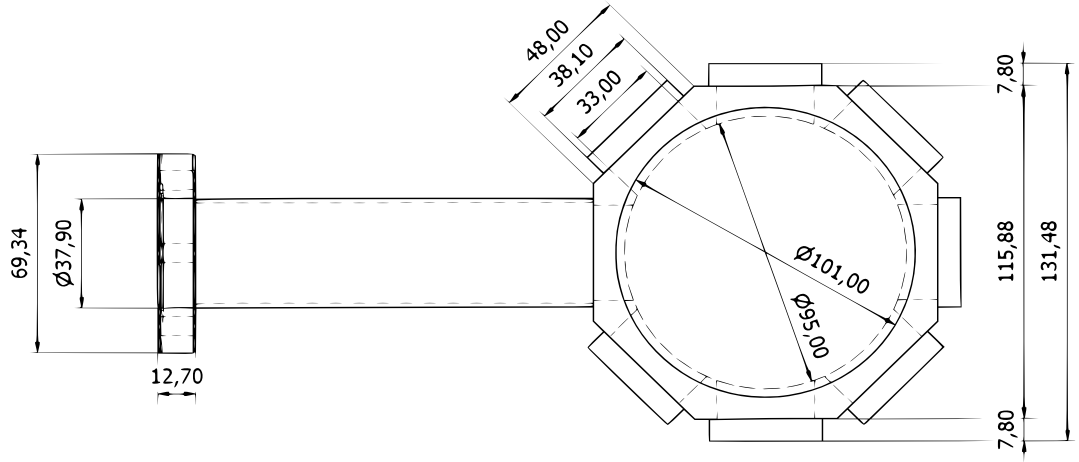

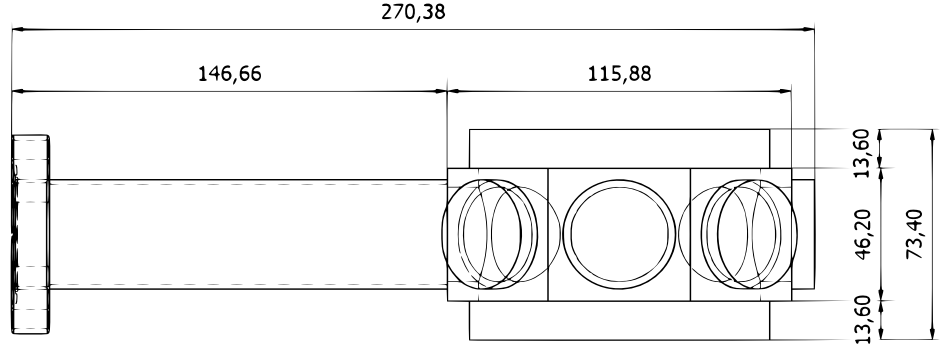

Diseño de	Revisado por	Aprobado por	Fecha	Fecha	
tvanderbruggen				20/03/2014	

glass_cell_octogonal_2-1	Edición	Hoja
		1 / 1

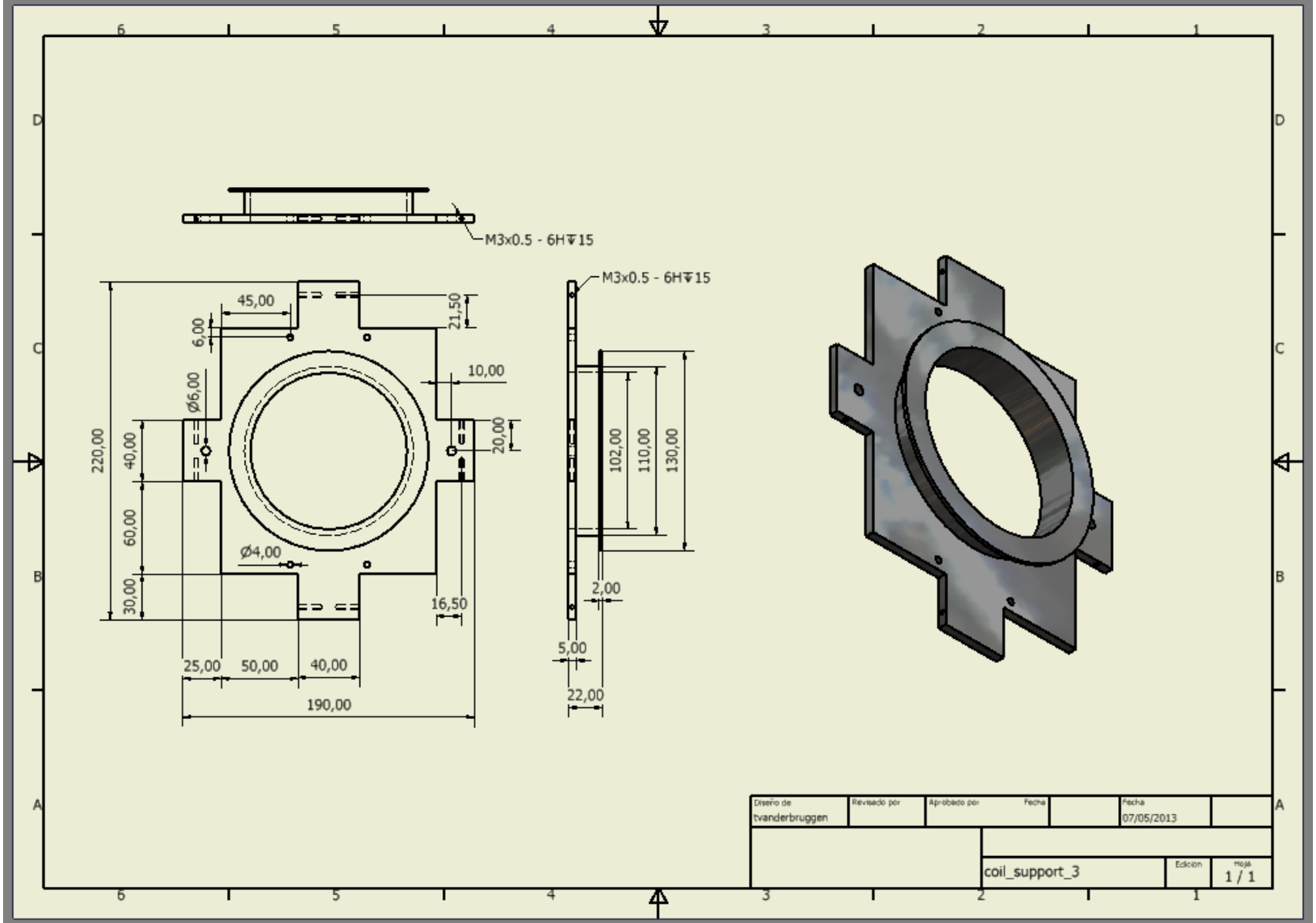
M3x0.5 - 6H↧15
45,00
6,00
21,50
10,00
Ø6,00
20,00
220,00
40,00
60,00
30,00
Ø4,00
16,50
25,00
50,00
40,00
190,00
M3x0.5 - 6H↧15
102,00
110,00
130,00
2,00
5,00
22,00
Diseño de
tvanderbruggen
Revisado por
Aprobado por
Fecha
Fecha
07/05/2013
coil_support_3
Edición
Hoja
1 / 1

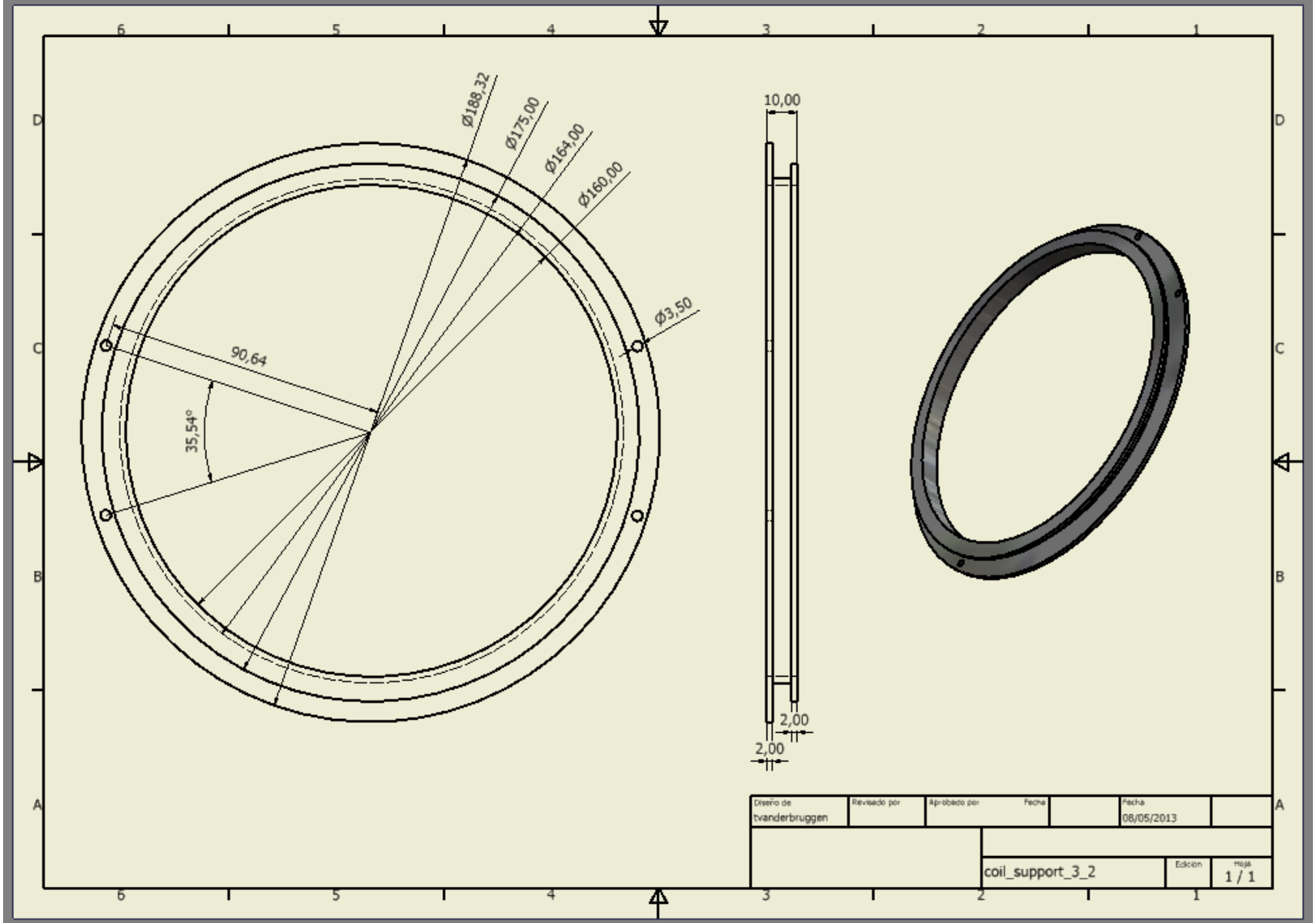
Ø188,32
Ø175,00
Ø164,00
Ø160,00
Ø3,50
90,64
35,54°
10,00
2,00
2,00
Diseño de
tvanderbruggen
Revisado por
Aprobado por
Fecha
Fecha
08/05/2013
coil_support_3_2
Edición
Hoja
1 / 1

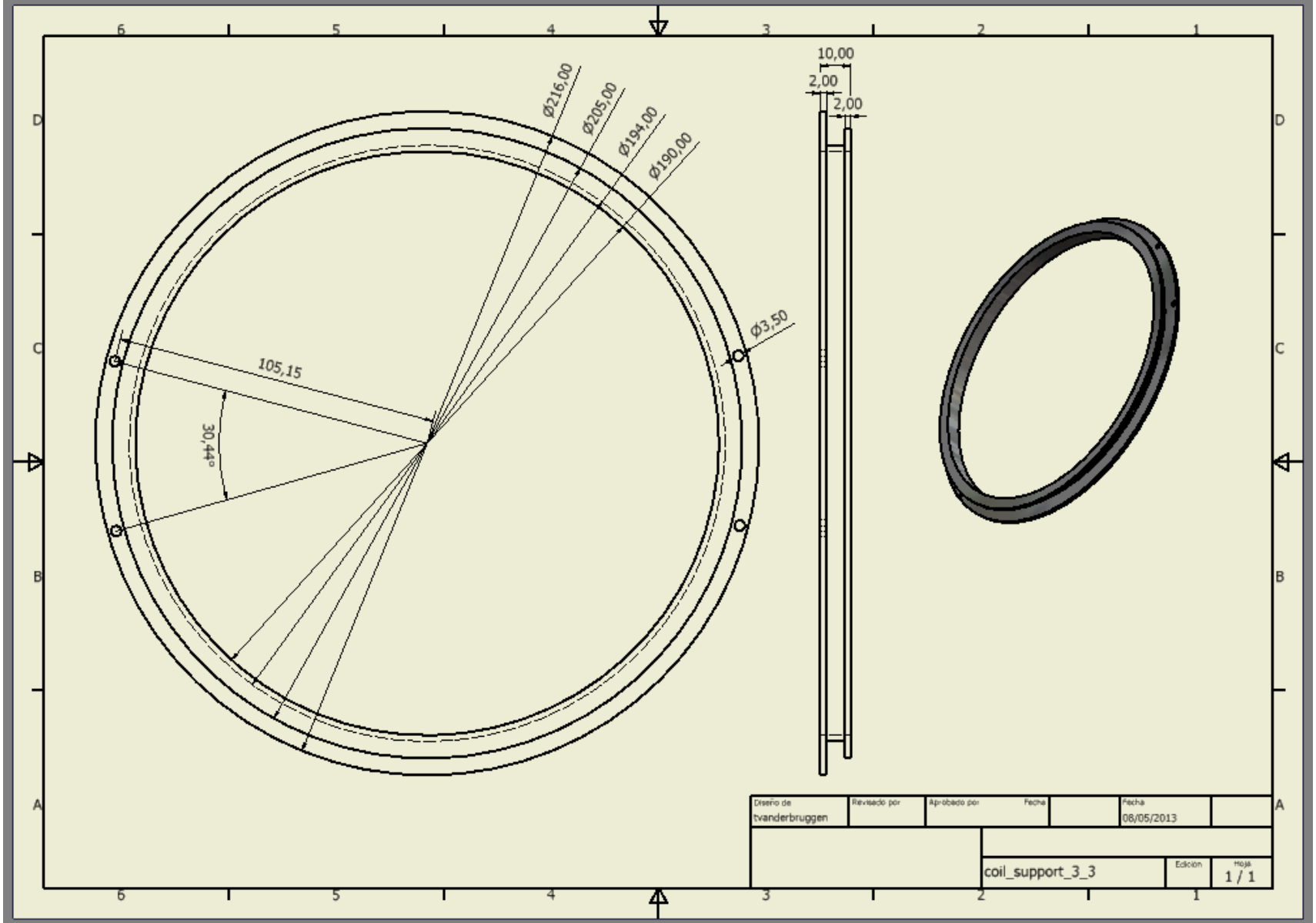
Ø216,00
Ø205,00
Ø194,00
Ø190,00
Ø3,50
105,15
30,44°
10,00
2,00
2,00
Diseño de
tvanderbruggen
Revisado por
Aprobado por
Fecha
Fecha
08/05/2013
coil_support_3_3
Edición
Hoja
1 / 1

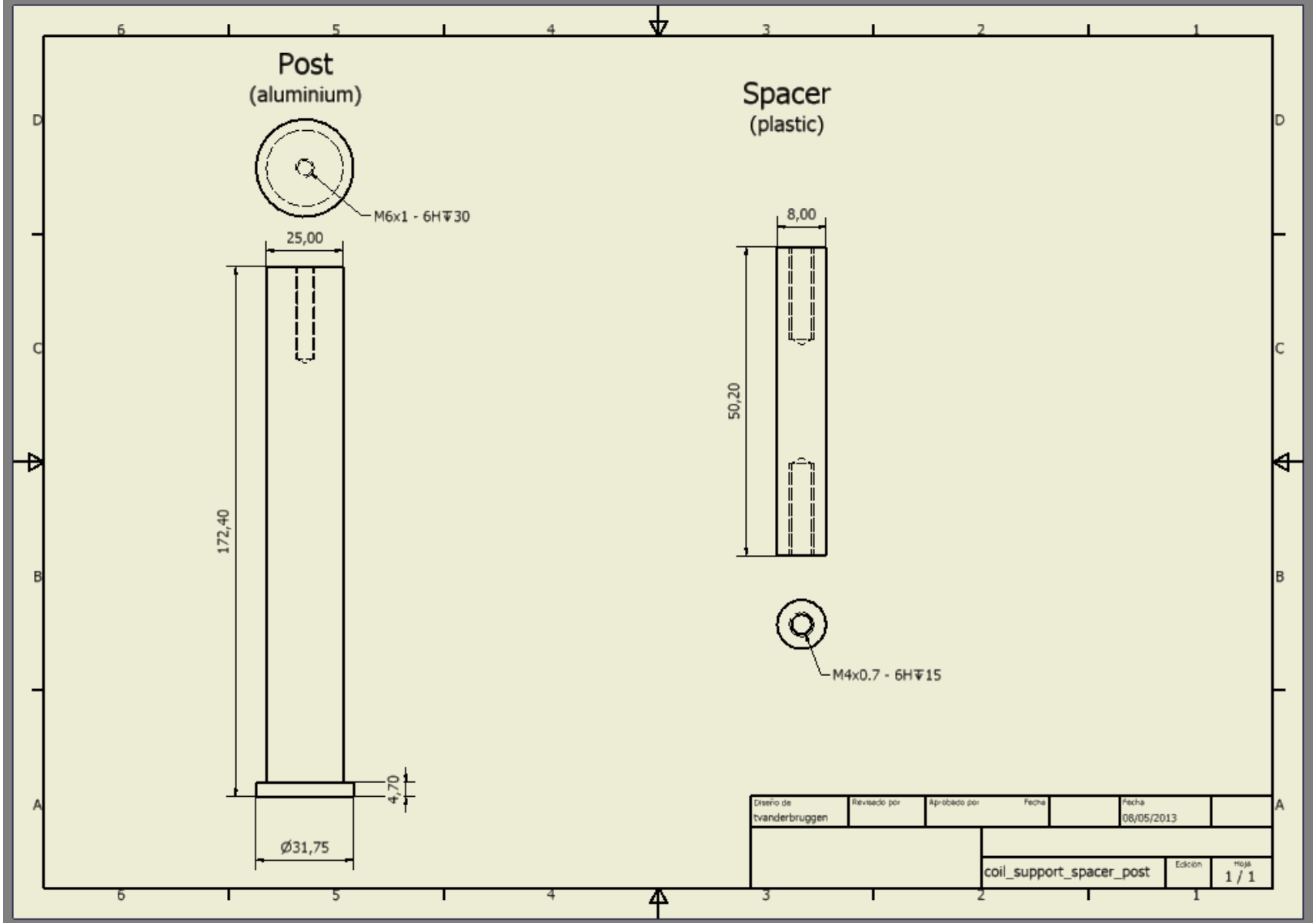
Post
(aluminium)
M6x1 - 6H↧30
25,00
172,40
4,70
Ø31,75
Spacer
(plastic)
8,00
50,20
M4x0.7 - 6H↧15
Diseño de
tvanderbruggen
Revisado por
Aprobado por
Fecha
Fecha
08/05/2013
coil_support_spacer_post
Edición
Hoja
1 / 1

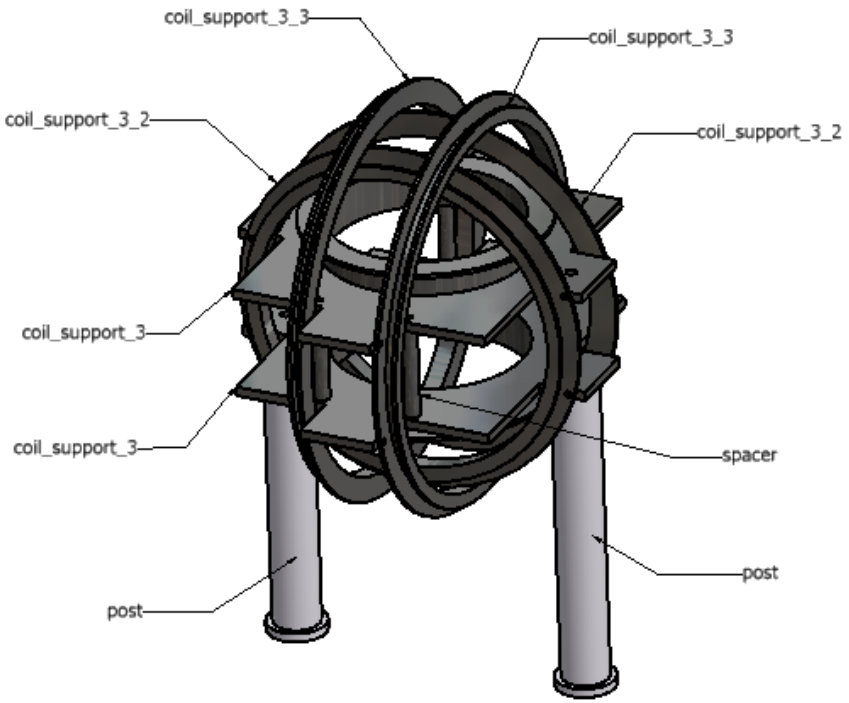

Diseño de	Revisado por	Aprobado por	Fecha	Fecha	
tvanderbruggen				08/05/2013	

assembly_coils_support	Edición	Hoja 1 / 1	

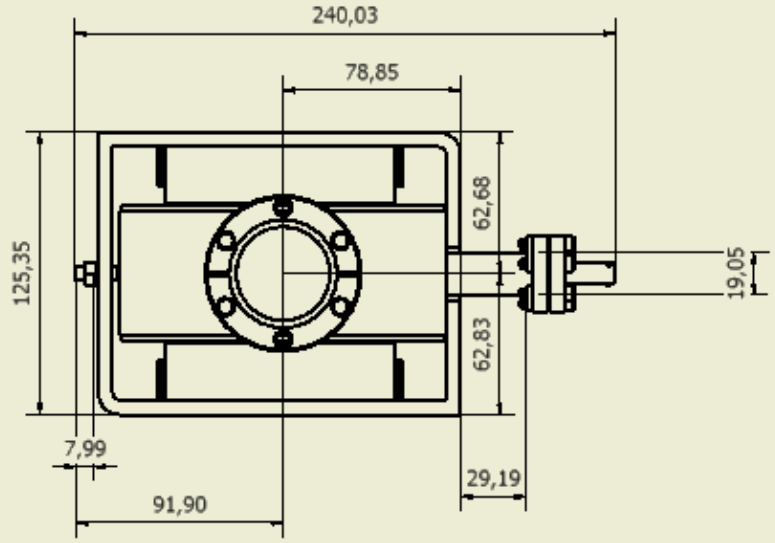

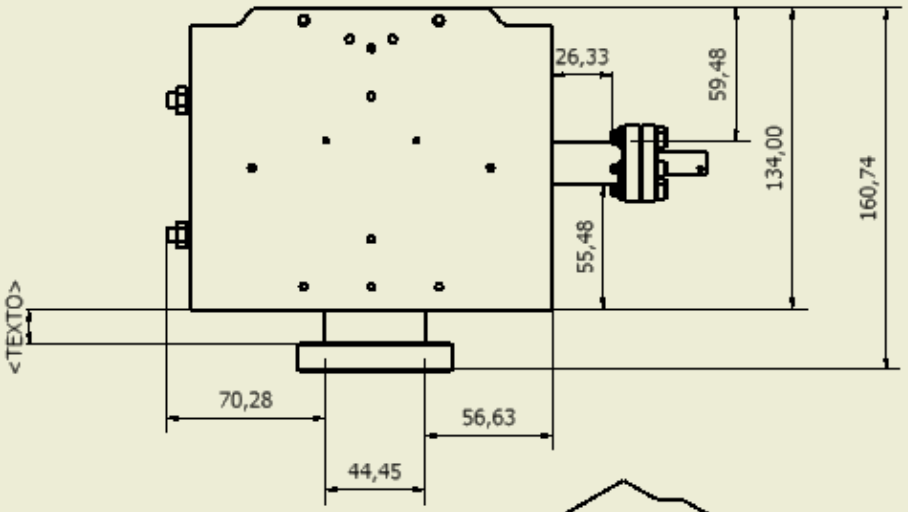

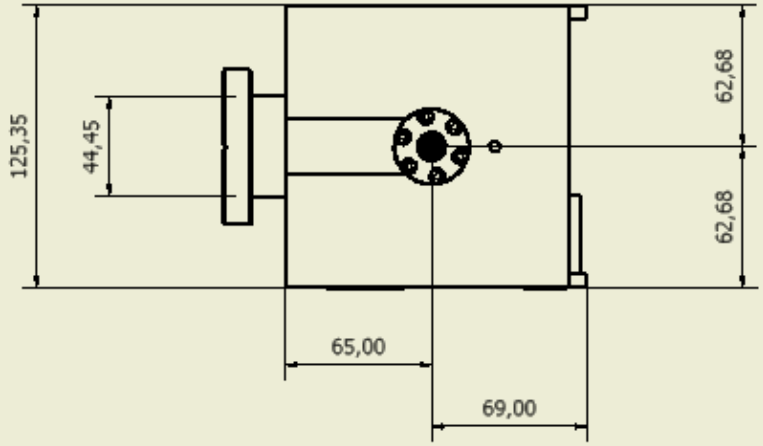

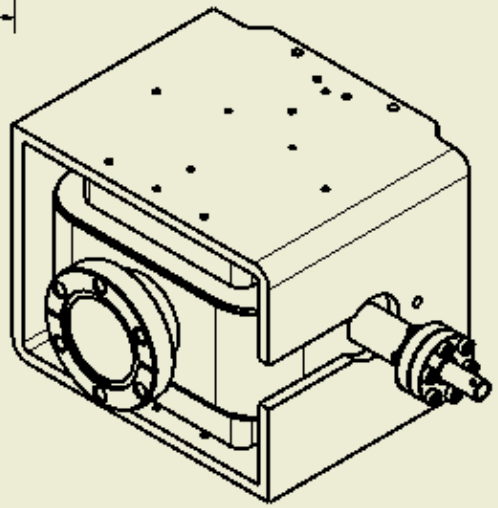

Diseño de	Revisado por	Aprobado por	Fecha	Fecha
spalacios				22/05/2013

25SW-XX-2H-SC_2	Edición	Hoja 1 / 1

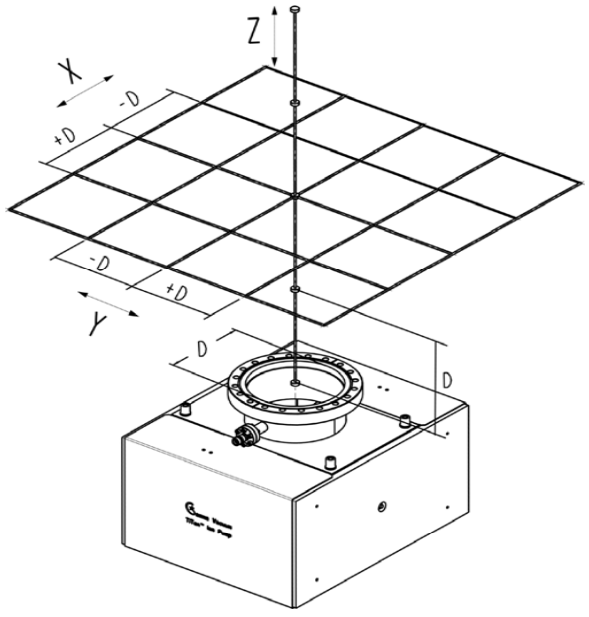

* Diagram for representation only and may not mimic pump style

Gamma Vacuum

Ion Pump Magnetic Field Data

Collected in accordance with ISO/DIN 28429

Ion Pump Style*: 25SVW
Flange: 2.75" CFF (NW35)
D: 1.50" (38.1 mm)
Data Units: Gauss

Z = 0		X				
		-2D	-D	0	D	2D
Y	-2D	3.884	4.249	1.630	1.568	2.137
	-D	6.466	12.151	9.913	6.634	3.716
	0	8.649	18.659	14.897	11.742	4.806
	D	7.163	12.306	7.629	7.984	4.080
	2D	5.256	5.184	2.422	3.043	3.290

Z = D		X				
		-2D	-D	0	D	2D
Y	-2D	1.849	1.640	0.854	0.900	0.787
	-D	2.545	2.903	1.392	0.989	1.122
	0	3.014	3.848	2.229	1.630	1.334
	D	2.846	3.006	1.220	1.067	1.315
	2D	2.211	2.142	1.208	1.024	1.276

Z = 2D		X				
		-2D	-D	0	D	2D
Y	-2D	1.296	0.911	0.670	0.616	0.538
	-D	1.356	1.048	0.509	0.489	0.608
	0	1.363	1.051	0.565	0.458	0.608
	D	1.489	1.212	0.547	0.509	0.616
	2D	1.417	1.288	0.927	0.707	0.640

Z = 3D		X				
		-2D	-D	0	D	2D
Y	-2D	0.927	0.707	0.616	0.489	0.489
	-D	0.927	0.640	0.547	0.458	0.424
	0	0.927	0.640	0.519	0.519	0.412
	D	0.994	0.761	0.616	0.509	0.400
	2D	1.004	0.927	0.610	0.519	0.412

Z = 4D		X				
		-2D	-D	0	D	2D
Y	-2D	0.866	0.748	0.538	0.509	0.441
	-D	0.787	0.670	0.509	0.447	0.458
	0	0.787	0.640	0.509	0.457	0.447
	D	0.860	0.640	0.583	0.447	0.447
	2D	0.860	0.781	0.583	0.458	0.458

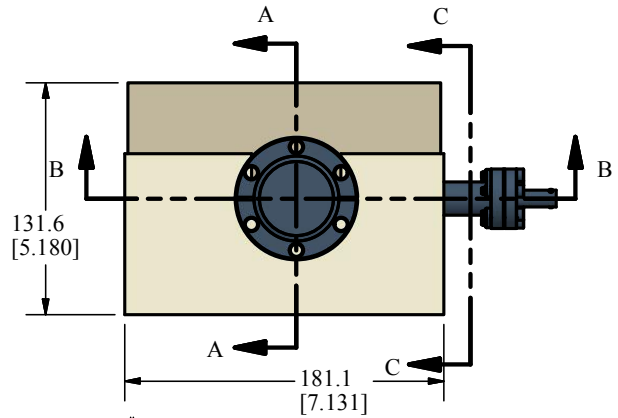

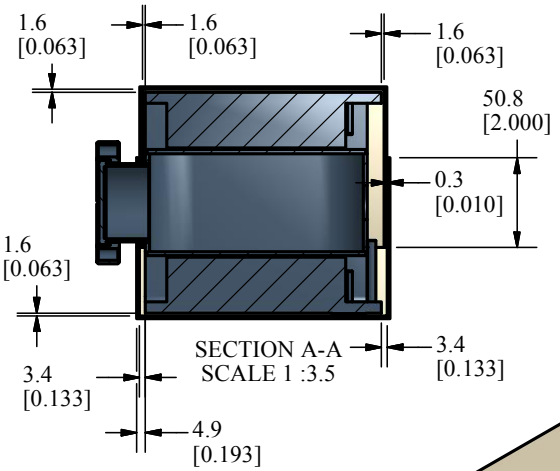

SECTION A-A
SCALE 1 :3.5

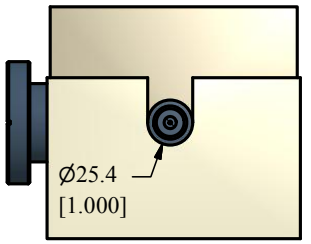

SECTION C-C
SCALE 1 :3.5

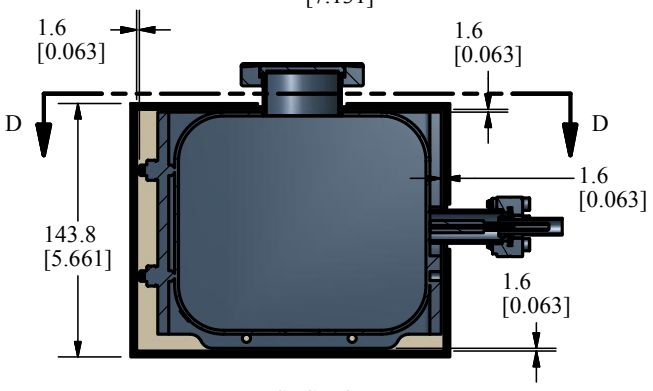

SECTION B-B
SCALE 1 :3.5

1. ION PUMP SHIELD ASSEMBLY
2. INSTALL NON-MAGNETIC SPACERS TO HOLD GAPS BETWEEN PUMP AND SHIELDS
3. INSTALL SCREWS TO HOLD ION PUMP SHIELD SIDE 1 AND SIDE 2 TOGETHER (SIZE, LOCATION AND QUANTITY TO BE DETERMINED BY PRODUCTION)

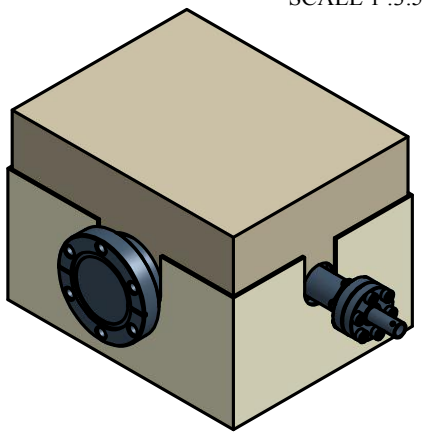

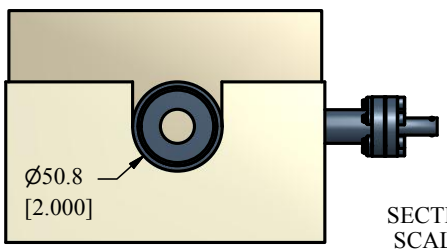

SECTION D-D
SCALE 1 :3.5

THE MUSHIELD COMPANY, INC

TITLE

ICFO
Ion Pump Magnetic Shield

Design Date: 6/11/13

SIZE		DWG NO	REV
A		ICFO-GVIP25SVW-TMC	D
SCALE	Dimensions: mm [in]	SHEET 2 OF 4	

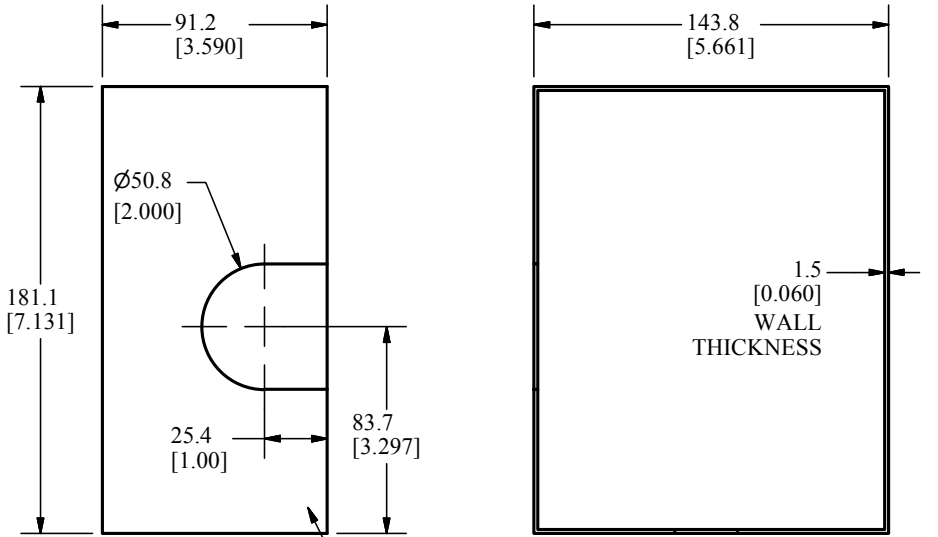

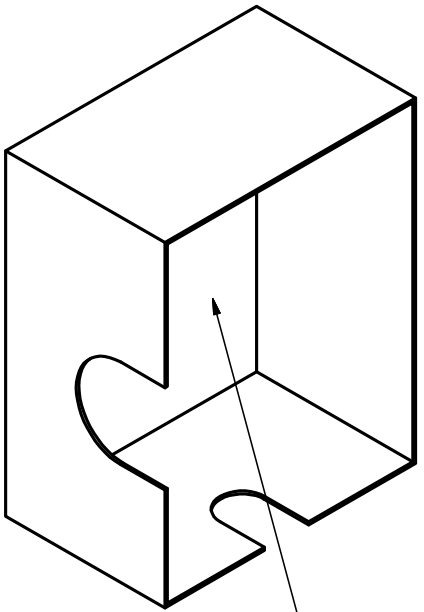

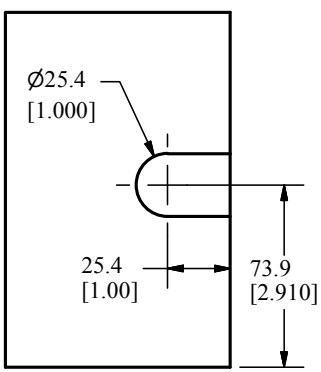

1. ION PUMP SHIELD SIDE 1
2. INSTALL NON-MAGNETIC SPACER ON BOTTOM OF SHIELD 1 TO HOLD 1/16" GAP BETWEEN SHIELD 1 AND SIDE OF ION PUMP
3. MATERIAL: HIGH PERMEABILITY COMP 1
4. THICKNESS: 0.060"
5. HEAT TREAT: 2050°F FOR 1 HOUR
6. 1 REQUIRED

THE MUSHIELD COMPANY, INC

TITLE

ICFO
Ion Pump Magnetic Shield Design Date: 6/11/13

SIZE		DWG NO	REV
A		ICFO-GVIP25SVW-TMC	D
SCALE	Dimensions: mm [in]	SHEET 3 OF 4	

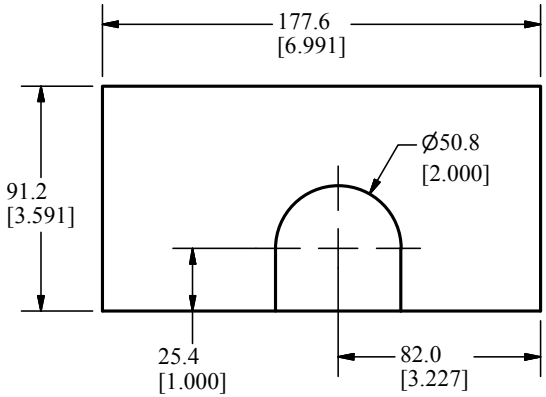

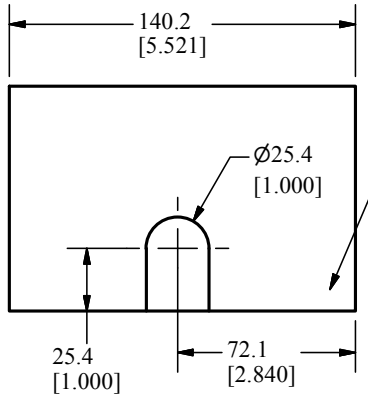

INSTALL SCREWS ON ALL SIDES
TO HOLD SHIELD 2 TO SHIELD 1
(SIZE, LOCATION AND QUANTITY
TO BE DETERMINED BY PRODUCTION)

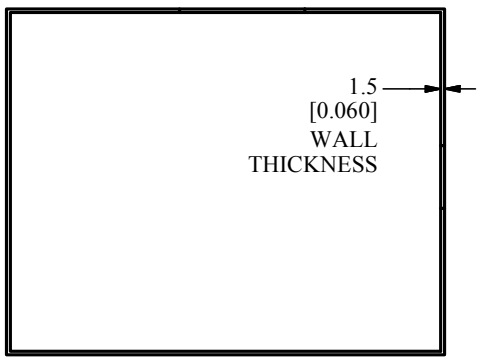

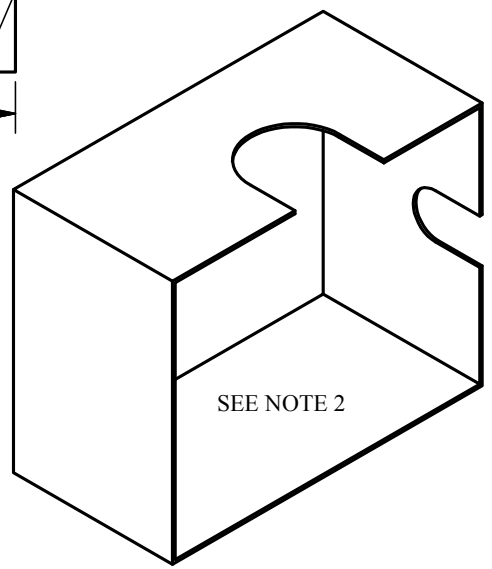

1. ION PUMP SHIELD SIDE 2
2. INSTALL NON-MAGNETIC SPACERS ON ALL SIDES TO HOLD 1/16" GAP BETWEEN SHIELD 1 AND SIDES OF ION PUMP
3. MATERIAL: HIGH PERMEABILITY COMP 1
4. THICKNESS: 0.060"
5. HEAT TREAT: 2050°F FOR 1 HOUR
6. 1 REQUIRED

THE MUSHIELD COMPANY, INC

TITLE
ICFO
Ion Pump Magnetic Shield Design Date: 6/11/13

SIZE		DWG NO	REV
A		ICFO-GVIP25SVW-TMC	D

SCALE | Dimensions: mm [in] | SHEET 4 OF 4

D

SPIN DYNAMICS IN A STOCHASTIC MODEL OF THE LABORATORY FIELD

In this chapter we will study the magnetic environment around the experiment and perform simulations of the atomic dynamics in the presence of such real magnetic field. This results will allow us to better understand the sensitivity measurements of the spinor magnetometer described in the last chapter.

Using a three-axis flux gate sensor (Mag-03 MCUP, Bartington) located next to the vacuum chamber we can measure the magnetic field in the three spatial directions at the same time. The noise of the instrument is $< 6\,\mathrm{pT/Hz^{1/2}}$ at 1 Hz in a full scale of $\pm 100\,\mu\mathrm{T}$.

Figure 77 shows one measurement of the magnetic field total amplitude. The mean value is $45.137 \pm 0.001\,\mu\mathrm{T}$, which mainly corresponds to the earth magnetic field. It also shows an oscillating component at the mains frequency (50 Hz) and its odd harmonics. We also show a fit of the form:

$$B(t) = B_{dc} + \sum_{n=0}^{2} B_{2n+1} \cos[2\pi 50(2n+1)t]. \tag{131}$$

A magnetic field that changes in time in a predictable way can not induce decoherence on the average over different preparations. Nevertheless, random fluctuations of the mean amplitude of the field and its oscillating components can. In order to measure possible fluctuations on the amplitudes we repeat the same measurement 100 times and make statistics on the fit parameters to each signal. To reproduce the typical conditions of the experiment we measure at the cycle rate of the experiment (every 40 s), always after synchronizing with the mains' cycle. The signals from the fluxgate are sent to an NI card with maximum acquisition rate of 1.25 MS/s. The results are summarized in Table 7.

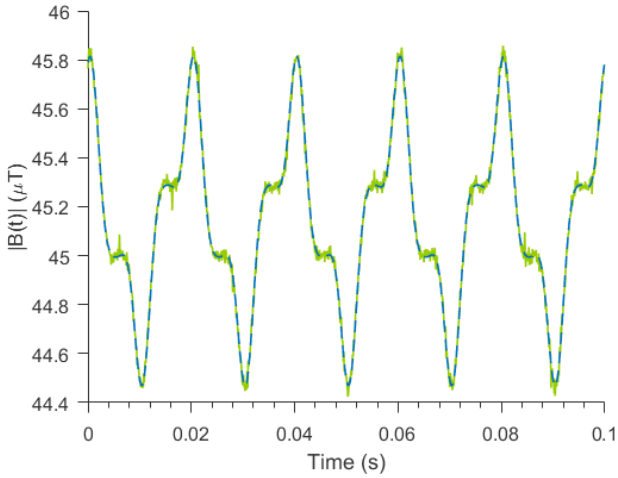

Figure 77: Measurement of the environment magnetic field amplitude using a three-direction flux-gate sensor. Data (green) is fitted with the function given in Equation 131.

In order to investigate the spin dynamics we compute the spin projection, as given in Equation 32, where the magnetic field is given by $B(t) = B_{dc} + B_{50}\cos(2\pi 50t) + B_{150}\cos(2\pi 150t)$. The coefficients of the oscillatory terms are the measured amplitudes. We neglect the fifth harmonic component which is much weaker than the rest. The random fluctuations of these oscillatory components are included in each coefficient adding a random component obtained from a Gaussian distribution of width $\sigma_{B_{50,150}}$

mean amplitude (nT)	standard deviation (nT)
$B_{dc} = 45.15 \times 10^3$	$\sigma_{dc} = 20$
$B_{50} = 439$	$\sigma_{50} = 5$
$B_{150} = 209$	$\sigma_{150} = 2$
$B_{250} = 37$	$\sigma_{250} = 1$

Table 7: Measurement results of the magnetic field environment . The measurements were performed with a fluxgate sensor located 20 cm away from the atoms.

as given by the measured values. Because during the experiment we compensate the mean magnetic field and set a bias along **z**, we assume the constant mean field is only that given by the set bias $B_{dc} = B_z = 28.6\,\mu T$. The noise on this DC component is included through σ_{dc} in the same manner as for the oscillating terms.

For the initial conditions $\langle \hat{F}^i_x \rangle = F_x$ and $\langle \hat{F}^i_{z,y} \rangle = 0$ the spin operator $\hat{F}_x$ is expected to be frequency modulated due the oscillating part of $B(t)$ and amplitude modulated due to the quadratic Zeeman interaction. One example of the spin evolution is shown in Figure 78.

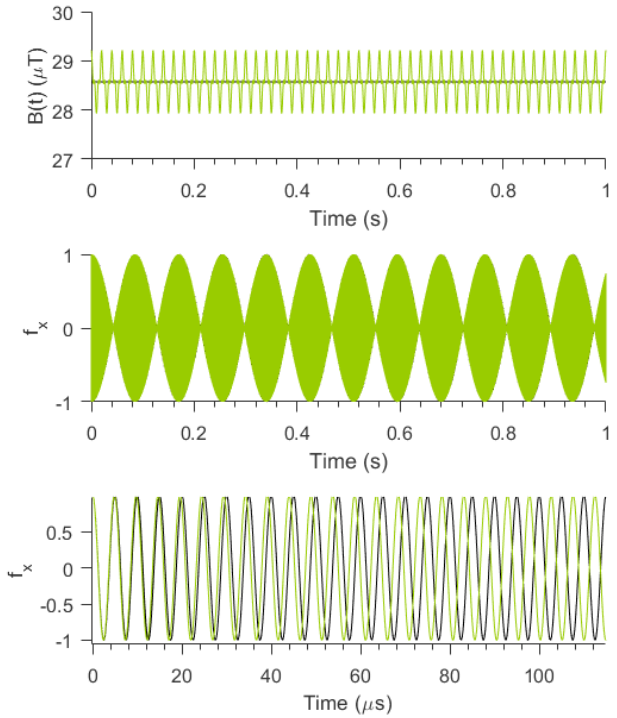

Figure 78: Top figure shows the magnetic field constant (black) and that with a 50 Hz and 150 Hz variation (green) to simulate the measured environment. The lower two figures show the spin projection on the axis **x** in a long and a short time scale, respectively to show the amplitude modulation cased by the quadratic Zeeman shift, and the fast Larmor precession.

The average over many preparations with random noise in the field amplitude induces variations in the relative phase. To quantify this variance we generate 300 signals with amplitude fluctuations as described above and compute the variance of the phase after a time evolution $t = 20\,\mu s$. For the measured fluctuation of the field without compensation $\sigma_{dc} = 20\,nT$, the variance is $\mathrm{var}\,(\Theta_L(t = 20\,\mu s)) = 3 \times 10^{-4}\,rad^2$.

Since the compensation fields may also contribute to widen the random noise distribution, we study the noise scaling in terms of the total width σ_{B_z}. The results are shown in Figure 79 where we can appreciate that the variance in the phase rises to the $\simeq 3 \times 10^{-3}\,rad^2$ for $\sigma_{B_z} = 60\,nT$, which is the noise of the spinor magnetometer we have reported in Section 9.4.

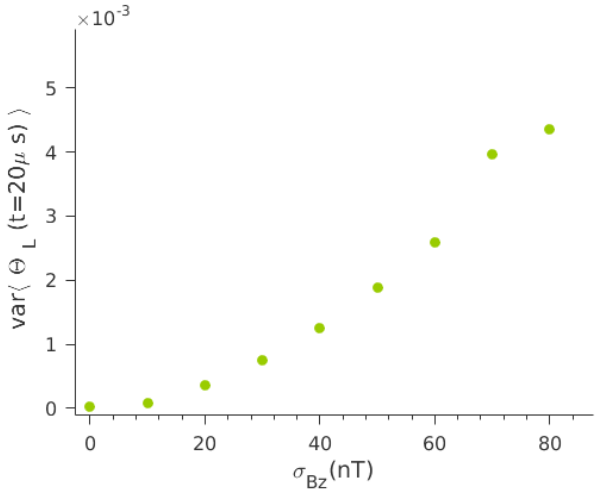

Figure 79: Variance of Θ_L (rad^2) after 20 µs of evolution time as a function of the DC noise fluctuations. The mean amplitude of the magnetic field is $B_z = 28.6\,\mu T$. The noise in the amplitude of B is modeled with a random Gaussian distribution of width σ_{B_z} in the DC part. Also contributions at 50 Hz and 150 Hz are included with amplitudes and noise widths measured for the ambient noise (see Table 7).

These estimations suggest that the limited sensitivity of the magnetometer could be entirely caused by the random fluctua-

tions in the amplitude of the ambient and compensating magnetic field even at very short time scales.

A BIT OF HISTORY FOR THE CURIOUS: FUNNY AND TOUGH MOMENTS

At the end of 2011 I joined Morgan's group as a master student. While taking the courses of the master I spent a few months in the old cold atom experiment (not quite working in the main experiment, of course) before I could start building the new lab.

When the new lab was finally available and freshly painted I started to design the lab distribution and buy the first equipment we were going to need. The first project was the construction of the master clock, which was completed and characterized soon in 2012. I presented it as my master thesis in the summer that year.

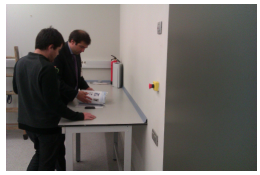

Mid-2012, before the non-magnetic optical tables arrived, our post-doc Thomas joined the group, we founded then the team Atom 2.0. Thomas and I started the design of the laser and vacuum system for the MOT. We decided to build a small experiment which could be eventually shielded. Back then, we were not sure we could achieve condensation without a 2D MOT, but it was worth trying, so we left some space to include one in case it was necessary in the future.

While preparing the vacuum, at the end of 2012 our post-doc Natali joined the group. That was great, 66% of the team was female! Anyways, we soon achieved 1×10^{-11} Torr *in the glass cell and could start filling the cell with Rubidium. We first activated the dispenser with both isotopes, but soon decided we would only use the* ^{87}Rb *enriched dispenser from then on.*

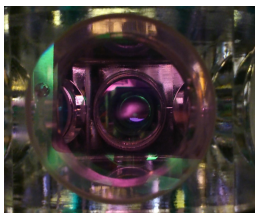

Later, Simon set up the control of the experiment and soon we could observe our first fluorescence signal of the MOT. He joined as a PhD student until late 2013 in shared-time with a group in Lens.

We were working on various projects including the non-degenerate MTS, but we all wanted to keep going ahead towards the condensate so we quickly set up the optics for the ODT.

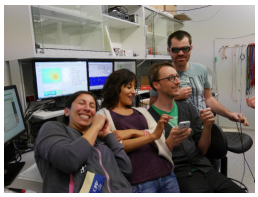

In February of 2013 we successfully transferred the atoms of the MOT into the ODT for the first time. We improved the efficiency of the loading and added the second arm and a dimple beam, which was going to be used at the end of the forced all-optical evaporation to compensate the relaxation of the potential. As soon as we got a few million atoms in the trap we started trying evaporation ramps and got to the sub micro Kelvin regime but with no sign of condensed fraction. We tried for a long time to make it work but it didn't, regardless the models and simulation that predicted that for our particular experimental conditions, condensation was achievable.

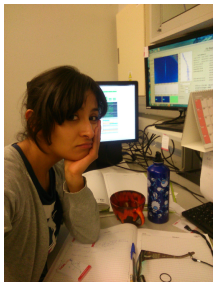

In 2014 Natali was working on the paper on the MTS for frequency references at telecom wavelengths and Thomas on another one about the spontaneous PT symmetry breaking in a spinor condensate. That year both decided to move for different reasons, she wanted to comeback with her family to the States and Thomas got a position in the UK. At that period also Simon left for one year to Lens and I was left alone. Any person that has ever work in a cold atom experiment knows being alone in the lab is the worst thing that can happen.

In the mean time Morgan tried to find new people to join the experiment and I spent my time trying to find potential causes of the failure, It was weird we were losing the atoms almost right after crossing one micro Kelvin. Most people suggested that the problem was that we didn't have enough atoms from the beginning so we decided to buy another amplifier to make a deeper and more robust ODT. It was very simple,

same company, same design, it could be shipped in three months... It wasn't. After six months waiting for the laser the company finally sent it. Just after switching it on it burned. We sent it back for repairing and when it was back it burned again the first day. The company had to change a lot in the mechanics to make it work, which took a total time of one year #honestly. That amplifier is just bad, is dying day to day and never quite gave all the power we requested. The first amplifier in contrast is great, five years working at full power with no problems. So weird.

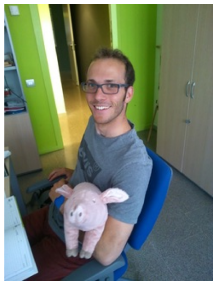

In 2015 our post-doc Martijn joined the team. Simon was also back. Not much later PhD student Pau also joined the team. Many things in the lab were improved thanks to them. With a new fresh Atoms 2.0 team (maybe better to call it Atoms 2.0.1) we set up the Faraday probe, the new ODT and started trying evaporation ramps again. In that period we realized there was a problem of RF contamination, we noticed it especially in the lock of the lasers, the instability was causing failures in our atom manipulation sequence. One day it was particularly lucky, we were not running the sequence but the MOT was on; that day the signal was so strong or simply better coupled to our cooler laser, that the MOT was dying at a constant rate: every 40 s. That sounded like a cold atom experiment cycle.... The powerful RF source of the experiment next door was getting into all our electronics.

Martijn built many dipole and loop antennas and an RF power meter box to monitor the RF contamination at different points in the lab. We tried to filter the signal everywere but that didn't improve much. Several technicians came to try to solve the problem which resulted to be far from trivial. They finally installed many layers of metallic clothing around the experiment next door and between the labs to shield our experiment.

In July 2016 Martijn got a good position in Australia. We arrange a farewell in the traditional way: all the group together went for lunch to the beach. That always relaxes and clears your mind (just saying, Morgan). When we came back, I decided to add the auxiliary third beam of the ODT we had considered in the new design but had not used yet. The beam was weak and the atoms were escaping through the arms so I just reduced the waist inserting a telescope I had around. After the change, the first ramp I tried finally gave me a double structure: the condensate.

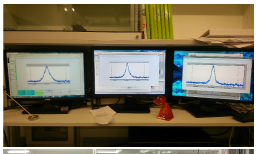

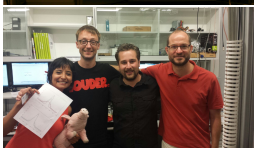

I called all the others, It was so exciting, a very strong emotion that after so long we finally got it. I'm happy Martijn could see it before leaving, I wish Thomas and Natali had had that fortune.

After that day we worked trying to improve the number of atoms in the condensate. Pau implemented the simplex to find the most effective evaporation ramp that gave us from 50 to 100 thousand atoms in the condensate. We started performing non-destructive measurements of the spin state and characterized the spinor magnetometer. After this I dedicated full time to write this thesis. My time was over but now is the time for Simon, Pau and the many new generations to come. I hope this experiment grows and brings many answers to questions about ferromagnetism, the limits on field sensing and many other topics the new members desire to explore.

PS. Yes the pig is always around, is our pet.

BIBLIOGRAPHY

A. Abragam. *The principles of nuclear magnetism*. Oxford University Press, 1961.

Sanjar M. Abrarov and Brendan M. Quine. sep 2014.

M. H. Anderson, J. R. Ensher, M. R. Matthews, C. E. Wieman, and E. A. Cornell. Observation of Bose-Einstein Condensation in a Dilute Atomic Vapor. *Science*, 269(5221):198–201, 1995. ISSN 0036-8075. doi: 10.1126/science.269.5221.198. URL http://science.sciencemag.org/content/269/5221/198.

Jurgen Appel, Andrew MacRae, and A I Lvovsky. A versatile digital GHz phase lock for external cavity diode lasers. *Meas. Sci. Technol.*, 20:055302, 2009.

K.J. Arnold and M.D. Barrett. All-optical Bose-Einstein condensation in a 1.06 um dipole trap. *Optics Communications*, 284(13): 3288, 2011. URL http://www.sciencedirect.com/science/article/pii/S0030401811002793.

T. Arpornthip, C. A. Sackett, and K. J. Hughes. Vacuum-pressure measurement using a magneto-optical trap. *Phys. Rev. A*, 85: 033420, 2012.

A. Aspect, E. Arimondo, R. Kaiser, N. Vansteenkiste, and C. Cohen-Tannoudji. Laser Cooling below the One-Photon Recoil Energy by Velocity-Selective Coherent Population Trapping. *Phys. Rev. Lett.*, 61:826–829, Aug 1988. doi: 10.1103/PhysRevLett.61.826. URL http://link.aps.org/doi/10.1103/PhysRevLett.61.826.

M. D. Barrett, J. A. Sauer, and M. S. Chapman. All-Optical Formation of an Atomic Bose-Einstein Condensate. *Phys. Rev. Lett.*, 87:010404, Jun 2001. doi: 10.1103/PhysRevLett.87.010404. URL http://link.aps.org/doi/10.1103/PhysRevLett.87.010404.

N. Behbood, F. Martin Ciurana, G. Colangelo, M. Napolitano, M. W. Mitchell, and R. J. Sewell. Real-time vector field tracking with a cold-atom magnetometer. *Applied Physics Letters*, 102 (17):173504, 2013. doi: 10.1063/1.4803684. URL http://dx.doi.org/10.1063/1.4803684.

Jacob D. Bekenstein. Entropy content and information flow in systems with limited energy. *Phys. Rev. D*, 30(8):1669–1679, october 1984.

William E. Bell and Arnold L. Bloom. Optically Driven Spin Precession. *Phys. Rev. Lett.*, 6:280–281, Mar 1961. doi: 10.1103/PhysRevLett.6.280. URL http://link.aps.org/doi/10.1103/PhysRevLett.6.280.

Simon Bernon. *Piégeage et mesure non-destructive d'atomes froids dans une cavité en anneau de haute finesse*. PhD thesis, 2011. URL http://www.theses.fr/2011EPXX0034;http://www.theses.fr/2011EPXX0034/document. Thèse de doctorat dirigée par Bouyer, Philippe Physique Palaiseau, Ecole polytechnique 2011.

N. N. Bogolyubov. On the theory of superfluidity. *J. Phys.(USSR)*, 11:23–32, 1947. [Izv. Akad. Nauk Ser. Fiz.11,77(1947)].

G. Boyd and D Kleinman. Parametric Interaction of Focused Gaussian Light Beams. *J. Appl. Phys.*, 39(8):3597, 1968.

J. P. Brantut, J. F. Clément, M. Robert de Saint Vincent, G. Varoquaux, R. A. Nyman, A. Aspect, T. Bourdel, and P. Bouyer. Light-shift tomography in an optical-dipole trap for neutral atoms. *Phys. Rev. A*, 78:031401, Sep 2008. doi: 10.1103/PhysRevA.78.031401. URL https://link.aps.org/doi/10.1103/PhysRevA.78.031401.

J. B. Brask, R. Chaves, and J. Kołodyński. Improved Quantum Magnetometry beyond the Standard Quantum Limit. *Phys. Rev. X*, 5:031010, Jul 2015. doi: 10.1103/PhysRevX.5.031010. URL https://link.aps.org/doi/10.1103/PhysRevX.5.031010.

G. Breit and I. I. Rabi. Measurement of Nuclear Spin. *Phys. Rev.*, 38:2082–2083, Dec 1931. doi: 10.1103/PhysRev.38.2082.2. URL http://link.aps.org/doi/10.1103/PhysRev.38.2082.2.

D. M. Brink and C. V. Sukumar. Majorana spin-flip transitions in a magnetic trap. *Phys. Rev. A*, 74:035401, Sep 2006. doi: 10.1103/PhysRevA.74.035401. URL http://link.aps.org/doi/10.1103/PhysRevA.74.035401.

D Budker and M Romalis. Optical magnetometry. *Nature Phys.*, 3:227–234, 2007. ISSN 1745-2473. doi: 10.1038/nphys566.

E. A. Burt, R. W. Ghrist, C. J. Myatt, M. J. Holland, E. A. Cornell, and C. E. Wieman. Coherence, Correlations, and Collisions: What One Learns about Bose-Einstein Condensates from Their Decay. *Phys. Rev. Lett.*, 79:337–340, Jul 1997. doi: 10.1103/PhysRevLett.79.337. URL http://link.aps.org/doi/10.1103/PhysRevLett.79.337.

Eugene I. Butikov. Parametric excitation of a Linear Oscillator. *Eur. J. Phys*, 25:535–554, 2004.

G Camy, C J Bord, and M Ducloy. Heterodyne saturation spectroscopy through frequency modulation of the saturating beam. *Opt. Comm.*, 41(5):325, 1982.

Y. Castin and R. Dum. Bose-Einstein Condensates in Time Dependent Traps. *Phys. Rev. Lett.*, 77:5315–5319, Dec 1996. doi: 10.1103/PhysRevLett.77.5315. URL http://link.aps.org/doi/10.1103/PhysRevLett.77.5315.

M.-S. Chang, C. D. Hamley, M. D. Barrett, J. A. Sauer, K. M. Fortier, W. Zhang, L. You, and M. S. Chapman. Observation of Spinor Dynamics in Optically Trapped ^{87}Rb Bose-Einstein Condensates. *Phys. Rev. Lett.*, 92:140403, Apr 2004. doi: 10.1103/PhysRevLett.92.140403. URL https://link.aps.org/doi/10.1103/PhysRevLett.92.140403.

Ming-Shien Chang, Qin Qishu, Zhang Wenxian, You Li, and Chapman Michael S. Coherent spinor dynamics in a spin-1 Bose condensate. *Nat Phys*, 1(2):111–116, nov 2005. ISSN 1745-2473. doi: 10.1038/nphys153. 10.1038/nphys153.

Steven Chu. Nobel Lecture: The manipulation of neutral particles. *Rev. Mod. Phys.*, 70:685–706, Jul 1998. doi: 10.1103/RevModPhys.70.685. URL http://link.aps.org/doi/10.1103/RevModPhys.70.685.

Andreas Chwala, Ronny Stolz, Matthias Schmelz, Vyacheslav Zakosarenko, Matthias Meyer, and Hans-Georg Meyer. SQUID Systems for Geophysical Time Domain Electromagnetics (TEM) at IPHT Jena. *IEICE Transactions on Electronics*, E98.C (3):167–173, 2015. doi: 10.1587/transele.E98.C.167.

J. I. Cirac, M. Lewenstein, K. Mølmer, and P. Zoller. Quantum superposition states of Bose-Einstein condensates. *Phys. Rev. A*, 57:1208–1218, Feb 1998. doi: 10.1103/PhysRevA.57.1208. URL https://link.aps.org/doi/10.1103/PhysRevA.57.1208.

F. Martin Ciurana, G. Colangelo, Robert J. Sewell, and Morgan W. Mitchell. Real-time shot-noise-limited differential photodetection for atomic quantum control. *Opt. Lett.*, 41(13): 2946–2949, Jul 2016. doi: 10.1364/OL.41.002946. URL http://ol.osa.org/abstract.cfm?URI=ol-41-13-2946.

J.-F. Clément, J.-P. Brantut, M. Robert-de Saint-Vincent, R. A. Nyman, A. Aspect, T. Bourdel, and P. Bouyer. All-optical runaway evaporation to Bose-Einstein condensation. *Phys. Rev. A*, 79:061406, Jun 2009. doi: 10.1103/PhysRevA.79.061406. URL http://link.aps.org/doi/10.1103/PhysRevA.79.061406.

Claude N. Cohen-Tannoudji. Nobel Lecture: Manipulating atoms with photons. *Rev. Mod. Phys.*, 70:707–719, Jul 1998. doi: 10.1103/RevModPhys.70.707. URL http://link.aps.org/doi/10.1103/RevModPhys.70.707.

Giorgio Colangelo, Robert J Sewell, Naeimeh Behbood, Ferran Martin Ciurana, Gil Triginer, and Morgan W Mitchell. Quantum atom–light interfaces in the Gaussian description for spin-1 systems. *New Journal of Physics*, 15(10):103007, 2013. URL http://stacks.iop.org/1367-2630/15/i=10/a=103007.

Giorgio Colangelo, Ciurana Ferran Martin, Bianchet Lorena C., Sewell Robert J., and Mitchell Morgan W. Simultaneous

tracking of spin angle and amplitude beyond classical limits. *Nature*, 543(7646):525–528, mar 2017. ISSN 0028-0836. doi: 10.1038/nature21434.

Simon Coop, Silvana Palacios, Pau Gomez, Y. Natali Martinez de Escobar, Thomas Vanderbruggen, and Morgan W. Mitchell. Strong light shifts from near-resonant and polychromatic fields: comparison of Floquet theory and experiment. *arXiv:1702.02802 [physics.atom-ph]*.

Franco Dalfovo, Stefano Giorgini, Lev P. Pitaevskii, and Sandro Stringari. Theory of Bose-Einstein condensation in trapped gases. *Rev. Mod. Phys.*, 71:463–512, Apr 1999. doi: 10.1103/RevModPhys.71.463. URL http://link.aps.org/doi/10.1103/RevModPhys.71.463.

H. B. Dang, A. C. Maloof, and M. V. Romalis. Ultrahigh sensitivity magnetic field and magnetization measurements with an atomic magnetometer. *Applied Physics Letters*, 97(15):151110, 2010. doi: 10.1063/1.3491215. URL http://link.aip.org/link/?APL/97/151110/1.

J. W. Dawson, N. Park, and K. J. Vahala. An improved delayed self-heterodyne interferometer for linewidth measurements. *IEEE Photon. Technol. Lett.*, 4(9):1063–1066, 1992.

S. R. de Echaniz, M. Koschorreck, M. Napolitano, M. Kubasik, and M. W. Mitchell. Hamiltonian design in atom-light interactions with rubidium ensembles: A quantum-information toolbox. *Phys. Rev. A*, 77:032316, Mar 2008. doi: 10.1103/PhysRevA.77.032316. URL http://link.aps.org/doi/10.1103/PhysRevA.77.032316.

Y. Natali Martinez de Escobar, Silvana Palacios Álvarez, Simon Coop, Thomas Vanderbruggen, Krzysztof T. Kaczmarek, and Morgan W. Mitchell. Absolute frequency references at 1529 and 1560 nm using modulation transfer spectroscopy. *Opt. Lett.*, 40(20):4731–4734, Oct 2015. doi: 10.1364/OL.40.004731. URL http://ol.osa.org/abstract.cfm?URI=ol-40-20-4731.

Cornell University Library/Research Department. Digital imaging tutorial, 2014. URL https://www.library.cornell.edu/preservation/tutorial/conversion/conversion-05.html.

E. A. Donley, E. Hodby, L. Hollberg, and J. Kitching. Demonstration of high-performance compact magnetic shields for chip-scale atomic devices. *Review of Scientific Instruments*, 78(8): 083102, 2007. doi: 10.1063/1.2767533. URL http://dx.doi.org/10.1063/1.2767533.

L.-M. Duan, J. I. Cirac, and P. Zoller. Quantum entanglement in spinor Bose-Einstein condensates. *Phys. Rev. A*, 65:033619, Feb 2002. doi: 10.1103/PhysRevA.65.033619. URL https://link.aps.org/doi/10.1103/PhysRevA.65.033619.

M. Ducloy and D. Bloch. Theory of degenerate four-wave mixing in resonant Doppler-broadened systems - I. Angular dependence of intensity and lineshape of phase-conjugate emission. *J. Physique*, 42(5):711–721, 1981.

M. Ducloy and D. Bloch. Theory of degenerate four-wave mixing in resonant Doppler-broadened media. - II. Doppler-free heterodyne spectroscopy via collinear four-wave mixing in two- and three-level systems. *J. Physique*, 43(1):57–65, 1982.

Michael Erhard. Experimente mit mehrkomponentigen Bose-Einstein-Kondensaten. *Ph.D. thesis*, 2004. URL http://ediss.sub.uni-hamburg.de/volltexte/2004/2261/pdf/Dissertation.pdf.

Esteve J., Gross C., Weller A., Giovanazzi S., and Oberthaler M. K. Squeezing and entanglement in a Bose-Einstein condensate. *Nature*, 455(7217):1216–1219, oct 2008. ISSN 0028-0836. doi: 10.1038/nature07332. URL http://www.nature.com/nature/journal/v455/n7217/suppinfo/nature07332_S1.html. 10.1038/nature07332.

GammaVacuum. *Ion Pumping of Cesium and Rubidium*. Technical Bulletin 00.003.971, 2006.

J. M. Geremia, John K. Stockton, and Hideo Mabuchi. Tensor polarizability and dispersive quantum measurement of multilevel atoms. *Phys. Rev. A*, 73:042112, Apr 2006. doi: 10.1103/PhysRevA.73.042112. URL http://link.aps.org/doi/10.1103/PhysRevA.73.042112.

K. Góral, L. Santos, and M. Lewenstein. Quantum Phases of Dipolar Bosons in Optical Lattices. *Phys. Rev. Lett.*, 88:170406, Apr 2002. doi: 10.1103/PhysRevLett.88.170406. URL https://link.aps.org/doi/10.1103/PhysRevLett.88.170406.

Rudolf Grimm, Matthias Weidemuller, and Yurii B. Ovchinnikov. Optical Dipole Traps for Neutral Atoms. In Benjamin Bederson and Herbert Walther, editors, , volume 42 of *Advances In Atomic, Molecular, and Optical Physics*, pages 95–170. Academic Press, 2000. doi: 10.1016/S1049-250X(08)60186-X. URL http://www.sciencedirect.com/science/article/pii/S1049250X0860186X.

Qiang Gu and Richard A. Klemm. Ferromagnetic phase transition and Bose-Einstein condensation in spinor Bose gases. *Phys. Rev. A*, 68:031604, Sep 2003. doi: 10.1103/PhysRevA.68.031604. URL http://link.aps.org/doi/10.1103/PhysRevA.68.031604.

Qiang Gu, Kai Bongs, and Klaus Sengstock. Spin waves in ferromagnetically coupled spinor Bose gases. *Phys. Rev. A*, 70:063609, Dec 2004. doi: 10.1103/PhysRevA.70.063609. URL http://link.aps.org/doi/10.1103/PhysRevA.70.063609.

E. L. Hahn. Spin Echoes. *Phys. Rev.*, 80:580–594, Nov 1950. doi: 10.1103/PhysRev.80.580. URL http://link.aps.org/doi/10.1103/PhysRev.80.580.

Hansel W., Hommelhoff P., Hansch T. W., and Reichel J. Bose-Einstein condensation on a microelectronic chip. *Nature*, 413 (6855):498–501, oct 2001. ISSN 0028-0836. doi: 10.1038/35097032. 10.1038/35097032.

Thomas Hawkins. Cauchy and the spectral theory of matrices. *Historia Mathematica*, 2(1):1–29, 1975. ISSN 0315-0860. doi: 10.

1016/0315-0860(75)90032-4. URL http://www.sciencedirect.com/science/article/pii/0315086075900324.

James Michael Higbie. First Steps toward Precision Measurements using Multicomponent Bose-Einstein Condensates of 87Rb. 2005.

E Hodby, G Hechenblaikner, O M Maragò, J Arlt, S Hopkins, and C J Foot. Bose-Einstein condensation in a stiff TOP trap with adjustable geometry. *Journal of Physics B: Atomic, Molecular and Optical Physics*, 33(19):4087, 2000. URL http://stacks.iop.org/0953-4075/33/i=19/a=319.

Holger F. Hofmann and Shigeki Takeuchi. Quantum-state tomography for spin-l systems. *Phys. Rev. A*, 69:042108, Apr 2004. doi: 10.1103/PhysRevA.69.042108. URL http://link.aps.org/doi/10.1103/PhysRevA.69.042108.

P. Horak and W. H. Loh. On the delayed self-heterodyne interferometric technique for determining the linewidth of fiber lasers. *Opt. Exp.*, 14(9):3923, 2006.

Tomoya Isoshima, Tetsuo Ohmi, and Kazushige Machida. Double Phase Transitions in Magnetized Spinor Bose-Einstein Condensation. *Journal of the Physical Society of Japan*, 69(12):3864–3869, 2000. doi: 10.1143/JPSJ.69.3864. URL http://dx.doi.org/10.1143/JPSJ.69.3864.

David Jacob, Lingxuan Shao, Vincent Corre, Tilman Zibold, Luigi De Sarlo, Emmanuel Mimoun, Jean Dalibard, and Fabrice Gerbier. Phase diagram of spin-1 antiferromagnetic Bose-Einstein condensates. *Phys. Rev. A*, 86:061601, Dec 2012. doi: 10.1103/PhysRevA.86.061601. URL https://link.aps.org/doi/10.1103/PhysRevA.86.061601.

Martijn Jasperse. Faraday Magnetic Resonance Imaging of Bose-Einstein Condensates. *Ph.D. thesis*, 2015.

Josef M. Jauch and F Rohrlich. *The theory of photons and electrons : the relativistic quantum field theory of charged particles with spin one-half / J. M. Jauch and F. Rohrlich.* Springer-Verlag New York, 2d expanded ed. edition, 1976. ISBN 0387072950.

Ricardo Jiménez-Martínez and Svenja Knappe. *Microfabricated Optically-Pumped Magnetometers*, pages 523–551. Springer International Publishing, Cham, 2017. ISBN 978-3-319-34070-8. doi: 10.1007/978-3-319-34070-8_17. URL http://dx.doi.org/10.1007/978-3-319-34070-8_17.

Mattias T Johnsson, Graham R Dennis, and Joseph J Hope. Squeezing in Bose–Einstein condensates with large numbers of atoms. *New Journal of Physics*, 15(12):123024, 2013. URL http://stacks.iop.org/1367-2630/15/i=12/a=123024.

Yuki Kawaguchi and Masahito Ueda. Spinor Bose-Einstein condensates. *Physics Reports*, 520(5):253, 2012. doi: 10.1016/j.physrep.2012.07.005. URL http://www.sciencedirect.com/science/article/pii/S0370157312002098.

Andrew J. Kerman, Vladan Vuletić, Cheng Chin, and Steven Chu. Beyond Optical Molasses: 3D Raman Sideband Cooling of Atomic Cesium to High Phase-Space Density. *Phys. Rev. Lett.*, 84:439–442, Jan 2000. doi: 10.1103/PhysRevLett.84.439. URL http://link.aps.org/doi/10.1103/PhysRevLett.84.439.

Wolfgang Ketterle and N.J. Van Druten. Evaporative Cooling of Trapped Atoms. 37:181–236, 1996. ISSN 1049-250X. doi: 10.1016/S1049-250X(08)60101-9. URL http://www.sciencedirect.com/science/article/pii/S1049250X08601019.

Wolfgang Ketterle, Kendall B. Davis, Michael A. Joffe, Alex Martin, and David E. Pritchard. High densities of cold atoms in a *dark* spontaneous-force optical trap. *Phys. Rev. Lett.*, 70:2253–2256, Apr 1993. doi: 10.1103/PhysRevLett.70.2253. URL http://link.aps.org/doi/10.1103/PhysRevLett.70.2253.

Rainer Körber, Jan-Hendrik Storm, Hugh Seton, Jyrki P Mäkelä, Ritva Paetau, Lauri Parkkonen, Christoph Pfeiffer, Bushra Riaz, Justin F Schneiderman, Hui Dong, Seong-min Hwang, Lixing You, Ben Inglis, John Clarke, Michelle A Espy, Risto J Ilmoniemi, Per E Magnelind, Andrei N Matlashov, Jaakko O Nieminen, Petr L Volegov, Koos C J Zevenhoven, Nora Höfner,

Martin Burghoff, Keiji Enpuku, S Y Yang, Jen-Jei Chieh, Jukka Knuutila, Petteri Laine, and Jukka Nenonen. SQUIDs in biomagnetism: a roadmap towards improved healthcare. *Superconductor Science and Technology*, 29(11):113001, 2016. URL http://stacks.iop.org/0953-2048/29/i=11/a=113001.

M. Koschorreck, M. Napolitano, B. Dubost, and M. W. Mitchell. Quantum Nondemolition Measurement of Large-Spin Ensembles by Dynamical Decoupling. *Phys. Rev. Lett.*, 105:093602, Aug 2010a. doi: 10.1103/PhysRevLett.105.093602. URL https://link.aps.org/doi/10.1103/PhysRevLett.105.093602.

Marco Koschorreck. Generation of Spin Squeezing in an Ensemble of Cold Rubidium 87. *PhD Thesis*, 2010. URL https://www.icfo.eu/images/publications/MarcoKoschorreck_definitive.pdf.

Marco Koschorreck, Mario Napolitano, B. Dubost, and M. W. Mitchell. Sub-Projection-Noise Sensitivity in Broadband Atomic Magnetometry. *Phys. Rev. Lett.*, 104:093602, Mar 2010b. doi: 10.1103/PhysRevLett.104.093602. URL http://link.aps.org/doi/10.1103/PhysRevLett.104.093602.

M. Kubasik, M. Koschorreck, M. Napolitano, S. R. de Echaniz, H. Crepaz, J. Eschner, E. S. Polzik, and M. W. Mitchell. Polarization-based light-atom quantum interface with an all-optical trap. *Phys. Rev. A*, 79:043815, Apr 2009. doi: 10.1103/PhysRevA.79.043815. URL http://link.aps.org/doi/10.1103/PhysRevA.79.043815.

L D Landau and E M Lifschitz. *Mechanics*, volume 1. Pergamon, second edition, 1969.

C. K. Law, H. Pu, N. P. Bigelow, and J. H. Eberly. Quantum phase diffusion of a two-component dilute Bose-Einstein condensate. *Phys. Rev. A*, 58:531–535, Jul 1998. doi: 10.1103/PhysRevA.58.531. URL https://link.aps.org/doi/10.1103/PhysRevA.58.531.

Fam Le Kien, Philipp Schneeweiss, and Arno Rauschenbeutel. Dynamical polarizability of atoms in arbitrary light fields: gen-

eral theory and application to cesium. *Eur. Phys. J. D*, 67 (5):92, 2013. doi: 10.1140/epjd/e2013-30729-x. URL http://dx.doi.org/10.1140/epjd/e2013-30729-x.

Won-Kyu Lee, Han Seb Moon, and Ho Suhng Suh. Measurement of the absolute energy level and hyperfine structure of the 87Rb 4D5/2 state. *Opt. Lett.*, 32(19):2810–2812, Oct 2007. doi: 10.1364/OL.32.002810. URL http://ol.osa.org/abstract.cfm?URI=ol-32-19-2810.

Lobser D. S., Barentine A. E. S., Cornell E. A., and Lewandowski H. J. Observation of a persistent non-equilibrium state in cold atoms. *Nat Phys*, 11(12): 1009–1012, dec 2015. ISSN 1745-2473. doi: 10.1038/nphys3491. URL http://www.nature.com/nphys/journal/v11/n12/abs/nphys3491.html#supplementary-information.

Norman Margolus and Lev B. Levitin. The maximum speed of dynamical evolution. In *Proceedings of the Fourth Workshop on Physics and Consumption*, volume 120, pages 188–195, 1998. doi: 10.1016/S0167-2789(98)00054-2. URL http://www.sciencedirect.com/science/article/pii/S0167278998000542.

F. Mazzanti, A. Polls, and A. Fabrocini. Energy and structure of dilute hard- and soft-sphere gases. *Phys. Rev. A*, 67:063615, Jun 2003. doi: 10.1103/PhysRevA.67.063615. URL http://link.aps.org/doi/10.1103/PhysRevA.67.063615.

L. Mercer. 1/f Frequency Noise Effects on Self-Heterodyne Linewidth Measurements. *Journal of Lightwave Technology*, 9 (4):485, 1991.

J. D. Miller, R. A. Cline, and D. J. Heinzen. Far-off-resonance optical trapping of atoms. *Phys. Rev. A*, 47:R4567–R4570, Jun 1993. doi: 10.1103/PhysRevA.47.R4567. URL http://link.aps.org/doi/10.1103/PhysRevA.47.R4567.

Morgan Mitchell and John Kitching. Personal communication.

Morgan W. Mitchell. On the conjectured ħ limit to field sensing. *Notes*.

W. Muessel, H. Strobel, D. Linnemann, D. B. Hume, and M. K. Oberthaler. Scalable Spin Squeezing for Quantum-Enhanced Magnetometry with Bose-Einstein Condensates. *Phys. Rev. Lett.*, 113:103004, Sep 2014. doi: 10.1103/PhysRevLett.113.103004. URL https://link.aps.org/doi/10.1103/PhysRevLett.113.103004.

Özgür E. Müstecaplıoğlu, M. Zhang, and L. You. Spin squeezing and entanglement in spinor condensates. *Phys. Rev. A*, 66:033611, Sep 2002. doi: 10.1103/PhysRevA.66.033611. URL https://link.aps.org/doi/10.1103/PhysRevA.66.033611.

J. A. Nelder and R. Mead. A Simplex Method for Function Minimization. *The Computer Journal*, 7(4):308, 1965. doi: 10.1093/comjnl/7.4.308. URL +http://dx.doi.org/10.1093/comjnl/7.4.308.

NGDC. National Oceanic and Atmospheric Administration calculator. URL https://www.ngdc.noaa.gov/geomag/magfield.shtml.

Heung-Ryoul Noh and Han Seb Moon. Calculation of line shapes in double-resonance optical pumping. *Phys. Rev. A*, 80:022509, Aug 2009. doi: 10.1103/PhysRevA.80.022509. URL http://link.aps.org/doi/10.1103/PhysRevA.80.022509.

K. M. O'Hara, M. E. Gehm, S. R. Granade, and J. E. Thomas. Scaling laws for evaporative cooling in time-dependent optical traps. *Phys. Rev. A*, 64:051403, Oct 2001. doi: 10.1103/PhysRevA.64.051403. URL http://link.aps.org/doi/10.1103/PhysRevA.64.051403.

Abraham J. Olson, Robert J. Niffenegger, and Yong P. Chen. Optimizing the efficiency of evaporative cooling in optical dipole traps. *Phys. Rev. A*, 87:053613, May 2013. doi: 10.1103/PhysRevA.87.053613. URL http://link.aps.org/doi/10.1103/PhysRevA.87.053613.

B. Pasquiou, E. Maréchal, G. Bismut, P. Pedri, L. Vernac, O. Gorceix, and B. Laburthe-Tolra. Spontaneous Demagnetization of a Dipolar Spinor Bose Gas in an Ultralow Magnetic

Field. *Phys. Rev. Lett.*, 106:255303, Jun 2011. doi: 10.1103/PhysRevLett.106.255303. URL https://link.aps.org/doi/10.1103/PhysRevLett.106.255303.

C. J. Pethick and H. Smith. Cambridge University Press, reprinted edition, 2002.

William D. Phillips. Nobel Lecture: Laser cooling and trapping of neutral atoms. *Rev. Mod. Phys.*, 70:721–741, Jul 1998. doi: 10.1103/RevModPhys.70.721. URL http://link.aps.org/doi/10.1103/RevModPhys.70.721.

Ville Pietilä and Mikko Möttönen. Creation of Dirac Monopoles in Spinor Bose-Einstein Condensates. *Phys. Rev. Lett.*, 103:030401, Jul 2009. doi: 10.1103/PhysRevLett.103.030401. URL https://link.aps.org/doi/10.1103/PhysRevLett.103.030401.

Yu. M. Poluektov and V. M. Savchenko. Magnetic Transitions and Condensation in a Bose-Gas. *Journal of Low Temperature Physics*, 179(5):350–364, 2015. ISSN 1573-7357. doi: 10.1007/s10909-015-1298-6. URL http://dx.doi.org/10.1007/s10909-015-1298-6.

E. L. Raab, M. Prentiss, Alex Cable, Steven Chu, and D. E. Pritchard. Trapping of Neutral Sodium Atoms with Radiation Pressure. *Phys. Rev. Lett.*, 59:2631–2634, Dec 1987. doi: 10.1103/PhysRevLett.59.2631. URL http://link.aps.org/doi/10.1103/PhysRevLett.59.2631.

Ray M. W., Ruokokoski E., Kandel S., Mottonen M., and Hall D. S. Observation of Dirac monopoles in a synthetic magnetic field. *Nature*, 505(7485):657–660, jan 2014. ISSN 0028-0836. doi: 10.1038/nature12954. URL http://www.nature.com/nature/journal/v505/n7485/abs/nature12954.html#supplementary-information.

G. Reinaudi, T. Lahaye, Z. Wang, and D. Guéry-Odelin. Strong saturation absorption imaging of dense clouds of ultracold atoms. *Opt. Lett.*, 32(21):3143–3145, Nov 2007. doi: 10.1364/

OL.32.003143. URL http://ol.osa.org/abstract.cfm?URI=ol-32-21-3143.

Gael Reinaudi. 2013. URL http://www.scholarpedia.org/article/User:Gael_Reinaudi/Proposed/Absorption_imaging_of_ultracold_atoms.

Riedel Max F., Böhi Pascal, Li Yun, Hänsch Theodor W., Sinatra Alice, and Treutlein Philipp. Atom-chip-based generation of entanglement for quantum metrology. *Nature*, 464 (7292):1170–1173, apr 2010. ISSN 0028-0836. doi: 10.1038/nature08988. URL http://www.nature.com/nature/journal/v464/n7292/suppinfo/nature08988_S1.html. 10.1038/nature08988.

Sherman Rutherford. Ion Pump Operation & Trouble Shooting Guide. 1997.

M. S. Safronova, Carl J. Williams, and Charles W. Clark. Relativistic many-body calculations of electric-dipole matrix elements, lifetimes, and polarizabilities in rubidium. *Phys. Rev. A*, 69:022509, Feb 2004. doi: 10.1103/PhysRevA.69.022509. URL https://link.aps.org/doi/10.1103/PhysRevA.69.022509.

G. Santarelli, A. Clairon S.N. Lea, and G.M. Tino. Heterodyne optical phase-locking of extended-cavity semiconductor lasers at 9 GHz. *Optics Communications*, 104:339–344, 1994.

C. M. Savage and J. Ruostekoski. Dirac monopoles and dipoles in ferromagnetic spinor Bose-Einstein condensates. *Phys. Rev. A*, 68:043604, Oct 2003. doi: 10.1103/PhysRevA.68.043604. URL https://link.aps.org/doi/10.1103/PhysRevA.68.043604.

T. A. Savard, K. M. O'Hara, and J. E. Thomas. Laser-noise-induced heating in far-off resonance optical traps. *Phys. Rev. A*, 56:R1095–R1098, Aug 1997. doi: 10.1103/PhysRevA.56.R1095. URL http://link.aps.org/doi/10.1103/PhysRevA.56.R1095.

M Schmelz, V Zakosarenko, T Schönau, S Anders, S Linzen, R Stolz, and H-G Meyer. Nearly quantum limited

nanoSQUIDs based on cross-type Nb/AlO x /Nb junctions. *Superconductor Science and Technology*, 30(1):014001, 2017. URL http://stacks.iop.org/0953-2048/30/i=1/a=014001.

D. Sesko, T. Walker, C. Monroe, A. Gallagher, and C. Wieman. Collisional losses from a light-force atom trap. *Phys. Rev. Lett.*, 63:961–964, Aug 1989. doi: 10.1103/PhysRevLett.63.961. URL http://link.aps.org/doi/10.1103/PhysRevLett.63.961.

R. J. Sewell, M. Koschorreck, M. Napolitano, B. Dubost, N. Behbood, and M. W. Mitchell. Magnetic Sensitivity Beyond the Projection Noise Limit by Spin Squeezing. *Phys. Rev. Lett.*, 109:253605, Dec 2012. doi: 10.1103/PhysRevLett.109.253605. URL https://link.aps.org/doi/10.1103/PhysRevLett.109.253605.

A Smith, B E Anderson, S Chaudhury, and P S Jessen. Three-axis measurement and cancellation of background magnetic fields to less than 50 uG in a cold atom experiment. *Journal of Physics B: Atomic, Molecular and Optical Physics*, 44(20):205002, 2011. URL http://stacks.iop.org/0953-4075/44/i=20/a=205002.

Greg A. Smith, Souma Chaudhury, Andrew Silberfarb, Ivan H. Deutsch, and Poul S. Jessen. Continuous Weak Measurement and Nonlinear Dynamics in a Cold Spin Ensemble. *Phys. Rev. Lett.*, 93:163602, Oct 2004. doi: 10.1103/PhysRevLett.93.163602. URL http://link.aps.org/doi/10.1103/PhysRevLett.93.163602.

J. Söding, D. Guéry-Odelin, P. Desbiolles, F. Chevy, H. Inamori, and J. Dalibard. Three-body decay of a rubidium Bose–Einstein condensate. *Applied Physics B*, 69(4):257–261, 1999. ISSN 1432-0649. doi: 10.1007/s003400050805. URL http://dx.doi.org/10.1007/s003400050805.

D. M. Stamper-Kurn, M. R. Andrews, A. P. Chikkatur, S. Inouye, H.-J. Miesner, J. Stenger, and W. Ketterle. Optical Confinement of a Bose-Einstein Condensate. *Phys. Rev. Lett.*, 80:2027–2030, Mar 1998. doi: 10.1103/PhysRevLett.80.2027. URL https://link.aps.org/doi/10.1103/PhysRevLett.80.2027.

Dan M. Stamper-Kurn and Masahito Ueda. Spinor Bose gases: Symmetries, magnetism, and quantum dynamics. *Rev. Mod. Phys.*, 85:1191–1244, Jul 2013. doi: 10.1103/RevModPhys.85.1191. URL http://link.aps.org/doi/10.1103/RevModPhys.85.1191.

Daniel A. Steck. Rubidium 87 D Line Data, September 2001. URL http://steck.us/alkalidata/rubidium87numbers.1.6.pdf.

John Kenton Stockton. *Continuous quantum measurement of cold alkali-atom spins*. Dissertation (ph.d.), 2007. URL http://resolver.caltech.edu/CaltechETD:etd-02172007-172548.

Claudia D. Tesche and John Clarke. dc SQUID: Noise and optimization. *Journal of Low Temperature Physics*, 29(3):301–331, 1977. doi: 10.1007/BF00655097. URL http://dx.doi.org/10.1007/BF00655097.

T. Vanderbruggen and M. W. Mitchell. Near-resonant optical forces beyond the two-level approximation for a continuous source of spin-polarized cold atoms. *Phys. Rev. A*, 87:033410, Mar 2013. doi: 10.1103/PhysRevA.87.033410. URL http://link.aps.org/doi/10.1103/PhysRevA.87.033410.

T. Vanderbruggen, Silvana Palacios Álvarez, S. Coop, N. Martinez de Escobar, and M. W. Mitchell. Spontaneous $\mathcal{PT}$ symmetry breaking of a ferromagnetic superfluid in a gradient field. *EPL (Europhysics Letters)*, 111(6):66001, 2015. URL http://stacks.iop.org/0295-5075/111/i=6/a=66001.

M. Vengalattore, J. M. Higbie, S. R. Leslie, J. Guzman, L. E. Sadler, and D. M. Stamper-Kurn. High-Resolution Magnetometry with a Spinor Bose-Einstein Condensate. *Phys. Rev. Lett.*, 98:200801, May 2007. doi: 10.1103/PhysRevLett.98.200801. URL http://link.aps.org/doi/10.1103/PhysRevLett.98.200801.

M. Vengalattore, J. Guzman, S. R. Leslie, F. Serwane, and D. M. Stamper-Kurn. Periodic spin textures in a degenerate $F = 1$ ^{87}Rb spinor Bose gas. *Phys. Rev. A*, 81:053612, May 2010. doi: 10.1103/PhysRevA.81.053612. URL https://link.aps.org/doi/10.1103/PhysRevA.81.053612.

Nikolay Vitanov, Thomas Halfmann, Bruce W Shore, and Klaas Bergmann. LASER-INDUCED POPULATION TRANSFER BY ADIABATIC PASSAGE TECHNIQUES. *Annual Review of Physical Chemistry*, 52(1):763–809, 2001. doi: 10.1146/annurev.physchem.52.1.763. URL http://dx.doi.org/10.1146/annurev.physchem.52.1.763. PMID: 11326080.

Ying-Ju Wang, Dana Z. Anderson, Victor M. Bright, Eric A. Cornell, Quentin Diot, Tetsuo Kishimoto, Mara Prentiss, R. A. Saravanan, Stephen R. Segal, and Saijun Wu. Atom Michelson Interferometer on a Chip Using a Bose-Einstein Condensate. *Phys. Rev. Lett.*, 94:090405, Mar 2005. doi: 10.1103/PhysRevLett.94.090405. URL https://link.aps.org/doi/10.1103/PhysRevLett.94.090405.

David S. Weiss, Erling Riis, Yaakov Shevy, P. Jeffrey Ungar, and Steven Chu. Optical molasses and multilevel atoms: experiment. *J. Opt. Soc. Am. B*, 6(11):2072–2083, Nov 1989. doi: 10.1364/JOSAB.6.002072. URL http://josab.osa.org/abstract.cfm?URI=josab-6-11-2072.

S. Wildermuth, S. Hofferberth, I. Lesanovsky, S. Groth, P. Krüger, J. Schmiedmayer, and I. Bar-Joseph. Sensing electric and magnetic fields with Bose-Einstein condensates. *Applied Physics Letters*, 88(26):264103, 2006. doi: 10.1063/1.2216932. URL http://dx.doi.org/10.1063/1.2216932.

Tony W. Wilson, Elizabeth Heinrichs-Graham, Amy L. Proskovec, and Timothy J. McDermott. Neuroimaging with magnetoencephalography: A dynamic view of brain pathophysiology. *Translational Research*, 175:17–36, 2016. ISSN 1931-5244. doi: 10.1016/j.trsl.2016.01.007. URL http://www.sciencedirect.com/science/article/pii/S1931524416000311. In-Depth Review: New Insights in Neuroimaging.

Florian Wolfgramm, Alessandro Cerè, Federica A. Beduini, Ana Predojević, Marco Koschorreck, and Morgan W. Mitchell. Squeezed-Light Optical Magnetometry. *Phys. Rev. Lett.*, 105:053601, Jul 2010. doi: 10.1103/PhysRevLett.105.053601.

URL https://link.aps.org/doi/10.1103/PhysRevLett.105.053601.

Florian Wolfgramm, Chiara Vitelli, Federica A. Beduini, Nicolas Godbout, and Morgan W. Mitchell. Entanglement-enhanced probing of a delicate material system. *Nat Photon*, 7(1):28–32, jan 2013. ISSN 1749-4885. doi: 10.1038/nphoton.2012.300. URL http://www.nature.com/nphoton/journal/v7/n1/abs/nphoton.2012.300.html#supplementary-information. 10.1038/nphoton.2012.300.

A. A. Wood, L. M. Bennie, A. Duong, M. Jasperse, L. D. Turner, and R. P. Anderson. Magnetic tensor gradiometry using Ramsey interferometry of spinor condensates. *Phys. Rev. A*, 92:053604, Nov 2015. doi: 10.1103/PhysRevA.92.053604. URL http://link.aps.org/doi/10.1103/PhysRevA.92.053604.

Keiji Yamada. Thermal Properties of the System of Magnetic Bosons — Bose-Einstein Ferromagnetism —. *Progress of Theoretical Physics*, 67(2):443, 1982. doi: 10.1143/PTP.67.443. URL http://dx.doi.org/10.1143/PTP.67.443.

S. Yi and H. Pu. Spontaneous Spin Textures in Dipolar Spinor Condensates. *Phys. Rev. Lett.*, 97:020401, Jul 2006. doi: 10.1103/PhysRevLett.97.020401. URL http://link.aps.org/doi/10.1103/PhysRevLett.97.020401.

S. Yi, L. You, and H. Pu. Quantum Phases of Dipolar Spinor Condensates. *Phys. Rev. Lett.*, 93:040403, Jul 2004. doi: 10.1103/PhysRevLett.93.040403. URL http://link.aps.org/doi/10.1103/PhysRevLett.93.040403.

COLOPHON

This document was typeset using a modified version of the typographical look-and-feel `classicthesis` available at:

`http://code.google.com/p/classicthesis/`

Final Version as of May 13, 2017 (`classicthesis`).

DECLARATION

I declare that this thesis has been composed solely by myself and that it has not been submitted, in whole or in part, in any previous application for a degree. Except where states otherwise by reference or acknowledgment. The data presented in this thesis was obtained in an experiment carried out by the atom 2.0 team in the group of Prof. Morgan W. Mitchell in ICFO-The Institute of Photonic Sciences where collaboration happened. I played a major role in the preparation and execution of the experiment, and the data analysis and interpretation are entirely by own work. Any contributions entirely from colleagues are explicitly referenced in the text.

ICFO-The Institute of Photonic Sciences, 2017

Silvana Palacios Álvarez